

Structural evolution, exhumation rates, and rheology of the European crust during Alpine collision: constraints from the Rotondo granite - Gotthard nappe

Alberto Ceccato¹, Whitney M. Behr², Alba Zappone³, Lorenzo Tavazzani¹, and Andrea Giuliani¹

¹ETH Zurich

²Department of Earth Sciences, ETH Zürich

³Geological Institute, ETH Zurich

December 18, 2023

Abstract

The rheology of crystalline units controls the large-scale deformation geometry and dynamics of collisional orogens. Defining a time-constrained rheological evolution of such units may help unravel the details of collisional dynamics. Here, we integrate field analysis, pseudosection calculations and in-situ garnet U-Pb and mica Rb-Sr geochronology to define the structural and rheological evolution of the Rotondo granite (Gotthard nappe, Central Alps). We identify a sequence of four (D1-D4) deformation stages. Pre-collisional D1 brittle faults developed before Alpine peak metamorphism, which occurred at 34-20 Ma (U-Pb garnet ages) at $590 \pm 25^\circ\text{C}$ and 0.95 ± 0.1 GPa. The reactivation of D1 structures controlled the rheological evolution, from D2 reverse mylonitic shearing at amphibolite facies ($520 \pm 40^\circ\text{C}$ and 0.85 ± 0.1 GPa) at 18-20 Ma (white mica Rb-Sr ages), to strike-slip, brittle-ductile shearing at greenschist-facies D3 ($395 \pm 25^\circ\text{C}$ and 0.4 ± 0.1 GPa) at 14-15 Ma (white and dark mica Rb-Sr ages), and then to D4 strike-slip faulting at shallow conditions. Although highly misoriented for the Alpine collisional stress orientation, D1 brittle structures controlled the localization of D2 ductile mylonites accommodating fast (1-3 mm/yr) exhumation rates due to their weak shear strength (<10 MPa). This structural and rheological evolution is common across External Crystalline Massifs (e.g., Aar, Mont Blanc), suggesting that the entire European crust was extremely weak during Alpine collision, its strength controlled by weak ductile shear zones localized on pre-collisional deformation structures, that in turn controlled localized exhumation at the scale of the orogen.

Hosted file

982039_0_supp_11682685_s550j5.docx available at <https://authorea.com/users/709591/articles/693995-structural-evolution-exhumation-rates-and-rheology-of-the-european-crust-during-alpine-collision-constraints-from-the-rotondo-granite-gotthard-nappe>

1 **Structural evolution, exhumation rates, and rheology of the European crust**
2 **during Alpine collision: constraints from the Rotondo granite – Gotthard nappe**
3

4 **A. Ceccato¹, W. M. Behr¹, A. S. Zappone², L. Tavazzani³, and A. Giuliani³**

5
6 ¹Structural Geology and Tectonics Group, Geological Institute, Department of Earth Sciences,
7 ETH Zurich, Sonneggstrasse 5, 8092 Zurich, Switzerland.

8 ²Swiss Seismological Service, ETHZ, Zurich, 8092, Switzerland.

9 ³Institute of Geochemistry and Petrology, Department of Earth Sciences, ETH Zurich,
10 Clausiusstrasse 25, 8092 Zurich, Switzerland.

11
12 Corresponding author: Alberto Ceccato (aceccato@erdw.ethz.ch)

13
14 **Key Points:**

- 15 • Garnet U-Pb, mica Rb-Sr dating constrain exhumation of Rotondo granite from
16 amphibolite facies at 34-20 Ma to greenschist facies at 15-14 Ma
- 17 • Fast exhumation (1-3 mm/yr) accommodated by ductile shearing of weak shear zones
18 localized on pre-collisional brittle deformation structures
- 19 • The European crust was extremely weak during collision, rheology was controlled by
20 metamorphic and fluid evolution in localized shear zones
21

22

Abstract

23

24

25

26

27

28

29

30

31

32

33

34

35

36

37

38

39

40

41

42

43

1 Introduction

44

45

46

47

48

49

50

51

52

53

54

55

56

57

58

59

60

61

62

63

64

65

The rheology of crystalline units controls the large-scale deformation geometry and dynamics of collisional orogens. Defining a time-constrained rheological evolution of such units may help unravel the details of collisional dynamics. Here, we integrate field analysis, pseudosection calculations and in-situ garnet U-Pb and mica Rb-Sr geochronology to define the structural and rheological evolution of the Rotondo granite (Gotthard nappe, Central Alps). We identify a sequence of four (D₁-D₄) deformation stages. Pre-collisional D₁ brittle faults developed before Alpine peak metamorphism, which occurred at 34-20 Ma (U-Pb garnet ages) at 590 ± 25°C and 0.95 ± 0.1 GPa. The reactivation of D₁ structures controlled the rheological evolution, from D₂ reverse mylonitic shearing at amphibolite facies (520 ± 40°C and 0.85 ± 0.1 GPa) at 18-20 Ma (white mica Rb-Sr ages), to strike-slip, brittle-ductile shearing at greenschist-facies D₃ (395 ± 25 °C and 0.4 ± 0.1 GPa) at 14-15 Ma (white and dark mica Rb-Sr ages), and then to D₄ strike-slip faulting at shallow conditions. Although highly misoriented for the Alpine collisional stress orientation, D₁ brittle structures controlled the localization of D₂ ductile mylonites accommodating fast (1-3 mm/yr) exhumation rates due to their weak shear strength (<10 MPa). This structural and rheological evolution is common across External Crystalline Massifs (e.g., Aar, Mont Blanc), suggesting that the entire European crust was extremely weak during Alpine collision, its strength controlled by weak ductile shear zones localized on pre-collisional deformation structures, that in turn controlled localized exhumation at the scale of the orogen.

During mountain-building events, rheological contrasts between lithospheric plates are first-order controls on the geometry of collision (Faccenda et al., 2008; Vogt et al., 2018, Candiotti et al., 2021), the development of topography (Cook & Royden, 2008; Wolf et al., 2022), and the styles and rates of regional deformation and metamorphism (Willingshofer et al., 2005; Piccolo et al., 2018). Rheological contrasts may result from different crustal compositions, ages, geological histories, and/or thermal regimes of the lithospheric plates involved in collision (Audet & Burgmann, 2011; Mouthereau et al., 2013). For example, depending on the composition and the fluid content, lithospheric plates may present different mechanical behavior (brittle vs. viscous deformation) and strength at the same depth and temperature conditions during collision (Bürgmann & Dresen, 2008; Menegon et al., 2011; Behr & Platt, 2014, Jamtveit et al., 2019). Furthermore, the occurrence of anisotropic structural fabrics (foliations and fractures), strictly related to the geological history of crustal sections, may promote or hinder deformation depending on their suitability to be reactivated, and/or their ability to promote or hinder fluid infiltration (Ceccato et al., 2020, Zertani et al., 2023). Pressure, temperature, fluid, and structural fabrics evolve with the tectono-metamorphic evolution of a collisional orogen, and so does their effects on the rheological contrast between colliding plates (Groome et al., 2008; Behr & Platt, 2013; Bellanger et al., 2014; Ceccato et al., 2020).

Most of the deformation and shortening in the core of collisional belts is accommodated through deformation of crystalline basement units (Lacombe & Mouthereau, 2002; Rosenberg & Kissling, 2013; Pfiffner, 2016). Such crystalline units are typically characterized by poly-metamorphic histories, with wet and/or dry mineral assemblages, and multiple tectonic fabrics, all of them strongly affecting the rheology during collision (Audet & Burgmann, 2011;

66 Mouterau et al., 2013). Moreover, pre-collisional events such as lithospheric rifting, prograde
67 burial, and subduction, lead to the development of additional deformation structures (e.g., rift-
68 related normal fault zones) and tectonic fabrics (e.g., prograde foliations), which may introduce
69 rheological heterogeneity that later influences collisional dynamics (Mohn et al., 2014). The
70 European Alps is a region where both inherited compositional and fabric variations, as well as
71 pre-collisional tectonics, are thought to have strongly influenced later syn-orogenic development.
72 For example, rheological contrast between the upper (Adriatic) and lower (European) crust
73 varies along the strike of the orogen, and resulted in different patterns of strain partitioning,
74 amounts of shortening and exhumation, and collisional styles between the Western, Central and
75 Eastern Alps (Bellahsen et al., 2014; Rosenberg & Kissling, 2013). In the Central Alps, in
76 particular, the Adriatic upper plate indents into the weaker, thickened European crust (Rosenberg
77 & Kissling, 2013). The European thickened crust is composed of stacked slices of crystalline
78 basement derived from the thinned Mesozoic European margin, now exposed in the Aar massif,
79 Gotthard nappe, and Lepontine dome (Fig. 1). The thickened European crust is considered here
80 to be much weaker than the juxtaposed Adriatic continental lithosphere, represented by the
81 almost undeformed, lower-crustal Ivrea-Verbano complex (Fig. 1). However, constraints on the
82 factors controlling this “weakness” are sparse, including whether the crust was weak since the
83 beginning of burial and subduction, or if it was initially strong and then progressively weakened
84 during collision. Both tectonic inheritance related to Mesozoic rifting (Bellahsen et al., 2014) and
85 syn-collisional Barrovian metamorphism (Rosenberg & Kissling, 2013) might have contributed
86 to the weakening of the European continental crust in this part of the Alps.

87 To better understand this weakening process, and the extent to which different factors
88 (temperature, fluids, inherited fabrics) contributed to it, a detailed characterization of the
89 structural and rheological evolution of the crystalline basement is required. Providing a time-
90 integrated evolution of the rheology and of the geological parameters controlling this evolution
91 might help us to quantitatively constrain the relationship between the rheology of crystalline
92 basement units and the large-scale geometry and dynamics of the Alpine orogen.

93 In this regard, previous investigations have revealed a recurrent brittle-to-ductile
94 structural evolution (i.e., ductile shear zone related to collisional processes overprinting pre-
95 existent brittle faults and fractures) of crystalline basement units in the Western and Central Alps
96 (e.g., Mont Blanc: Guermani & Pennacchioni, 1998; Gran Paradiso: Menegon & Pennacchioni,
97 2010; Aar-Gotthard: Oliot et al., 2014; Rolland et al., 2009; Wehrens et al., 2016; Lepontine
98 Dome: Goncalves et al., 2016). Several hypotheses were proposed to explain such brittle-to-
99 ductile evolution, including the occurrence of prograde brittle deformation during burial
100 (Guermani & Pennacchioni, 1998), and mid-crustal seismicity at peak metamorphic conditions
101 (Wehrens et al., 2016). Previous authors have also speculated on the occurrence of pervasive
102 extensional faulting related to the Mesozoic rifting of the European margin, providing field
103 evidence for limited reactivation of structures inherited from rifting (Ballèvre et al., 2018;
104 Dall’Asta et al., 2022; Herwegh et al., 2017, 2020; Nibourel et al. 2021; Musso-Piantelli et al.,
105 2022).

106 Here we present an integrated field and petrochronological study of the deformation
107 features of the Rotondo granite in the Gotthard nappe (Fig. 1). The Gotthard nappe represents a
108 sliver of European crust now exposed in the Central Swiss Alps. The Rotondo granite is a Post-
109 Variscan pluton (i.e., not affected by Variscan tectonometamorphic events), intruded into the
110 European polymetamorphic crust. Differently from its host polymetamorphic host rock, the lack

111 of Variscan pervasive fabrics (foliations) and the homogeneous texture of the granite allow us to
112 define a sequence of (localized) deformation structures probably related to Alpine deformation.
113 We use structural and petrochronological data to:

- 114 i. Define the pressure-temperature-time-deformation (P - T - t - d) path of the Rotondo
115 granite;
- 116 ii. Examine the time-constrained structural and rheological evolution of the
117 thickened crust of the lower plate during Alpine continental collision;
- 118 iii. Investigate the geological factors that affect the rheological evolution of the
119 crystalline unit.

120 **2 Geological setting**

121 The European Alps (Fig. 1) are a double-verging orogen resulting from the continental
122 collision between Europe and Adria, following the closure and subduction of the Mesozoic
123 Tethys ocean (Dal Piaz et al., 2003). European and Adriatic polymetamorphic crustal sections
124 were each strongly modified by the Variscan orogeny during the formation of the Pangean
125 supercontinent. The Permo-Mesozoic breakup of Pangea led to the development of the Tethys
126 Ocean, including the Liguro-Piemontese ocean and Valais trough. The development of the
127 Liguro-Piemontese ocean divided Europe from Adria (210-140 Ma) by 200-400 km (Ballèvre et
128 al., 2018; Beltrando et al., 2014). A second, more short-lived rifting phase took place on the
129 European margin to the north of the Liguro-Piemontese ocean and led to the development of the
130 Valais trough during Late-Jurassic to Early Cretaceous (140-120 Ma), separating the European
131 distal margin from the southern Briançonnais microcontinent (Beltrando et al., 2012; Célini et
132 al., 2023; Handy et al., 2010). This former paleogeography is now preserved in the Internal
133 (Penninic) domains of the Central and Western Alps, exposing the remnants of the Valaisan,
134 Briançonnais and Liguro-Piemontese units (Fig. 1). The proximal European passive margin is
135 now exposed in the External Crystalline Massifs (ECMs), including: Aar, Mont Blanc, Aiguille
136 Rouges, Belledonne, Pelvoux-Oisian massifs as well as in the Gotthard nappe (Fig. 1a; Lemoine
137 et al., 1986).

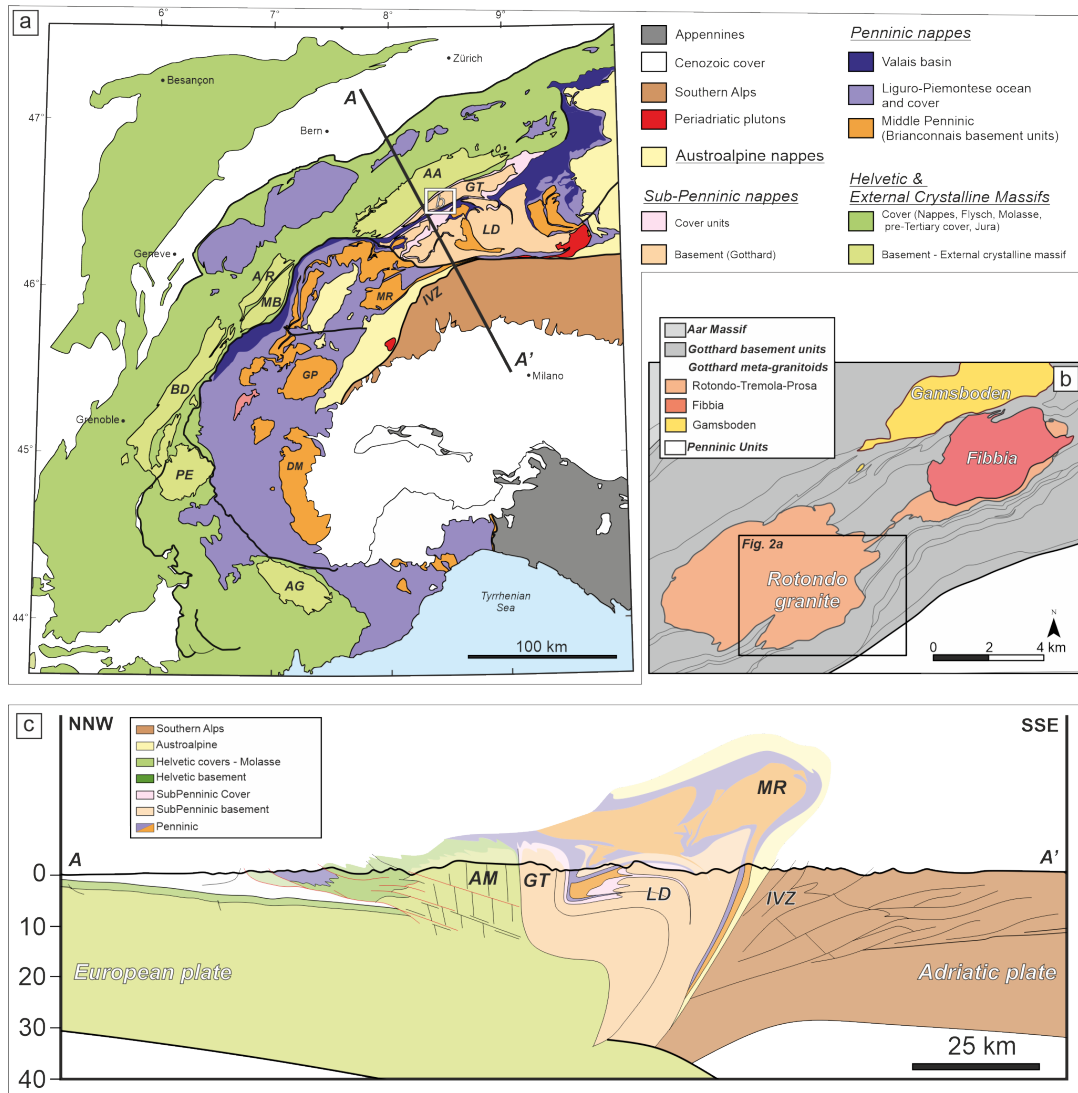
138 The study area is located in the Gotthard nappe (Swiss Alps, Fig. 1a). The Gotthard
139 nappe includes a series of polymetamorphic Ordovician-Silurian crystalline units intruded by
140 late-Variscan granitoids (Berger et al., 2017). The crystalline units include high-grade gneisses of
141 the Val Nalps, Paradis and Streifegneis complexes (Fig. 2a; Berger et al., 2017). The Val Nalps
142 and Paradis Complexes preserve evidence of an Early- to Mid-Ordovician (~470 Ma) high grade
143 metamorphism, later affected by Silurian (~440 Ma) magmatism (Berger et al., 2017). Between
144 340 and 300 Ma, these complexes were affected by Variscan amphibolite facies metamorphism
145 and transpressional shearing (Bühler et al., 2022; Simonetti et al., 2020; Vanardois et al., 2022).
146 Post-Variscan magmatism led to the intrusion of several granitic plutons into the
147 polymetamorphic basement, including the Cristallina granodiorite, the Fibbia and Gamsboden
148 granite-gneisses and the Rotondo granite (Fig., 1b; Berger et al., 2017).

149 At the regional scale, the European crust was affected by the development of Permo-
150 Mesozoic transtensional basins, resulting eventually in the formation of the Valais trough in the
151 Jurassic-Cretaceous period (Ballèvre et al., 2018; Célini et al., 2023; Handy et al., 2010). The
152 units now included in the Gotthard nappe were part of the distal European passive margin
153 located north of the Valais trough (Schmid et al., 2004). From the Late Cretaceous onwards,
154 convergence between Europe and Adria led to the subduction of the Liguro-Piemontese ocean

155 and to progressive development of the Penninic accretionary wedge facing the advancing
156 Adriatic upper plate (Dal Piaz et al., 2003). Progressive convergence led to burial and
157 underthrusting of the European passive margin, eventually leading to continental collision. The
158 Gotthard nappe was buried beneath the advancing Penninic accretionary wedge around 35 Ma
159 (Handy et al., 2010), reaching greenschist-facies conditions between 35 and 22 Ma (Herwegh et
160 al., 2020; Janots et al., 2009). Subsequently, continental collision between Europe and Adria led
161 to the rapid exhumation of the crystalline units of the Gotthard-Aar massifs at around 22-17 Ma,
162 through the activation of greenschist facies sub-vertical ductile shear zones with reverse
163 kinematics ($T = 450\text{-}500\text{ }^{\circ}\text{C}$ and $P = 0.7\text{-}0.8\text{ GPa}$; Challandes et al., 2008; Goncalves et al., 2012;
164 Herwegh et al., 2017; Oliot et al., 2010; Rolland et al., 2008, 2009). From 14 Ma onward, the
165 Gotthard nappe was then affected by regional strike-slip tectonics related to the activity of the
166 Simplon-Rhone transtensional fault system (Campani et al., 2010; Herwegh et al., 2017).
167 Shallow brittle faulting has affected the Gotthard nappe since the Late Miocene, leading to the
168 activation of brittle gouge-bearing faults up to recent times (Kralik et al., 1992; Pleuger et al.,
169 2012).

170 2.1 The Rotondo granite

171 The Rotondo Granite (RG) is an Early-Permian (295 Ma, U-Pb on zircon, Rast et al.,
172 2022) peraluminous granite, crosscut by mafic dykes (290-285 Ma, U-Pb on zircon, Bussien et
173 al., 2008). It includes two main magmatic facies (equigranular RG₁ and porphyritic RG₂) both
174 composed of $\text{Qz} + \text{Kfs} + \text{Pl} + \text{Bt} \pm \text{Wm} \pm \text{Grt} \pm \text{Ep} \pm \text{Chl} \pm \text{Zr} \pm \text{Spn} \pm \text{Cal} \pm \text{Py}$ (Rast et al.,
175 2022, mineral abbreviations from Whitney & Evans, 2010; Wm: white mica). RG₁ and RG₂
176 facies only differ by mineral proportions and the occurrence of a Bt-Kfs foliation in RG₂ (Rast et
177 al., 2022). This meso-scale bulk foliation has been attributed to an Alpine greenschist facies
178 overprint, based on field and microstructural observations (Gapais et al., 1987; Steck, 1976;
179 Steck & Burri, 1971). Another evidence of Alpine greenschist facies metamorphism is the
180 occurrence of atoll-like garnets in the Rotondo granite (Steck, 1976; Steck & Burri, 1971). The
181 peculiar atoll-like shape, and their Ca-rich composition, have been interpreted by Steck & Burri
182 (1971) to reflect two metamorphic growth stages at different temperature and/or fluid activity
183 conditions. However, the textural relationship between the atoll-garnets and the bulk foliation
184 was not addressed in detail. A set of steep, NW-dipping ductile shear zones, with top-to-SE dip-
185 slip reverse kinematics developed during the same Alpine retrograde event (Lützenkirchen &
186 Loew, 2011). The ductile shear zones have been classified in two main groups (Rast et al., 2022):
187 (i) granitic shear zones, composed of fine-grained mylonite with feldspar augens in a biotite-
188 bearing foliation; and (ii) quartz-biotite-rich shear zones, characterized by the occurrence of
189 sigmoidal quartz veins with rigid cm-sized calcite clasts. Ductile shear zones were exploited as
190 nucleation sites for late brittle faulting at upper crustal levels, as inferred from the stability of
191 syn- to post-kinematic zeolite minerals, and the formation of clay-rich gouges (Lützenkirchen &
192 Loew, 2011). Despite the general understanding of the regional and local scale tectonic
193 evolution, a detailed and holistic description of the structural and tectonometamorphic features,
194 and absolute timing of deformation events in this area are still missing.



195
 196 **Figure 1:** Geological setting of the study area. (a) Tectonic sketch of the Central-Western
 197 Alps (redrawn from Ballèvre et al., 2018, Schmid et al., 2004). AA: Aar; AG: Argentera; AR:
 198 Aiguilles rouges; BD: Belledonne; DM: Dora Maira; GP: Gran Paradiso; GT: Gotthard; IVZ:
 199 Ivrea-Verbano Zone; LD: Lepontine Dome; MB: Mont Blanc; MR: Monte Rosa; PE: Pelvoux.
 200 (b) Tectonic sketch of the Central-Western Gotthard massif showing the spatial distribution of
 201 the meta-granitoid intrusion (Rotondo, Fiabba, Gamsboden). (c) Geological section across the
 202 Central Swiss Alps.

203 **3 Material and Methods**

204 **3.1. Field structural analysis**

205 This work further extends the previous work of Lützenkirchen & Loew (2011) and Rast
 206 et al. (2022), improving the detail of structural description, and adding absolute age constraints
 207 on the deformation structures, with implications on regional tectonic and rheological evolution. It
 208 provides a detailed description of the structural evolution and inventory of the deformation
 209 structures affecting the rock massif hosting the Bedretto Underground Laboratory for

210 Geosciences and Geoenergies (BULGG; Ma et al., 2022). Field survey was focused on the
211 analyses of deformation features and the collection of structural data at 205 structural stations
212 (“Waypoints” – WP in Fig. 2a), resulting in a georeferenced dataset of 473 structural
213 measurements, each of which includes a structural description, orientation of shear plane
214 (Dip/Dip direction) and lineation (Trend/Plunge), kinematics, mineralogy, deformation fabric
215 (brittle vs. ductile), thickness, length, and throw. These structures were then subdivided into sets
216 based on kinematic compatibility, mineralogy, and texture. Oriented samples were collected for
217 further microstructural and petrochronological analysis. The geographic coordinates of relevant
218 waypoints are reported in the Supplementary Information (SI) Table S1. The Structural dataset is
219 available in the SI Dataset DS1

220 3.2. Optical/Scanning Electron Microscopy and Electron Probe Micro Analyses

221 Thin sections were cut parallel to the lineation direction (X kinematic direction) and
222 perpendicular to the foliation plane (XY kinematic plane). Backscattered electron (BSE) images
223 and Energy Dispersion Spectrometry (EDS) mapping were performed at ScopeM (ETH) with a
224 Hitachi SU5000 Scanning Electron Microscope (SEM). Quantitative compositional analyses
225 were performed at the Institute for Geochemistry and Petrology (ETH) with a JEOL JXA-8230
226 Electron Probe Microanalyzer equipped with five Wavelength Dispersion Spectrometers (WDS).
227 Further details on analytical conditions are reported in the SI Text S1. Mineral compositions are
228 reported in the SI Table S2.

229 3.3. P-T pseudosection calculation

230 The bulk rock compositions adopted for pseudosection calculation were obtained by X-
231 Ray Fluorescence spectroscopy at the Institute for Geochemistry and Petrology (ETH) with a
232 WD-XRF PANalytical AXIOS equipped with five diffraction crystals (bulk compositions are
233 reported in the SI Table S3). Pressure-temperature pseudosection calculations were performed
234 with *Perple_X* 6.9.1 (Connolly, 2005) adopting the thermodynamic database of pure end-
235 members from Holland & Powell, (2011; *hp62ver.dat*). Adopted solid solution models and
236 computational details are reported in the SI Text S1. The chemical system used for the
237 calculation is MnO-Na₂O-CaO-K₂O-FeO-MgO-Al₂O₃-SiO₂-H₂O-TiO₂-Fe₂O₃
238 (MNCKFMASHTO). In the text, the term “observed” refers to the paragenesis observed in thin
239 section and to the phase chemistry obtained from EPMA analyses; the term “computed” refers to
240 the chemistry and mineral paragenesis calculated by pseudosection computations. Results of
241 pseudosections and related files are available in the SI Dataset DS2.

242 3.4. In-situ LA-ICP-MS U-Pb & Trace Element analyses

243 In-situ Garnet U-Pb dating, and trace element analyses were performed on polished thin
244 sections by laser ablation-inductively coupled plasma-mass spectrometry (LA-ICP-MS) at the
245 ERDW department of ETH Zurich using an ASI RESOLUTION S-155 excimer (ArF, 193 nm) laser
246 ablation system coupled to a Thermo Scientific Element XR sector-field ICP-MS (Guillong et
247 al., 2014). Instrumentation and data acquisition parameters for U-Pb dating are summarized in SI
248 Dataset DS3 reporting standards of Horstwood et al. (2016). All data from the session, including
249 details on the data reduction strategies and results of validation reference materials can be found
250 in SI Dataset DS3.

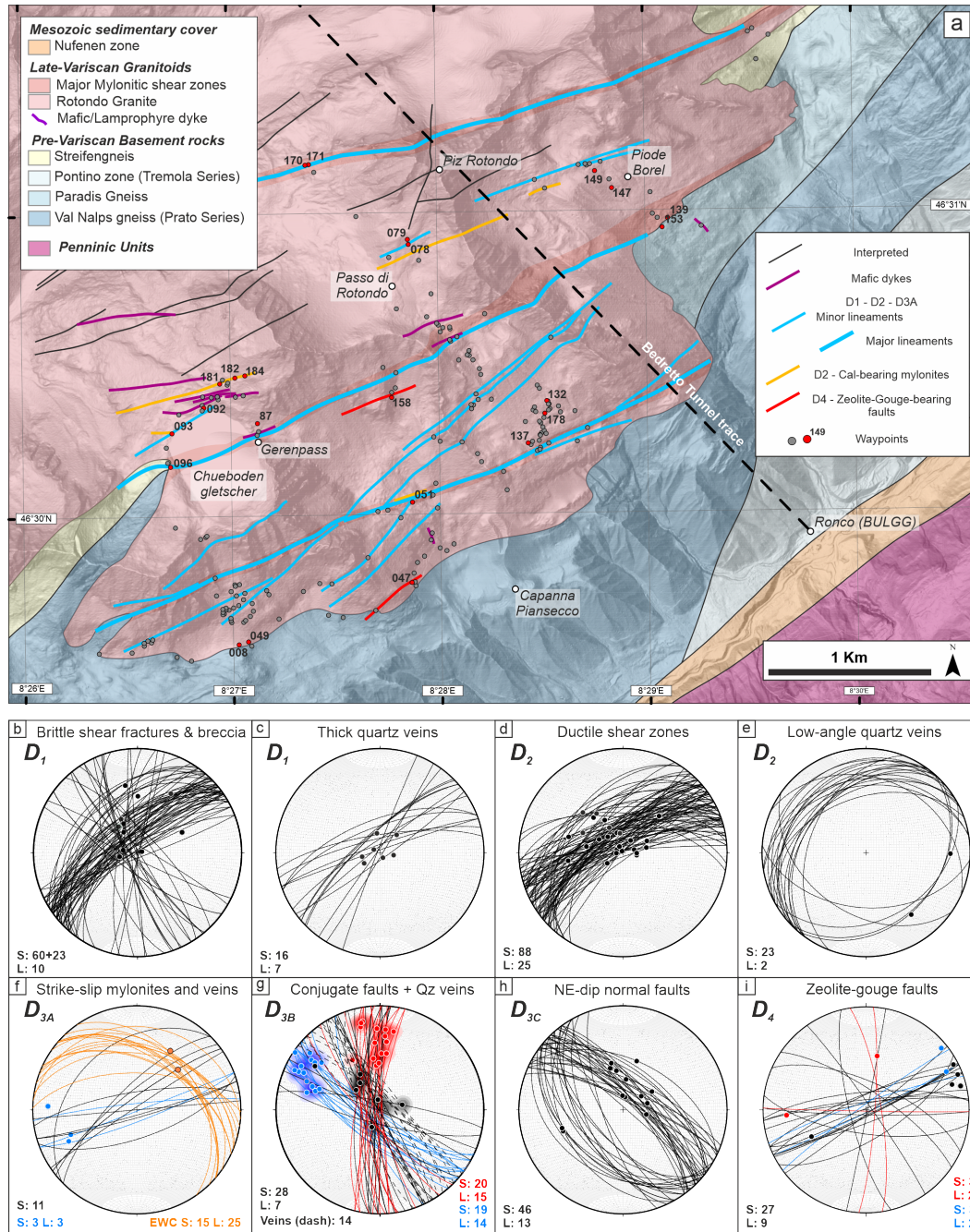
251 3.5. In-situ LA-ICP-MS Rb-Sr analyses

252 In situ Rb-Sr isotope analyses of mica in thin section were undertaken using an ASI
253 RESolution 193 nm excimer laser probe interfaced to an Agilent 8800 ICP-MS/MS at ETH
254 Zurich following the procedure outlined in Giuliani et al. (in review). This method employs an
255 isochronous in-house mica reference material from the Wimbledon lamproite (Sarkar et al.,
256 2023) to calibrate the Rb/Sr fractionation in mica unknowns following initial calibration of
257 $^{87}\text{Sr}/^{86}\text{Sr}$ and $^{87}\text{Rb}/^{86}\text{Sr}$ using the silicate glass reference material NIST 610. This method is
258 validated by analyses of micas from the Bultfontein kimberlite with ages independently
259 constrained by isotope-dilution Rb-Sr dating (Fitzpayne et al., 2020). All the details pertaining
260 analytical conditions, reference materials and data processing can be found in the SI Text S1.
261 The Rb-Sr age data are summarized in Table 1 and all the Rb-Sr analyses can be found in SI
262 Dataset DS4.

263 **4. Results**

264 4.1 Field observations – Sequence of localized deformation structures

265 In the following, we describe the sequence of subsolidus deformation structures,
266 numbered following their relative chronology (from the oldest D₁, to the youngest D₄), as
267 inferred from field analyses of crosscutting and overprinting relationships, mineralogy, texture,
268 and kinematics. Structural data are summarized in Fig. 2b-i. Field images of the described
269 structure sets are reported in Figs. 3-4-5. In the SI Text S2, additional data about the magmatic
270 structures (aplitic and mafic dykes), and the tectonometamorphic evolution of the RG-host rocks
271 are presented.



272

273 **Figure 2.** Structural map and data of the surveyed area in the Rotondo granite. (a)
 274 Structural field map of the southern rim of the Rotondo Granite summarizing the field
 275 observations and showing the location of investigated areas (modified after Berger et al., 2017).
 276 (b-i) Equal area, lower-hemisphere stereographic projections of the structural data for each set of
 277 deformation structures. Great circles: slip planes (S); Dots and contour: lineations (L). Blue and
 278 red planes and dots represent dextral and sinistral kinematics, respectively. Contours are
 279 calculated as Area percentage, minimum contour is 5 area% - computed with Stereonet 11
 280 (<https://www.rickallmendinger.net/stereonet>). (b) D₁ shear fractures, cataclasites and breccias;

281 (c) D₁ plane-parallel thick quartz veins; (d) D₂ ductile shear zones, dip-slip, top-to-SE reverse
 282 kinematics; (e) low-angle quartz veins kinematically related to D₂ shear zones; (f) D_{3A} ductile
 283 shear zones (black great circles) showing strike-slip reactivation and associated extensional wing
 284 cracks (EWC) and quartz-veins developed in dilational jogs (orange great circles); (g) D_{3B}
 285 conjugate, brittle-ductile shear zones (solid great circles) and extensional veins (dashed great
 286 circles); (h) D_{3C} normal faults; (i) D₄ Zeolite- and gouge-bearing brittle fault zones.

287 4.1.1. D₁ brittle shear fractures, cataclasites and breccias

288 The D₁ set consists of brittle shear fractures (Fig 3a), cataclasites (Fig. 3b) and breccias
 289 (Fig. 3c-d) containing a dark, fine-grained matrix that surrounds angular clasts of undeformed
 290 granite (Fig. 3c-d). Milky quartz veins are common along these structures, ranging in thickness
 291 from a few mm (Fig. 3e), to >1 m (Fig. 3e-f), and showing mutual overprinting relationship with
 292 the dark fine-grained matrix (Fig. 3e-h). In some cases, large breccia bodies are observed,
 293 characterized by a transitional texture from crackle-breccias to fine grained cataclasites. A
 294 peculiar feature of D₁ structures is the occurrence of mm-size garnets overgrowing the dark
 295 matrix (Fig. 3b,c,d,g). D₁ structures are steeply dipping, SE-verging, and ENE-WSW-striking
 296 (Fig. 2b-c). A subset of D₁ cataclasites (23 planar measurements) presents an orientation at high
 297 angle to the main set (Fig. 2b). The kinematics of set D₁ structures is rather difficult to constrain,
 298 given that they are overprinted by the following stage of ductile deformation. A dip-slip lineation
 299 L₁ is observed on the exposed surface of the matrix (Fig. 3g), and incipient breccias and shear
 300 fractures commonly show either strike-slip dextral or normal-sense displacement of crosscut
 301 markers in the present orientation (Fig. 3h). Garnet is only observed in D₁ structures not heavily
 302 overprinted by the ductile deformation related to D₂ shear zones (Fig. 3b-c).

303 4.1.2. D₂ Dip-slip, reverse ductile shear zones

304 The D₂ set consists of mylonitic ductile shear zones. D₂ shear zones exploit as nucleation
 305 site the pre-existing structural and/or compositional heterogeneities in the host Rotondo granite,
 306 such as aplitic and mafic dykes, veins, and D₁ structures (Fig. 4). Deformed aplitic and mafic
 307 dykes develop an oblique homogeneous foliation abruptly terminating at the dyke selvage
 308 against the undeformed host RG. D₂ shear zones exploiting D₁ brittle structures preserve the
 309 geometric and textural complexity of the precursor, developing an heterogeneous Bt-Wm-
 310 bearing foliation wrapping around low-strain granite clasts and lithons (Fig. 4b). D₂ structures
 311 strike ENE-WSW, showing a dip-slip, L₂ Bt-Wm-bearing lineation (Fig. 2d). The dominant
 312 kinematics is reverse, top-to-SE, even though dip-slip normal kinematics are observed on rare
 313 SE-steeply-dipping shear planes. Overall, the D₂ ductile shear zones form a large-scale network
 314 defined by subparallel zones of high strain surrounding high-aspect-ratio lozenges of
 315 undeformed granite (Gapais et al., 1987). Sheared quartz + calcite veins are common in high
 316 strain D₂ ductile shear zones (Fig. 4a; see also Fig. 11 of Rast et al. 2022). Locally, calcite-rich
 317 shear zones are observed, showing thick homogeneous calcite-rich layers close to layers clearly
 318 resembling sheared calcite-bearing breccias (Fig. 4d). A set of shallowly NW-dipping quartz +
 319 feldspar veins and non-mineralized joints also occur (Figs. 2e, 4b), and commonly abut major
 320 mylonitic shear zones, with vein tips dragged into the main mylonitic foliation (Fig. 4b).

321 4.1.3. D₃. Strike-slip, brittle-ductile shear zones

322 D₃ structures include: (i) D_{3A}, strike-slip mylonitic shear zones reactivating pre-existent
 323 D₁-D₂ structures; (ii) D_{3B}, a set of conjugate, brittle-ductile strike-slip faults; (iii) D_{3C}, a set of

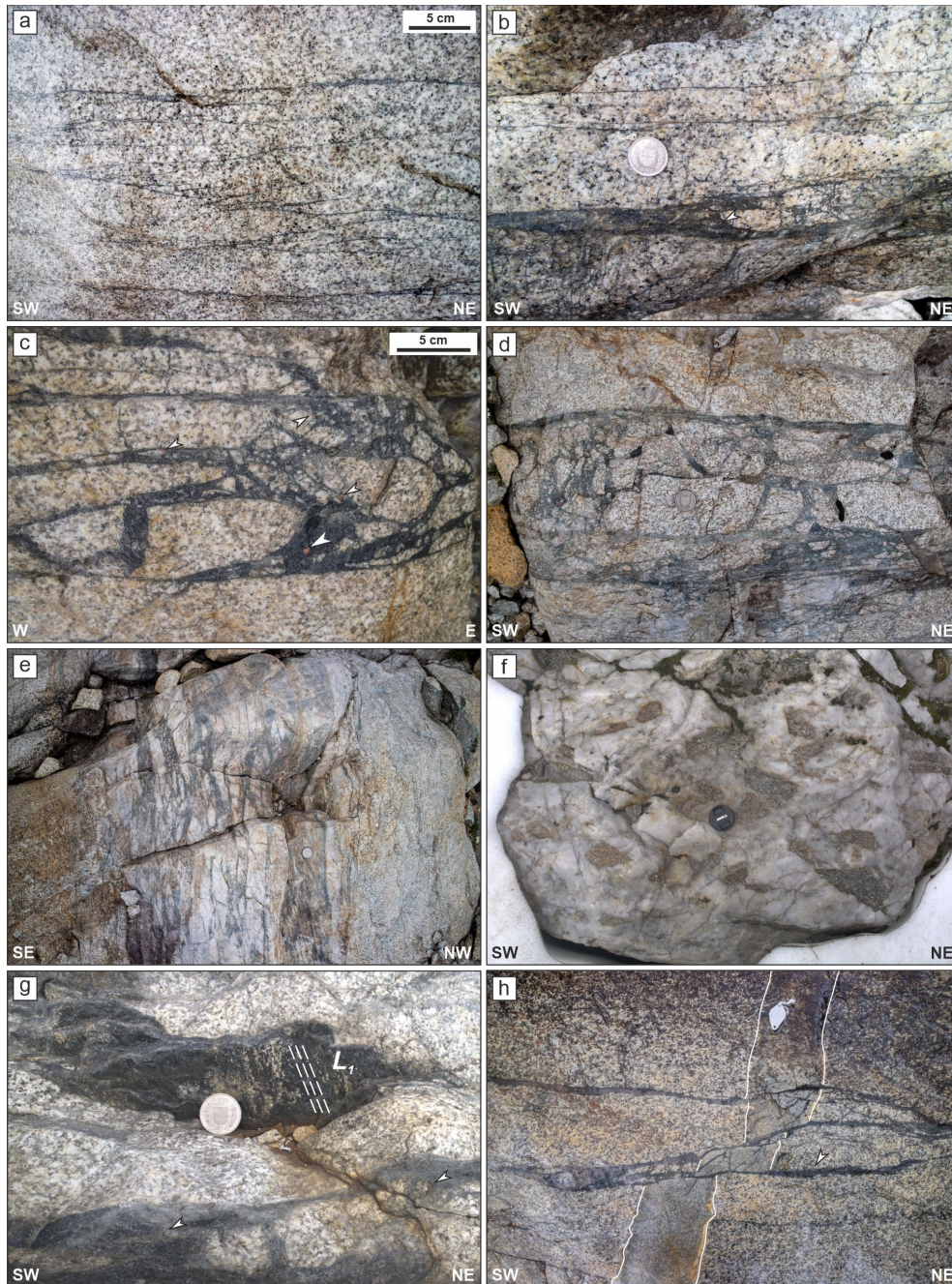
324 conjugate, normal dip-slip faults. D₁-D₂ structures are reactivated under brittle-ductile conditions
325 with a dominant strike-slip kinematics (Fig. 4e-h), as inferred from the development of a sub-
326 horizontal L_{3A} lineation overprinting the pre-existing dip-slip L₂ (Fig. 4e). The orientation of D_{3A}
327 structures reflects the pre-existent ENE-WSW mylonitic shear zones (Fig. 2f). A heterogeneous
328 S-C fabric is developed in major mylonitic zones, showing dominant dextral kinematics (Fig. 4e-
329 f, same outcrop of the shear zone a few meters far from Fig. 4a). Tensile wing cracks (Figs. 4g,
330 2f), brecciated dilational jogs (Fig. 4h), and quartz + feldspar veins develop at high angle to D₁-
331 D₂ shear fractures and mylonites during re-shearing under strike-slip orientations. These veins
332 and dilational breccias can be distinguished from previous D₁ quartz-veins and breccias based on
333 their orientation and their content of coarse quartz clear crystals.

334 The D_{3B} structures consist of brittle-ductile discrete faults and mylonites, arranged in
335 conjugate sets (Fig. 5a). N-S-striking set of sinistral, strike-slip fault planes is conjugated to a
336 WNW-ESE-striking set of dextral strike-slip fault planes (Fig. 2g). In both cases, the L_{3B}
337 lineation is oblique (Fig. 2g), shallowly plunging toward ENE or WNW, respectively. The
338 conjugate fault sets crop out in low-strain domains bounded by major D_{3A} shear zones. A very
339 localized mylonitic foliation is observed along the discrete fault planes. The conjugate set of
340 brittle-ductile faults is associated with subvertical, NW-SE-striking tensional Qz + Chl + Wm +
341 Py + Hem veins (Fig. 5a). Such mineralization and veins are observed also in extensional jogs
342 between overlapping en-echelon fault segments (Fig. 5a). Episyenites (i.e., quartz-depleted,
343 vuggy altered granites) are observed close to mineralized veins and shearing planes
344 (Pennacchioni et al., 2016).

345 D_{3C} structures consist of NW-SE striking faults with a dip-slip, Qz + Wm-bearing L_{3C}
346 lineation with normal kinematics (Figs. 5b, 2h). They occur as discrete shear planes, with a near-
347 constant spacing on the m-scale (Fig. 5b). They crop out mainly in the southern part of the RG,
348 and they are less developed elsewhere. The dominant set of shear planes dips NE, with a pure
349 dip-slip L_{3C} lineation. Conjugate, SW-dipping shear planes with normal kinematics also occur. In
350 some cases, the shear plane is also characterized by a weak ductile foliation in the host rock. D_{3C}
351 shows mutual crosscutting relationships with D_{3B} structures.

352 4.1.4. D₄ Zeolite- and gouge-bearing brittle faults

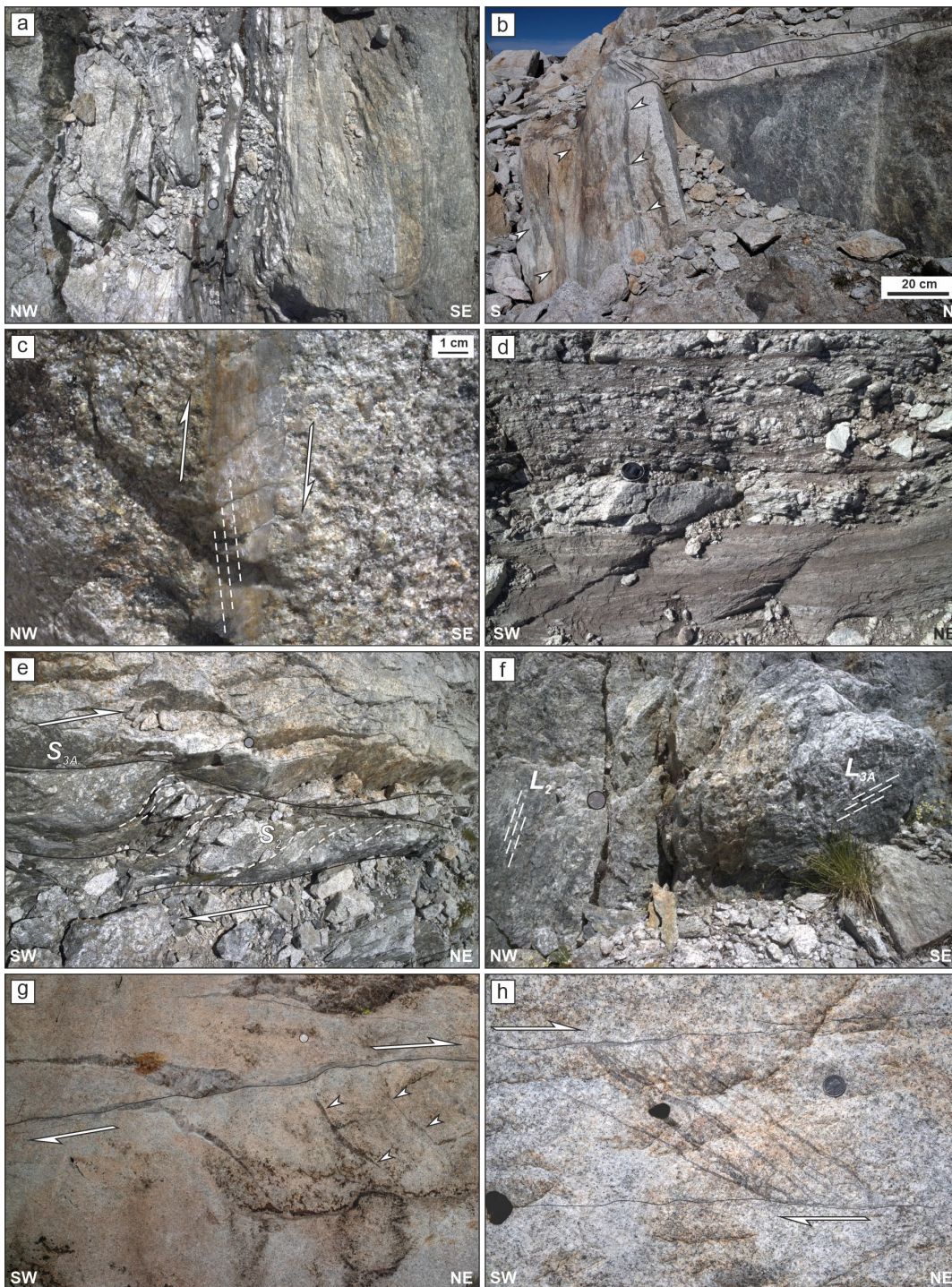
353 The latest set of deformation structures D₄ includes zeolite- and gouge-bearing brittle
354 faults (Fig. 5c-d). They form gullies and valleys in the topography of the RG, and thus their
355 exposure is very limited and, when present, badly preserved. When observed, the L₄ lineation is
356 subhorizontal, consistent with a dominant dextral kinematics inferred from the few planes
357 showing offset markers (Fig. 2i). Zeolite-bearing, fine-grained breccias are observed on
358 anastomosing planes exploiting pre-existent D₁ shear fractures. Gouge-bearing fault zones are
359 observed to develop at the contact between major quartzo-feldspathic mylonites and the
360 undeformed granite (Fig. 5c-d). D₄ structures exploit pre-existent structural discontinuities, and
361 the structural data in Fig. 2i show that D₄ structures actually reactivate and exploit the entire set
362 of pre-existent structures.



363 **Figure 3.** D₁ structures. Note that D₁ brittle structures contain clast and lithons only of
 364 undeformed granite. White arrow points to garnet in the matrix. (a) Set of quartz-biotite-bearing
 365 shear fractures showing en-echelon spatial arrangement (Wp004). (b) A cataclasite, showing
 366 limited ductile reactivation and preserving angular clasts of undeformed granite (Wp078). (c-d)
 367 Example of breccias (outcrop of sample ACB35; Wp149). (e) Sheared breccia showing moderate
 368 ductile reactivation and sheared clasts (resulting from the reworking of a thick quartz vein
 369 (Wp149). (f) Thick, plane-parallel quartz vein preserving breccia structures and undeformed
 370 granite clasts (Wp051). (g) Example of lineated surfaces in the breccia matrix (Wp149). (h)

371 Cataclasites displacing with dextral (and normal) strike-slip kinematics a subvertical pegmatitic-
372 aplitic dyke. Handlens (3 cm) for scale.

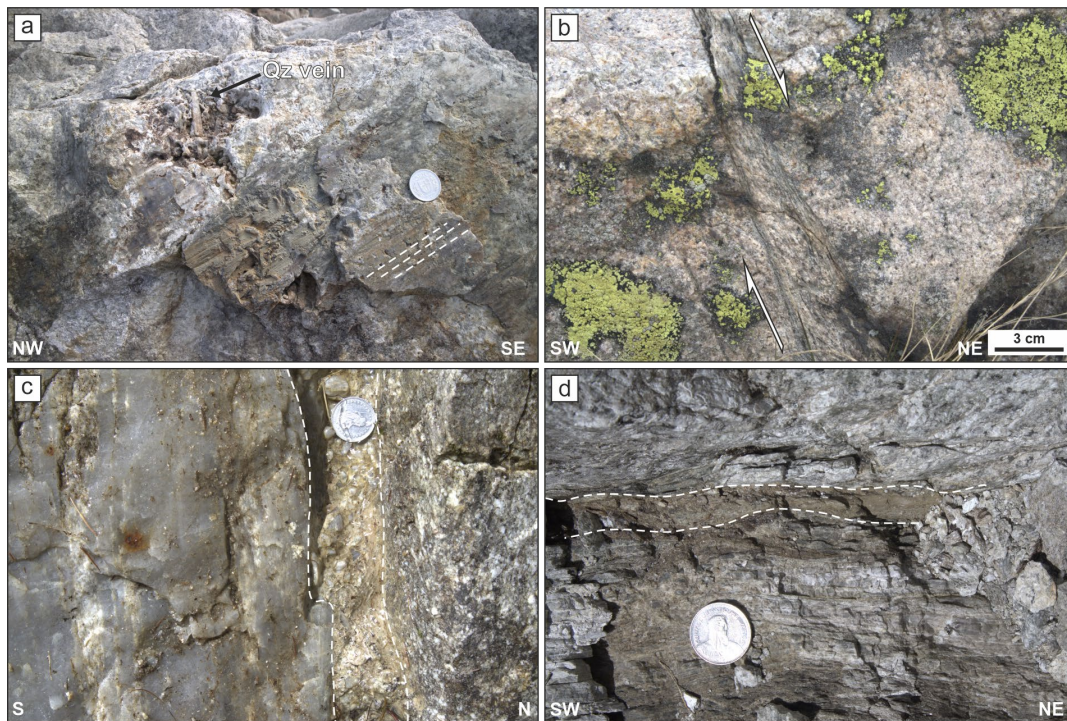
373



374

375 **Figure 4.** D2-D3 structures. (a) Dip-slip D2 shear zone localized on a mafic dyke, parallel
376 to a set of D1 shear fractures (left hand side of the image) and characterized by the pervasive

377 occurrence of sheared quartz + calcite veins. (Wp170). (b) Heterogeneous D₂ ductile shear zone
 378 (foliation marked by white arrows) with reverse kinematics and the associated low-angle Qz-vein
 379 (black arrows) (Wp087). (c) Sheared D₂ quartz + feldspar vein showing homogeneous internal
 380 foliation, suggesting top-to-SE reverse kinematics (Wp020). (d) D₂ calcite-bearing mylonite
 381 showing the boundary between a homogeneous calcite-mylonite (bottom) and a sheared breccia
 382 (top) with granitoid clasts (Wp182). (e) D_{3A} mylonitic shear zone showing S-C fabric related to
 383 strike-slip reactivation of a former dip-slip D₂ ductile shear zone (Wp171). (f) Detail of the D_{3A}
 384 shear zone reported in (e) showing the occurrence of the L_{3A}, strike-slip lineation and the L₂-dip-
 385 slip lineation on adjacent shear planes; L_{3A} lineation occurs on S-C planes of the mylonitic shear
 386 zone wrapping around lensoid domains where L₂ is still preserved. (g) D_{3A} shear fractures,
 387 showing the development of quartz + feldspar wing cracks suggesting dextral strike-slip
 388 reactivation (Wp178). (h) D_{3A} brecciated dilational jog between two reactivated D₁ shear
 389 fractures (Wp137).



390

391 **Figure 5.** D₃-D₄ structures. (a) D_{3B} shear plane of a sinistral brittle-ductile fault, showing
 392 the oblique L_{3B} lineation and the occurrence of mineralized jogs (quartz vein) (Wp092). (b) D_{3C}
 393 brittle-ductile normal fault characterized by cm-scale heterogeneous foliation along the shear
 394 plane. (c) D₄ zeolite-bearing cataclasite (delimited by dashed white curves) localized at the
 395 contact between a major quartzo-feldspathic D₂ mylonite (left-hand side of the picture) and the
 396 undeformed granite (right-hand side of the picture, Wp047). (d) D₄ gouge-bearing fault localized
 397 on D₂ mylonitic foliation (Wp158).

398

399

400 4.2 Microstructures & petrochronology

401 We report here the results of microstructural, chemical and petrochronological
 402 characterization of representative samples from three of the four classes of deformation
 403 structures, including: (i) ACB35, D₁ brittle breccia (Fig. 3d-e); (ii) ACB27a, major dip-slip D₂
 404 ductile shear zone with tip-to-SE kinematics; (iii) ACB37b, D_{3A} brittle-ductile shear zones with
 405 dextral strike-slip reactivation (Fig. 4f). Microstructure and petrography are presented together
 406 with the mineral composition obtained from EPMA. Representative mineral compositions,
 407 diagrams, and bulk rock chemical compositions are reported in the SI Tables S2-S3, and in SI
 408 Fig. S3.

409 4.2.1. Microstructures, mineral paragenesis and pseudosection calculations

410 4.2.1.1. D₁ Qz-Bt-bearing breccia

411 D₁ breccias are composed of cm-size angular granite clasts, weakly flattened and
 412 sheared, embedded in a fine-grained matrix showing homogeneous grain size and a weak
 413 pervasive foliation defined by Bt (Fig. 6b). The matrix mineral paragenesis in ACB35 includes
 414 Qz + Bt (Mg# = 0.40-0.45; Ti = 0.02 apfu) + Kfs + Grt + Ep/Aln + Ab ± Pl ± Wm ± Chl + Ap +
 415 Zrc + Nb-Y-REE oxides and silicates (Gadolinite group). Rare Mnz grains are observed scattered
 416 in the recrystallized matrix. Grt crystals range from 100 μm to 5-10 mm, showing a wide range
 417 of crystal morphologies, from euhedral grains containing angular inclusions (Fig. 6a), to grains
 418 showing anhedral shapes, resorbed rims, and poikiloblastic/honeycomb textures (Fig 6b). In most
 419 samples of pristine D₁ breccia, euhedral Grt includes a random pattern of Qz + Pl + Kfs angular
 420 inclusions with no shape preferred orientation (Fig. 6a). These inclusions are only preserved
 421 within euhedral garnets and are here interpreted to reflect the fine-grained cataclastic matrix of
 422 the D₁ breccia on which Grt grew. There is no evidence of Grt growth and shearing coeval with
 423 D₁ brecciation. Grt grains containing angular inclusions are typically enveloped by a weak
 424 mylonitic foliation overprinting the breccia matrix (Fig. 6a-b). In some cases, Grt is weakly
 425 pleochroic, suggesting a non-cubic crystal symmetry (e.g., Cesare et al., 2019). The Grt in
 426 sample ACB35 shows an elongated shape, parallel to the foliation, with an honeycomb texture,
 427 characterized by a heterogeneous distribution of oriented inclusions (Fig. 6b). The inclusions are
 428 mainly euhedral Ep and Aln with a peculiar texture (Fig. 6c-d). Aln is observed at the core,
 429 surrounded by Ep forming the euhedral rim (Fig. 6d). Ep in the recrystallized breccia matrix
 430 shows a concentric, rhythmic zoning with brighter rims, without Aln cores (Fig. 6e-f). Ep
 431 aggregates in the recrystallized matrix contain spongy Zrc crystals, and partially destabilized
 432 Thorite-Xenotime at their core (Fig. 6f).

433 Grt compositional variability in this structural domain ranges from Alm₃₆Sps₃₀Grs₃₂Prp₂
 434 (Grt_A) to Alm₃₆Sps₂₆Grs₃₆Prp₂ (Grt_B), describing a smooth gradient from the inclusion-free layer
 435 (Grt_A in Fig. 6c) toward the outer, inclusion-rich rims with honeycomb microstructure (Grt_B in
 436 Fig. 6c).

437 Garnets with similar compositions are also observed in sheared D₁ shear fractures and
 438 veins (samples ACB_Sp3d and ACB18, Alm₃₄₋₄₁Sps₂₆₋₁₈Grs₃₈₋₃₉Prp₁; Fig. 6b; SI Fig. S2a). Grt in
 439 ACB35 shows resorbed rims and embayment at the contact with the sheared granular matrix and
 440 phyllosilicates, indicating that Grt is likely metastable in the sheared mineral paragenesis (Fig.
 441 6b-d).

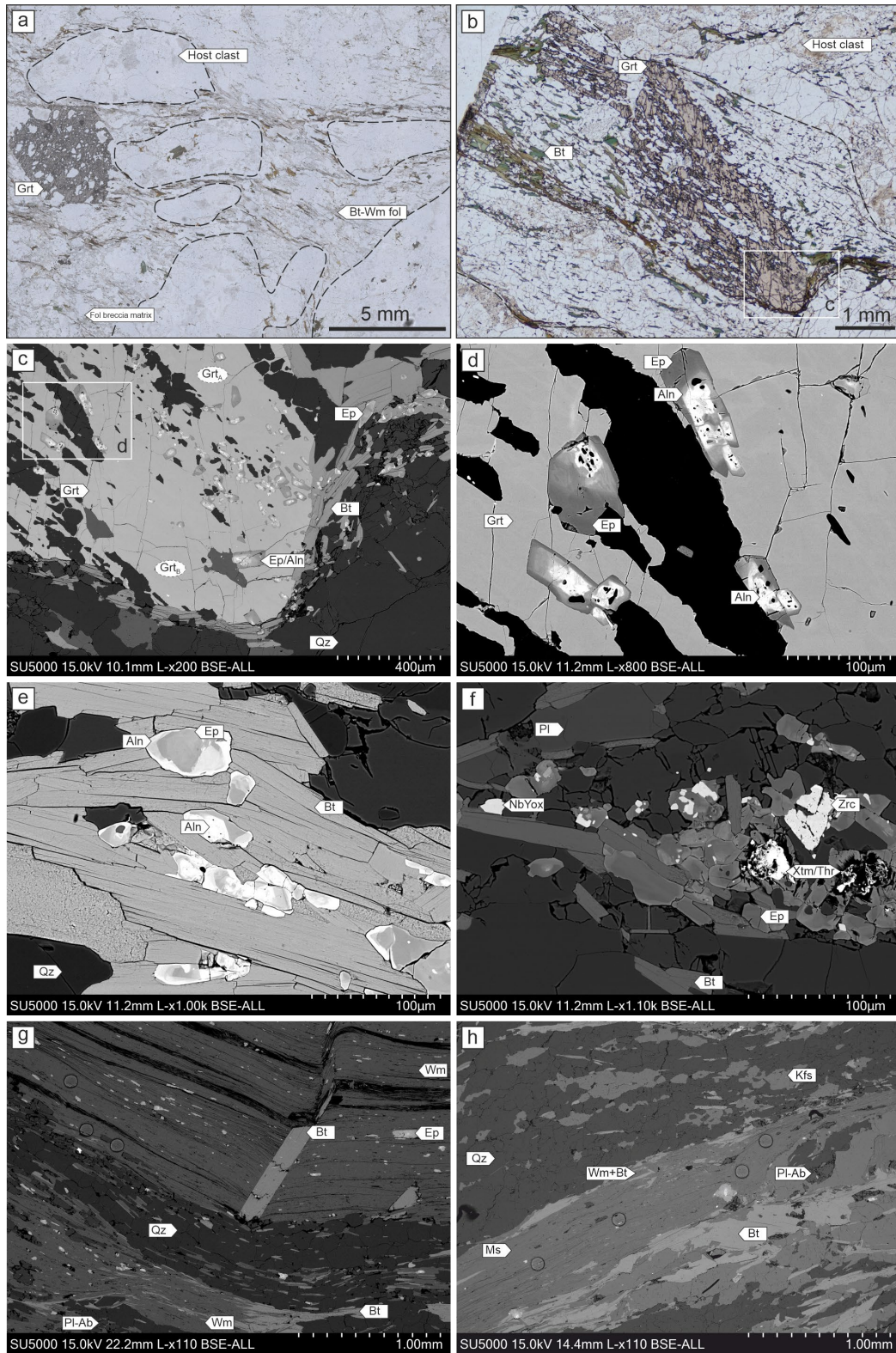
442 The pseudosection for sample ACB35 was computed with an H₂O amount equal to the
 443 LOI content retrieved from XRF analyses (SI Table S2; Fig. 7a). The bulk composition adopted
 444 for the calculation reflects the recrystallized matrix of the breccia. Its composition is highly
 445 enriched in SiO₂ compared to the undeformed granite (SI Table S3). The observed paragenesis
 446 Qz + Bt + Kfs + Grt + Ep + Ab is computed to be stable over a wide range of *P-T* conditions (*T*
 447 < ~550 °C, *P* < 0.9 GPa). The variation of computed Bt composition is limited and not useful to
 448 further constrain *P-T* conditions of apparent equilibrium. The observed Grt_A and Grt_B
 449 compositions are computed to be stable at *T* = 590 ± 10 °C, and *P* = 0.94 GPa for Grt_A, *P* = 1.02
 450 GPa for Grt_B. However, under those conditions, Ep and Ab are not stable. This misfit between
 451 observed and computed paragenesis suggests that the observed paragenesis might be metastable,
 452 preserving a porphyroclastic Grt in a recrystallized and equilibrated fine-grained matrix. In any
 453 case, similar *P-T* estimates are retrieved from pseudosection calculations using samples ACB18
 454 (590 ± 25 °C, 1.0 ± 0.1 GPa), as well as ACB25 (575 ± 15 °C, 0.9 ± 0.1 GPa), the latter
 455 representing the seared contact between granite and the host rock (SI Text S2-S3).

456 4.2.1.2. D₂ Dip-slip, reverse shear zones

457 The sample ACB27a represents a high-strain domain of a D₂ ductile shear zone. D₂
 458 ductile shear zones are characterized by a pervasive and homogeneous mylonitic foliation
 459 including Qz + Kfs + Wm (Si = 6.6-6.8) + Ep/Aln + Bt (Mg# = 0.55; Ti = 0.04 apfu) + Ab ± Pl
 460 enveloping mm-sized Wm + Bt porphyroblasts (Fig. 6g). The pseudosection was computed
 461 adopting an H₂O amount as obtained from the LOI content retrieved from XRF analyses (Fig.
 462 8a). The observed paragenesis Qz + Bt + Wm + Kfs + Ep + Ab is computed to be stable over a
 463 wide range of *P-T* conditions, at H₂O-saturated conditions. Computed Wm(Si) is comparable to
 464 the observed composition. Considering the observed Wm(Si), Bt(Ti) = 0.03 and Bt(Mg#) > 0.5,
 465 the stability field of the observed paragenesis is constrained to *T* = 520 ± 40 °C and *P* = 0.83
 466 ± 1.25 GPa.

467 4.2.1.3. D₃ Strike-slip, dextral shear zones

468 The ACB37b mineral paragenesis includes Qz + Kfs + Wm + Bt (Mg# = 0.58; Ti = 0.05
 469 apfu) + Pl + Ab + Ep/Aln + Ap ± Chl (Fig. 6h). The main foliation is defined by anastomosing
 470 S-C shear planes of fine-grained Wm, incorporating Bt and Ep/Aln inclusions, wrapping around
 471 recrystallized Qz + Pl + Ab + Kfs lenses. Wm(Si) is rather variable, forming two main
 472 compositional groups which have no microstructural correspondence: Wm(Si)₁ = 6.40 apfu and
 473 Wm(Si)₂ = 6.65-6.85 (SI Fig. S3a-b). The pseudosection has been computed at H₂O-saturated
 474 conditions (Fig. 8b). The observed paragenesis is stable over a wide range of *P-T* conditions.
 475 Computed Wm(Si)₁, and Bt(Ti) isopleths define a field centered at *T* = 395 ± 25 °C and *P* =
 476 0.4 ± 0.1 GPa. The variability of the computed Bt(Mg#) is rather limited (0.52-0.55) and slightly
 477 underestimates the observed composition. Spn is predicted in very small amounts (>1 vol%) but
 478 not observed.



479

480 **Figure 6.** Microstructures of the analyzed deformation zones. (a) Optical plane-polarized
 481 light micrograph of D₁ breccias. Note the occurrence of the random pattern of inclusions in Grt
 482 formed by angular clasts. Dashed curves delimit mm-to-cm clasts of the host granite. (b) Optical

483 plane-polarized light micrograph of the recrystallized matrix of a D₁ breccia (sample ACB35),
 484 showing the analyzed honeycomb Grt. (c) BSE image of Grt in sample ACB35 showing the
 485 alignment of Ep/Aln inclusions. See text for explanations. (d) BSE image of the Ep/Aln
 486 inclusions in the Grt of sample ACB35, showing the Aln, inclusion-rich cores with resorption
 487 textures and euhedral Ep rims. (e) BSE image of Ep crystals included in Bt in the fine-grained
 488 matrix of sample ACB35, showing rhythmic zoning between Ep-rich and Aln-rich layers. (f)
 489 BSE image of Ep aggregates along the mylonitic foliation in sample ACB35, including Zircon
 490 (Zrc), Nb-Y-oxides (NbYox), and Xtm/Thr aggregates likely resulting from the destabilization of
 491 Monazite. (g) BSE image of sample ACB27a showing the Wm porphyroblast and mylonitic
 492 foliation. Note the craters due to laser ablation analyses. (h) BSE image of the mylonitic foliation
 493 of sample ACB37b showing the occurrence of fine-grained aggregates of Wm + Bt. Note the
 494 craters due to laser ablation analyses.

495 4.2.2. In-situ U-Pb on Garnet

496 We report here the results of U-Pb and trace element analyses from a set of samples
 497 representing D₁ breccias (ACB35; ACB_Sp8; ACB_Sp7), and sheared Qz-veins and fractures
 498 (ACB18, ACB_Sp3) (Fig. 6; SI Fig. S2).

499 The analyses of Grt in ACB35 show two distinct populations, defining two separate
 500 trends in a Tera-Wasserburg concordia diagram (Fig. 7b). A first population of U-Pb data forms
 501 a linear array defining a lower intercept age of 128.0 ± 9.3 Ma (n=26, MSWD=2.9). A second
 502 population can be fitted by a regression line with a lower intercept corresponding to an age of
 503 34.0 ± 4.4 Ma (n=25, MSWD=2.8). The combination of U-Pb ratios and trace element
 504 concentrations reveals that the first population contains elevated Zr amounts (up to 7000 ppm),
 505 which are indicative of contamination of the analysis by ablation of zircon inclusions in the
 506 garnet. As shown in the trace element maps of Fig. 7c, some of the ablation spots fall adjacent to
 507 or on top of Grt areas where high amounts of Zr are detected. Therefore, to avoid contamination
 508 artifacts, we have excluded from the final age calculation all the U-Pb data with Zr content >20-
 509 30 ppm (depending on the sample). This approach filters out the anomalously old, spurious U-Pb
 510 intercept age (~128 Ma) defined above.

511 The pooled lower intercept Tera-Wasserburg age obtained from analyses of several small
 512 (inclusion-free) Grt grains for this (ACB35) and the other samples are reported in Table 1. Other
 513 samples range between 26.9 ± 1.3 Ma (n=54, MSWD=1.9) for ACB_Sp3b (Fig. 7e), and $20.1 \pm$
 514 1.0 Ma (n=33, MSWD=0.86) for ACB_Sp8d (Fig. 7f). Additional details of U-Pb analyses,
 515 including Tera-Wasserburg plots, are reported in the SI Text S2 and Fig. S2.

516 The REE patterns of analyzed garnets (Fig. 7d) are characterized by a high variability in
 517 REE contents, ranging between two end members (Grt-Type1 and Grt-Type2 in Fig. 7d inset).
 518 Grt-Type1 is characterized by significant depletion of LREE with a negative anomaly of Ce, and
 519 a steep HREE slope. Grt-Type2 is characterized by a rather flat LREE-HREE profile, along with
 520 a low Sm/La (Fig. 7d). In addition, the ablation maps reveal a weak trace element zoning in Grt
 521 (Fig. 7c). A similar variation in LREE content is also observed in samples ACB18, ACB_Sp3b,
 522 ACB_Sp8c/d, ACB_Sp7d (Fig. 7d).

524 **Figure 7.** *P-T-t* data for sample of D1 structures. (a) Computed pseudosections for
 525 sample ACB35; (b) Tera-Wasserburg (TW) diagram of U-Pb garnet and trace element data for
 526 samples ACB35, showing the two populations of data, with analyses plotted according to their Zr
 527 content. (c) Laser ablation maps for selected isotopic masses, including ^{55}Mn , ^{31}P , ^{90}Zr , ^{139}La ,
 528 ^{172}Yb , ^{238}U , on ACB35 Grt (see area delimited in Fig. 6b). (d) Chondrite-normalized
 529 (McDonough and Sun, 1995) REE-patterns of the analyzed Grt in samples ACB35, ACB18,
 530 ACB_Sp3b, ACB_Sp7c, ACB_Sp8c/d; the inset shows the compositions of the two identified
 531 end-members (Grt-Type1, Grt-Type2) characterized by either flat LREE or steep LREE profile.
 532 (e -f) TW diagram for Grt in ACB_Sp3b and ACB_Sp8d, respectively.

533 4.2.3. In-situ Rb-Sr on white mica and biotite

534 We report here the results of in-situ Rb-Sr analyses of white mica defining the main
 535 foliation in the samples ACB27a, ACB37b, already described before, as well as in an additional
 536 sample ACB12b. Then, Rb-Sr data for biotite in the undeformed granite B19-1417 are presented.

537 4.2.3.1. D₂ Dip-slip, reverse shear zone

538 In ACB27A the mica grains show a large spread in $^{87}\text{Rb}/^{86}\text{Sr}$ from 119 to 3125 with
 539 corresponding variations in $^{87}\text{Sr}/^{86}\text{Sr}$ between 0.82 and 1.42 ($n = 39$). A regression through these
 540 data generates an isochron with a slope corresponding to an age of 18.1 ± 0.9 Ma (2se, $n = 38/39$,
 541 MSWD = 1.5) and a $^{87}\text{Sr}/^{86}\text{Sr}$ intercept of 0.799 ± 0.010 (Fig. 7e).

542 4.2.3.2. D₃ Strike-slip, dextral shear zone

543 The analyses of mica in sample ACB37B provide different age results. Most of the
 544 analyzed grains cluster at $^{87}\text{Rb}/^{86}\text{Sr}$ between 700-1000 with four measurements extending to
 545 higher $^{87}\text{Rb}/^{86}\text{Sr}$ (up to 3030) and one to lower $^{87}\text{Rb}/^{86}\text{Sr}$ (4.1). $^{87}\text{Sr}/^{86}\text{Sr}$ values are similarly
 546 clustered between 0.86 and 0.99 with three higher (up to 1.44) and one lower value (0.77). The
 547 corresponding Rb-Sr isochron provides an age of 14.7 ± 1.5 Ma and an initial $^{87}\text{Sr}/^{86}\text{Sr}$ of 0.767
 548 ± 0.018 ($n = 35$, MSWD = 1.3; Fig. 7f). These values change marginally if the high Sr analysis,
 549 for which contribution by a Sr-bearing phase is likely, is removed (e.g., 13.1 ± 2.1 Ma).

550 4.2.3.3. D₂ bulk foliation in RG₂ granite

551 Sample ACB12b represents the foliated RG₂ granite, where the Wm-bearing bulk
 552 foliation wraps around the porphyric Kfs and the partially recrystallized quartz domains. The
 553 recrystallized matrix along the foliation is mainly composed of Qz + Wm + Ab + Ep. White mica
 554 shows limited $^{87}\text{Rb}/^{86}\text{Sr}$ spread (≤ 352) including two relatively low values of 8.0 due to ablation
 555 of Sr-rich impurities. $^{87}\text{Sr}/^{86}\text{Sr}$ is also limited compared to the previous samples (≤ 0.83) with
 556 $^{87}\text{Sr}/^{86}\text{Sr}$ of 0.73 for the two low-Rb/Sr samples. The age of the Rb-Sr isochron (18.6 ± 1.9 Ma; n
 557 $= 35$; MSWD = 0.76; $^{87}\text{Sr}/^{86}\text{Sr}_i = 0.729 \pm 0.005$) is largely constrained by the two low Rb/Sr
 558 analyses. Exclusion of these two analyses returns a similar although much less precise of $16.3 \pm$
 559 3.7 Ma. For all these samples (ACB27a, ACB37b and ACB12b) we prefer to consider the more
 560 precise isochron ages that include the high-Sr analyses because the high Sr impurities included in
 561 these analyses appear to be sourced from minerals (epidote) cogenetic with mica.

562

4.2.3.4. Undeformed RG₁ granite

563

564

565

566

567

568

Sample B19-1417 represents the undeformed RG₁ granite. Biotite in this undeformed granite provides similar ages to those of white mica in sheared sample ACB37B. This biotite shows very high and highly variable ⁸⁷Rb/⁸⁶Sr (2350-45720) corresponding to elevated ⁸⁷Sr/⁸⁶Sr between 1.22 and 10.5. The large spread in Rb-Sr data point results in a relatively precise isochron corresponding to an age of 15.2 ± 0.7 Ma (n = 28/30; MSWD = 0.34) but a poorly defined ⁸⁷Sr/⁸⁶Sr intercept of 0.68 ± 0.11 (Fig. 8f).

569

570

571

572

Biotite in RG₁ (sample B19-1417), foliated RG₂ (sample ACB14c, SI Text S4, Fig. S4) and D₂ localized shear zone in RG₂ (sample ACB3b, SI Text S4, Fig. S4) yielded indistinguishable ages (Table 1) which are all within uncertainty of the Rb-Sr age of white mica from the D_{3A} localized shear zone (Fig. 8d).

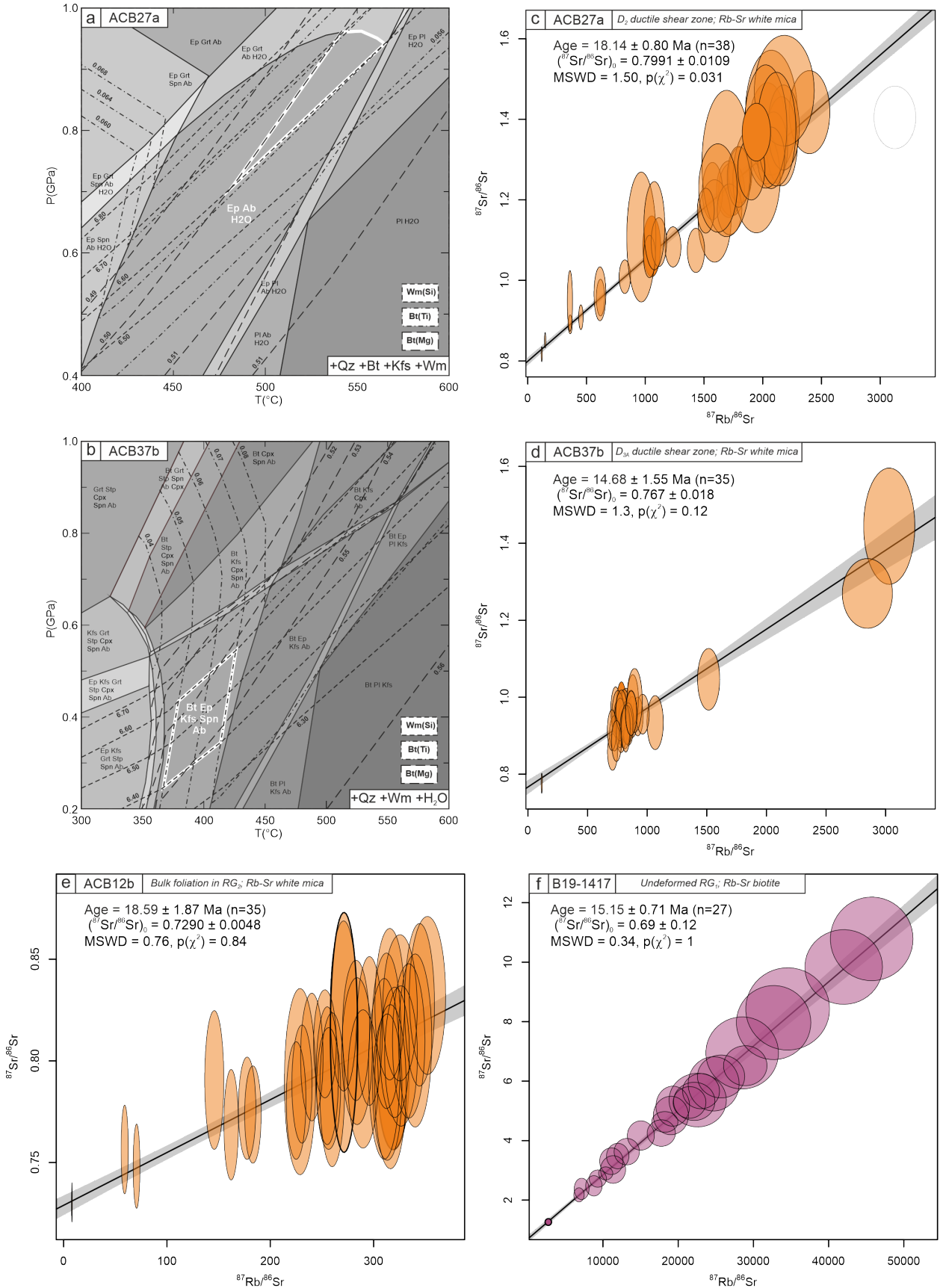
573

574

Sample	Description	Lower Intercept Age (Ma)	Uncert. Int. (±2σ, Ma)	Uncert. With Ssys (±2σ, Ma)*	Relative Uncertainty (±2σ, %)	Number of analyses	MSWD	p(χ ²)
ACB18	U-Pb Grt	23.23	3.58	3.60	15.48%	45 /55	3.40	0.0
ACB35	U-Pb Grt, Zr > 25 ppm	127.97	9.08	9.28	7.25%	26 /36	2.90	0.0
	U-Pb Grt, Zr < 25 ppm	34.04	4.37	4.40	12.93%	25 /35	2.80	0.0
ACB_Sp3b	U-Pb Grt	26.92	1.25	1.31	4.88%	54 /59	1.90	0.0
ACB_Sp7b	U-Pb Grt	30.51	6.79	6.81	22.31%	57 /58	0.47	1.0
ACB_Sp8c	U-Pb Grt	24.04	2.07	2.10	8.74%	68 /71	0.92	0.7
ACB_Sp8d	U-Pb Grt	20.09	1	1.04	5.20%	33 /33	0.86	0.7
B19-1417	Bt, Undeformed RG1	15.15	-	0.71	4.69%	27 /29	0.34	1.0
ACB3b	Bt, D2 in RG1	15.25	-	0.88	5.77%	28 /30	0.65	0.9
ACB12b	Wm, Bulk RG2 fol	18.59	-	1.87	10.06%	35 /37	0.76	0.8
ACB14c	Bt, Bulk RG2 fol	15.01	-	1.17	7.79%	30 /30	0.42	1.0
ACB27a	Wm, D2	18.14	-	0.8	4.41%	38 /39	1.50	0.0
ACB37b	Wm, D3	14.68	-	1.55	10.56%	35 /36	1.30	0.1
ACB_Sp6	Bt, Bulk RG2 fol	14.77	-	0.74	5.01%	30 /30	0.65	0.9
*Systematic, long-term excess variance used for propagation is 1.5%								
Note. Samples in bold are discussed in the main text.								

575

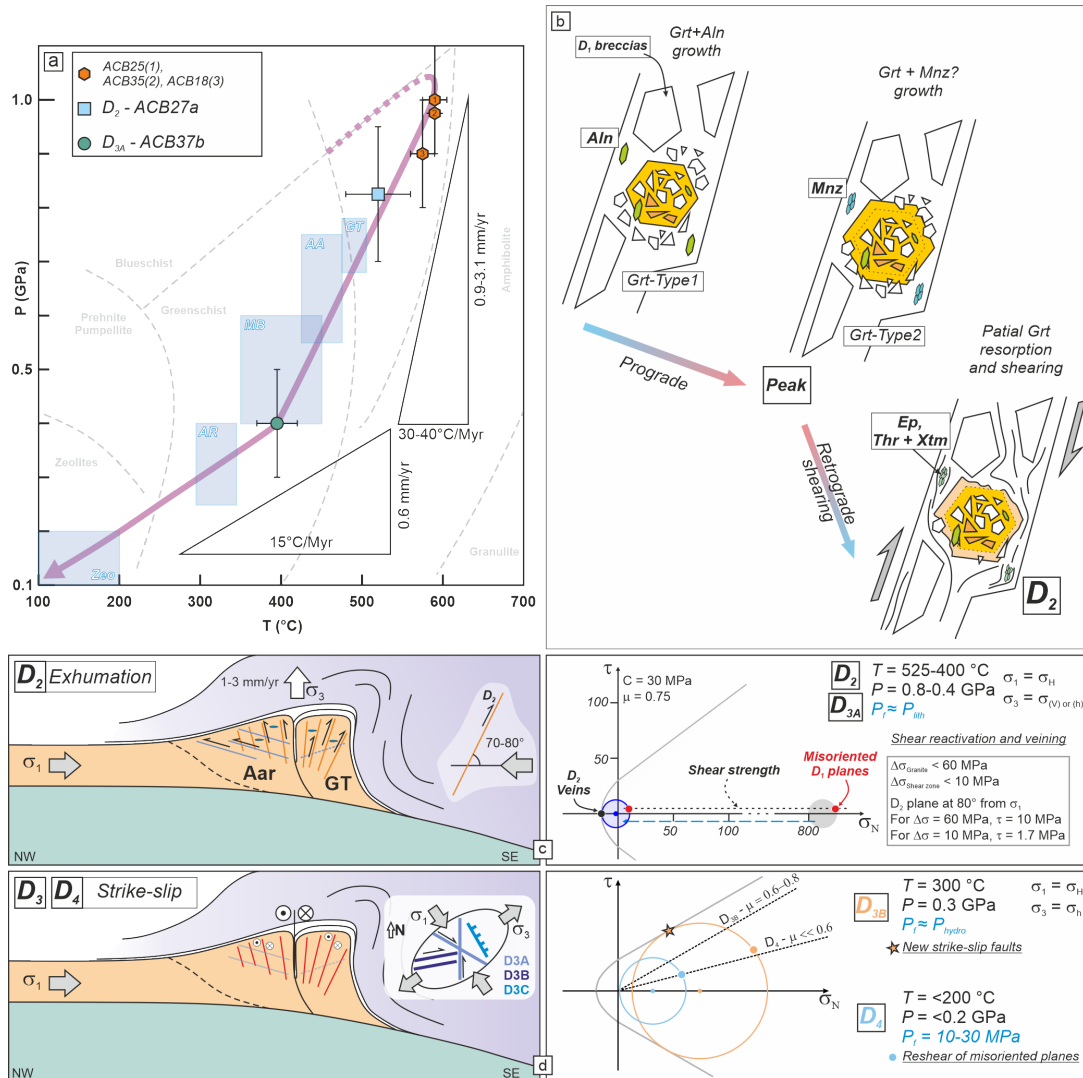
Table 1. Summary of the results from U-Pb in garnet and Rb-Sr in mica analyses.



577 **Figure 8.** *P-T-t* data for sample ACB27a-ACB37b. (a-b) Computed pseudosections for
 578 sample ACB27a and ACB37b, respectively. (c) ACB27a, (d) ACB37b, (e) ACB12b and (f) B19-
 579 1417 mica Rb-Sr isochrones including their corresponding ages (slope) and initial $^{87}\text{Sr}/^{86}\text{Sr}$
 580 composition (intercept). The size of the ellipses indicates internal 2SE (standard error).
 581 Isochronous regressions are plotted as black lines with their 95% confidence level as gray
 582 envelopes. All plots were generated using IsoplotR (Vermeesch, 2018).

583 **5. Discussion**

584 Here, we discuss and interpret the field observation and petrochronological data to (1)
 585 define the time-constrained *P-T-d* path and (2) to characterize the rheological evolution of the
 586 Rotondo granite, including the factors controlling it, during collisional tectonics.



587 **Figure 9.** *P-T-t* path for the Rotondo granite and sketch of its tectonic evolution. (a)
 588 Diagram summarizing the *P-T* conditions of deformation retrieved from thermodynamic
 589 modeling. Light blue boxes report the *P-T* conditions of peak/retrograde shear zone from other
 590 ECMs (AA: Aar/Grimsel, Goncalves et al., 2012; AR: Aiguille Rouges, Egli et al., 2017; MB:
 591 Mont Blanc: Rolland et al., 2009; GT: Gotthard-Fibbia, Oliot et al., 2014; Zeo: zeolite-faults

593 from Lützenkirchen & Loew, 2011). Exhumation and cooling rates are reported. (b) Sketch
 594 representing the possible microstructural evolution and Grt nucleation between D₁ and D₂
 595 deformation stages. See text for explanation. (c-d) Sketch (not to scale) of the tectonic and
 596 rheological evolution of the Rotondo granite and Gotthard nappe through the D₂-D₄ deformation
 597 stages. See text for explanation. σ_v : vertical principal stress; σ_H : major horizontal stress; σ_h :
 598 minor horizontal stress. Mohr plots computed with MohrPlotter
 599 (<https://www.rickallmendinger.net/mohrplotter>). GT: Gotthard nappe; Penninic a.w.: Penninic
 600 accretionary wedge.

601 5.1. P-T-t-d path and tectonic evolution

602 The *P-T-t-d* path summarizing the structural, petrochronological, and rheological
 603 evolution of the granite is presented in Fig. 9.

604 5.1.1. Brittle-to-ductile evolution and Alpine peak metamorphic conditions

605 The oldest structures observed in the granite consist of D₁ shear fractures, cataclasites and
 606 breccias. Similar brittle structures pre-dating ductile shear zones are reported from several other
 607 crystalline units of the Alps (External and Internal Crystalline Massifs: Bertini et al., 1985;
 608 Ceccato et al., 2022; Goncalves et al., 2012; Guermani & Pennacchioni, 1998; Menegon &
 609 Pennacchioni, 2010; Oliot et al., 2014; Rolland et al., 2009; Wehrens et al., 2016; Tauern
 610 Window: Leydier et al., 2019; Mancktelow & Pennacchioni, 2020; Suretta nappe: Goncalves et
 611 al., 2016). In many cases these brittle structures were interpreted to have formed in the biotite
 612 stability field, suggesting they were formed at relatively high T (>350 °C) and mid-to-lower
 613 crustal conditions (Goncalves et al., 2016; Wehrens et al., 2016). Accordingly, they have been
 614 interpreted to represent either (a) a pro-grade phase of brittle Alpine deformation (Guermani &
 615 Pennacchioni, 1998), or (b) brittle (seismic) deformation at mid-crustal depths at the Alpine peak
 616 metamorphic conditions (Leydier et al., 2019; Mancktelow & Pennacchioni, 2020; Wehrens et
 617 al., 2016). It is interesting to note that such brittle-to-ductile evolution at peak metamorphic
 618 conditions has been reported from different crystalline units across the Alps spanning the whole
 619 range of “peak metamorphic conditions” recorded for the different case studies, from sub-
 620 greenschist to high-pressure amphibolite facies (see Ceccato et al., 2022; Fig. 9a). Conversely,
 621 recent studies proposed an inherited origin for similar brittle structures occurring in the ECMs,
 622 suggesting their development during the Permo-Mesozoic rifting (Ballèvre et al., 2018;
 623 Dall’Asta et al., 2022; Herwegh et al., 2020).

624 Although we don’t have quantitative constraints on the timing or exact *P-T* conditions of
 625 formation of D₁ structures, their micro and macro-structural relationships provide several clues
 626 about their relative timing with respect to Alpine collision, and their deformation conditions. In
 627 terms of relative timing, firstly, a key observation is that D₁ structures are overprinted by D₂
 628 mylonitic shear zones without mutual cross-cutting relationship. Secondly, in the present
 629 orientation, D₁ structures are oriented at high angles (70-80°) with respect to the long-term
 630 NNW-SSE shortening direction and maximum principal stress σ_1 during Alpine convergence and
 631 D₂ reverse shearing (Fig. 9d-e). This high-angle orientation (much larger than the ~30° expected
 632 for Andersonian thrust faults) makes it difficult to explain the origin of D₁ structures as reverse
 633 brittle faults during Alpine convergence. As discussed by Herwegh et al. (2020) for similar
 634 brittle structures occurring in the Aar massif, exaggerated rotation (>60°) of the entire massif
 635 would be necessary to re-orient low-angle thrust planes into the observed D₁ orientation. Indeed,

636 such high angle orientation would be more consistent with the development of faults and
637 fractures under a strike-slip or extensional tectonic regime (Sibson, 2003). The steep orientation
638 of D₁ structures is a common feature of many of the shear zones presenting a brittle-to-ductile
639 evolution in the ECMs (e.g., Bertini et al., 1985; Guermani & Pennacchioni, 1998; Oliot et al.,
640 2014; Rolland et al., 2009; Wehrens et al., 2016; Herwegh et al., 2017, 2020). If we extrapolate
641 our observations from the Rotondo to the other massifs, the common D₁ steep orientation
642 suggests that little or no reorientation occurred regionally, and that this orientation might
643 represent an original feature of the brittle deformation structures at the regional scale. These
644 observations suggest the D₁ structures pre-date Alpine convergence, rather than being
645 synkinematic with cyclical brittle-ductile deformation at peak metamorphic conditions, as
646 instead proposed for other case studies (Herwegh et al., 2017; Mancktelow & Pennacchioni,
647 2020; Wehrens et al., 2016).

648 The geochemical and age relationships observed in Grt porphyroblasts that overprint D₁
649 structures provide further constraints on the earliest stages of Rotondo granite deformation and
650 the transition from D₁ to D₂ structures. Firstly, Grt postdates breccia formation, statically
651 overprinting the pre-existing texture (Fig. 6a). Later deformation during peak to D₂ retrograde
652 shearing led to foliation development in the matrix surrounding the Grt. The foliation-parallel,
653 elongated, and honeycomb-like crystal shapes (Fig. 6b) may suggest that Grt partially re-
654 equilibrated or crystallized synkinematically to early D₂ shearing at conditions close to peak
655 metamorphism. However, most of the D₂ shear zones do not contain Grt, probably indicating its
656 metastability during the main phase of retrograde D₂ shearing related to exhumation. Thus, we
657 define three main stages of early Rotondo evolution (Fig. 9b): (i) D₁ brecciation and cataclasis,
658 (ii) Grt growth at a post-kinematic stage relative to D₁; (iii) shearing and likely Grt
659 destabilization during D₂.

660 A diachronous two-stage evolution of Grt is supported by its REE and U-Pb systematics.
661 The two Grt compositions (Grt-Type1, Grt-Type2), characterized by different LREE patterns
662 have to be interpreted along with accessory mineral phases (Aln, Ep, Mnz) observed as
663 inclusions and in the ductile matrix overprinting D₁ breccia in sample ACB35. The depletion of
664 LREE observed for Grt-Type1 is consistent with growth of Grt in apparent equilibrium with
665 accessory phases preferentially partitioning LREE, such as Aln. Indeed, Aln inclusions are (only)
666 observed in some of the analyzed garnets. Similarly, the enrichment of LREE observed in Grt-
667 Type2 is consistent with garnet growth at conditions where LREE-rich phases (e.g., Aln) are not
668 stable anymore and the only phase capable of incorporating LREEs is garnet. In fact, Ep-
669 rich/Aln-poor grains are observed in the paragenesis of the sheared breccia matrix, surrounding
670 Xtm/Thr aggregates, in turn resulting from the destabilization of first generation Aln or Mnz
671 (Fig. 6f; Janots et al., 2008; Hentschel et al., 2020). In summary, a first phase of Grt (Grt-Type1)
672 crystallization in apparent equilibrium with Aln is followed by a second phase of crystallization
673 of Grt (Grt-Type2) during which Aln was not stable anymore, replaced by Mnz during prograde
674 metamorphism (e.g. Janots et al., 2008, 2009; Spear, 2010). The exact *T* of transition from Aln-
675 bearing to Mnz-bearing paragenesis could shift from *T* ~ 350 °C to *T* ~ 550 °C depending on the
676 bulk CaO and REE content of the rock (Spear, 2010). A similar prograde crystallization
677 sequence has been reported from metapelites in the south-eastern Gotthard nappe described by
678 Janots et al. (2008, 2009). In that case, prograde destabilization of Aln close to peak conditions
679 of about 560-580 °C formed the Mnz and REE-poor Ep aggregates observed in the recrystallized
680 metapelite hosting the Grt (Janots et al., 2008). Mnz is rare in our samples, and it is likely that
681 Mnz destabilization during retrograde D₂ shearing at amphibolite-to-greenschist facies

682 conditions may have led to the formation of the Ep + Xtm/Thr aggregates observed in the
 683 recrystallized breccia matrix (e.g., Hentschel et al., 2020). Therefore, Ep/Aln microstructures in
 684 ACB35 Grt likely record a prograde-to-peak crystallization sequence (Fig. 9b). Interestingly, in
 685 both ACB35 and especially ACB18 samples, the compositional zoning of garnet suggests
 686 increasing P - T conditions from core to rim (Fig. 7a, SI Fig. S2b).

687 U-Pb dating of Grt results in scattered ages ranging from ~34 to ~20 Ma, which is
 688 broadly consistent with the ages for the regional peak metamorphism obtained from other case
 689 studies in the Gotthard nappe (22-19 Ma, Janots et al., 2009; Janots & Rubatto, 2014; Boston et
 690 al., 2017) and nearby Lepontine Dome (32-22 Ma, Rubatto et al., 2009). The peak metamorphic
 691 conditions are constrained by pseudosections calculated for different samples (ACB35, ACB25,
 692 ACB18) at 590 ± 15 °C and 0.9 ± 0.1 GPa. The obtained P - T conditions are consistent with
 693 recent estimates of Alpine peak metamorphic conditions from the southern Aar massif and
 694 Gotthard nappe (Berger et al., 2020; Janots et al., 2008, 2009; Nibourel et al., 2021; Wiederkehr
 695 et al., 2011), as well as the Penninic units of the Northern Lepontine dome (Boston et al., 2017;
 696 Galli et al., 2007). The 34-20 Ma age spread would describe a prolonged thermal peak in the
 697 Gotthard nappe lasting for ~10 Myrs (Fig. 9b). This conclusion is consistent with
 698 geochronological data supporting the occurrence of a prolonged thermal peak starting at ~32-34
 699 Ma in several other ECMs and Penninic units, lasting until 22-17 Ma when the main phase of
 700 exhumation occurred (Boston et al., 2017; Cenko-Tok et al., 2014; Egli et al., 2016; Girault et al.,
 701 2020; Janots et al., 2008, 2009; Rolland & Rossi, 2016; Rubatto et al., 2009; Sanchez et al.,
 702 2011).

703

704 5.1.3. Exhumation – D₂ shear zones

705 The reverse kinematics of D₂ shear zones and the occurrence of associated shallowly
 706 dipping tensional veins constrain a subhorizontal σ_1 , parallel to a NW-SE trending maximum
 707 shortening axis ϵ_1 , and perpendicular to a subvertical σ_3 (Fig. 9c). Based on the results of
 708 pseudosection calculation, these shear zones were already active at 520 ± 40 °C and 0.82 ± 0.12
 709 GPa. The conditions of re-equilibration of the analyzed samples (ACB27a $T > 500$ °C) are
 710 similar to the closure temperature for Rb-Sr in white mica inferred for similar case studies of
 711 granitoid shear zones ($T \leq 500$ -550 °C; e.g., Egli et al., 2015; Ribeiro et al., 2023). Therefore, it
 712 is very likely that the obtained Rb-Sr date of 18.1 ± 0.8 Ma (Fig. 8) reflects the (re-)
 713 crystallization of white mica in D₂ ductile shear zones. D₂ ductile shear zones accommodate the
 714 main phase of tectonic exhumation of the Gotthard nappe through reverse shearing on NW-
 715 steeply dipping planes. Rb-Sr dating of white mica indicates that the bulk foliation of RG₂
 716 developed during the same amphibolite-facies deformation event at 18.6 ± 1.9 Ma (sample
 717 ACB12b, Fig. 8e). However, biotite in D₂ shear zones (15.3 ± 0.9 Ma, sample ACB3b, SI Text
 718 S4, Fig. S4) provides a younger Rb-Sr age which indicates either a later deformation event or,
 719 more likely, reflects the lower closure temperature of the Rb-Sr isotope system in biotite (≤ 350 -
 720 400 °C; e.g., Jenkin et al., 2001) compared to white mica (≤ 500 °C). The exhumation of the ECMs
 721 in the Central and Western Alps have been accommodated by similar steeply-dipping, reverse
 722 shear zones developed during retrograde greenschist facies conditions between 22 and 17 Ma
 723 (Cenko-Tok et al., 2014; Goncalves et al., 2012; Herwegh et al., 2020; Rolland et al., 2008).

724

725 5.1.4. Strike-slip tectonics – D₃-D₄

726 The kinematics and geometrical relationships of D_{3A} and D_{3B} structures constrain their
 727 development under a transpressional strain field developed during NW-SE convergence (D_{3A}-
 728 D_{3B}), associated with NE-SW-directed extension (D_{3B} tensional veins and D_{3C} normal faults; Fig.
 729 9d). The kinematics of D₃ shear zones and tensional veins constrain a subhorizontal σ_1 and
 730 maximum shortening axis ϵ_1 oriented ~NW-SE and a sub-horizontal, NE-SW-oriented σ_3 (Fig.
 731 9d). Strike-slip D_{3A} shearing is constrained to develop at 395 ± 25 °C and 0.4 ± 0.1 GPa. At these
 732 temperature conditions, the Rb-Sr chronometer applied to white mica constrains the age of mica
 733 (re-)crystallization because the closure temperature of Sr diffusion in white mica is considerably
 734 higher (see previous section). Hence, the 14.7 ± 1.6 Ma age of white mica in D_{3A} sample
 735 ACB37b (Fig. 8) probably constrains the age of this deformation event. The occurrence of
 736 similar Rb-Sr ages for white mica (ACB37b, D_{3A}) and biotite (B19-1417, undeformed granite:
 737 15.5 ± 0.7 Ma; ACB3b and ACB14c, foliated granite: 15.3 ± 0.9 Ma and 15.0 ± 1.2 Ma,
 738 respectively; Table 1, Fig. 8, and SI Fig. S4), regardless of the intensity of sample deformation,
 739 suggests that the D_{3A} deformation event occurred at conditions broadly corresponding to the
 740 closure temperature of the Rb-Sr chronometer in biotite, that is $\sim \leq 350$ °C (e.g., Jenkins et al.,
 741 2001). If the temperatures were substantially higher (e.g., 400-500 °C), white mica would have
 742 recorded an older age due to its higher closure temperature for the Rb-Sr isotope system. In other
 743 words, the ~15 Ma age of biotite in the undeformed Rotondo granite represents a cooling age.
 744 The overlap of white mica and biotite Rb-Sr ages implies that ductile reactivation of D₂ under
 745 strike-slip conditions leading to D_{3A} shear zones occurred during a very short time period at ~15
 746 Ma. Further deformation during D₃ strike-slip tectonics was accommodated by brittle-ductile
 747 transpressional and extensional faults. The NW-SE-striking extensional veins associated to this
 748 brittle-ductile deformation event in the Lepontine dome and Aar-Gotthard area are consistently
 749 dated to <14 Ma (Bergemann et al., 2020). The contemporaneous (or cyclic) development of
 750 D_{3B}-D_{3C} extensional and transpressional structures is consistent with the regional tectonic setting
 751 during the activity of the Rhone-Simplon fault system (Campani et al., 2010), accommodating
 752 NE-SW extensional tectonics under a constant dominant NW-SE transpression.

753 Late D₄ zeolite- and gouge-bearing brittle faults reactivated the pre-existing, steeply
 754 dipping structural discontinuities under strike-slip conditions (Lützenkirchen & Loew, 2011).
 755 Their activity is constrained to have occurred between 12 and 3 Ma based on K-Ar illite dating
 756 (Kralik et al., 1992; Pleuger et al., 2012) at upper crustal levels ($T < 200$ °C, depth <7 km;
 757 Lützenkirchen & Loew, 2011). These chronological constraints are consistent with the prolonged
 758 Neogene activity of the Periadriatic-Simplon-Rhone fault system (Ricchi et al., 2019).

759 In conclusion, the brittle-ductile-brittle evolution inferred from the sequence of
 760 deformation structures in the Rotondo granite is the result of pre-Alpine tectonics overprinted by
 761 the peak-and-retrograde collisional Alpine tectonics. Pre-collisional structures apparently
 762 controlled the localization and accommodation of collisional strain in the crystalline unit.

763 5.1.5. Exhumation and cooling rates during Alpine collision

764 Rates of tectonic exhumation and cooling can be calculated considering the constraints on
 765 P , T , and age of deformation provided above (Fig. 9a). Rates are computed considering a
 766 geothermal gradient of 25 °C/km and a lithostatic pressure gradient of 27.5 MPa/km (e.g.,
 767 Nibourel et al., 2021). Exhumation from peak conditions at 590 °C and 0.9 GPa at 34 to 20 Ma
 768 (U-Pb of garnet) to 520 °C and 0.8 GPa (D₂ conditions) at 18 Ma (Rb-Sr in white mica) occurred

769 at a rate of 0.22 to 1.8 mm/yr (km/Myr), associated with a cooling rate ranging between 5 to 35
 770 °C/Myr, respectively for the oldest and youngest U-Pb ages. Most of the exhumation was
 771 accommodated through the activity of D₂ ductile reverse shear zones. They accommodated the
 772 exhumation from D₂ conditions (520 °C and 0.8 GPa) at 18 Ma (Rb-Sr on white mica) to D₃
 773 conditions (395 °C and 0.4 GPa) at ~14 Ma (Rb-Sr on white mica and biotite). Related
 774 exhumation rates range between 3.8 and 5.1 mm/yr, with an associated cooling rate of 30-40
 775 °C/Myr. On average, the exhumation from peak metamorphic conditions at 34-20 Ma to the
 776 brittle-ductile conditions recorded after D_{3A} deformation at 14 Ma occurred at an average
 777 exhumation rate of 0.9-3.0 mm/yr, associated with a cooling rate of 10-30 °C/Myr. Such
 778 exhumation rates are comparable to those retrieved from regional thermochronometry (~1-3
 779 mm/yr; Glotzback et al., 2010; Herwegh et al., 2020; Nibourel et al., 2021). Similarly, the high
 780 cooling rates recorded during D₂-D₃ exhumation are compatible with the estimates of 30-40
 781 °C/Myr provided by Janots et al. (2009) for the eastern Gotthard nappe.

782 After the exhumation through the brittle-ductile transition, and the switch to regional
 783 transpression, the exhumation became much slower, as constrained by comparing D₃ Rb-Sr
 784 white mica/biotite ages and the youngest K-Ar illite age (3 Ma) Kralik et al. (1992) and Pleuger
 785 et al. (2012) for gouge-bearing faults similar to D₄ structures. The obtained exhumation rate of
 786 ~0.6 mm/yr is associated with a cooling rate of ~15 °C/Myr (Fig. 9a), similarly to what
 787 previously reported from thermochronological constraints (Glotzback et al., 2010; Herwegh et
 788 al., 2020).

789

790 5.2. Rheological evolution of the Rotondo granite during Alpine collision

791 In the RG, collisional shortening is accommodated through the reactivation and shearing
 792 of pre-collisional D₁ structures and pre-existing compositional and structural heterogeneities at
 793 different scales. In the current orientation D₁ brittle structures are severely misoriented, forming
 794 high angles to the maximum principal stress expected during NW-directed Alpine convergence
 795 and collision (Rosenberg et al., 2021). Despite this fact, these structures influenced the rheology
 796 and localized strain throughout the whole D₂-D₄ evolution across different *P-T* and rheological
 797 conditions of the crystalline basement (Fig. 9c-d). In the following sections, we constrain the
 798 rheology, as well as the stress and fluid regimes at which D₁ to D₄ structures likely formed.

799 The current high-angle dip of the D₁ brittle structures would be more compatible with an
 800 extensional or strike-slip tectonic regime than with a compressional/convergent setting. Given
 801 the uncertainty regarding the tectonic regime and original orientation of D₁ structures, we can
 802 only speculate about the values of differential stress ($\Delta\sigma$) and pore fluid pressure (P_f) during D₁
 803 development. The occurrence of thin shear fractures and cataclasites may indicate a dynamic
 804 environment characterized by variable $\Delta\sigma$ ($> 4 \cdot T_s - 5.6 \cdot T_s$, with T_s : tensile strength) and low P_f .
 805 Furthermore, the mutual overprinting between breccias and (fault-)veins implies cyclical
 806 variation of P_f and permeability in the brittle regime. Fluid-assisted brecciation is related to
 807 transient fluid-pressure increase in low-permeability rocks and facilitated in extensional regimes,
 808 as well as along pre-existing structures (Jébrak, 1997; Sibson et al., 1988). Fault-veins (lenticular
 809 Qz-veins parallel to the shear plane) suggest the fluid-driven reactivation of a pre-existing
 810 structure, at low $\Delta\sigma$ and likely sublithostatic P_f (probably < 300 MPa in the brittle field; Sibson
 811 et al., 1988). Similar conclusions can be drawn from the geometry of breccias, locally resembling
 812 crackle and mosaic breccias with randomly distributed fractures (Fig. 3c-d). These geometries

813 indicate very low $\Delta\sigma$ ($< 4 \cdot Ts$), and effective σ_1 close to zero ($\Delta\sigma \sim Ts$; Woodcock et al., 2007),
 814 and they are in some instances interpreted as resulting from seismic activity (Sibson, 1985, 1987;
 815 Melosh et al., 2014). Nonetheless, we cannot exclude that at least part of the veining occurred
 816 during prograde (brittle) reactivation of D_1 misoriented faults under compression, defining a
 817 general fault-valve behavior (Sibson et al., 1988). Such activity, if present, was only limited to
 818 pre-peak and brittle conditions, given the lack of brittle-over-ductile overprint in D_1 structures.

819 During D_2 - D_3 retrograde shearing at amphibolite-to-upper greenschist facies conditions
 820 ($T = 400$ - 520 °C, $P = 0.4$ - 0.8 GPa), the granite was characterized by a network of high strain
 821 shear zones, localized on magmatic (aplitic, mafic dykes) and tectonic (D_1) precursors,
 822 delimiting low strain domains of relatively undeformed granite. D_2 shear zones are oriented at
 823 high angle (70 - 80°) to the principal stress σ_1 (Fig. 9d-e). Accordingly, shearing on D_2 planes
 824 developed even if the resolved shear stress was very small, thus suggesting a limited shear
 825 strength of such D_2 ductile shear zones. Shear zone strength was controlled by reaction-
 826 weakening processes related to plagioclase destabilization, which led to the activation of fluid-
 827 mediated grain-size sensitive deformation mechanisms, as observed in similar granitoid ductile
 828 shear zones (Ceccato et al., 2022; Oliot et al., 2014). This localized weakening might have been
 829 related to the higher fluid content of D_1 structures exploited by D_2 compared to the host rock.
 830 This higher fluid content is likely related to either a fluid-bearing mineral paragenesis of former
 831 D_1 structures, or to the increased permeability of the granite along D_1 structures promoting fluid
 832 flux during retrograde D_2 shearing (e.g., Oliot et al., 2010). Further analyses would be necessary
 833 to discern between the two options and to understand the origin of the fluids and weakening. In
 834 any case, ductile shear zones acted as fluid pathways during D_2 deformation as can be inferred
 835 from the occurrence of sheared Qz + Cal veins (Fig. 4a), including Cal porphyroclasts (Fig. 11 of
 836 Rast et al., 2022). Cal porphyroclasts in Qz-mylonites have been constrained to develop during
 837 ductile shearing at low $\Delta\sigma$ (< 10 MPa) at amphibolite facies, fluid-rich conditions (Mancktelow
 838 & Pennacchioni, 2010). This further suggest that the D_2 ductile shear zones were extremely weak
 839 and able to accommodate strain at very low shear stresses, probably on the order of few (1-4)
 840 MPa, considering a $\Delta\sigma$ of 10 MPa) and an orientation of 80° with respect to σ_1 (Fig. 9c).
 841 Accordingly, the pervasive occurrence of tensional veins in the undeformed granite indicates
 842 high (quasi-supralithostatic) P_f and limited $\Delta\sigma$ ($< 4 \cdot Ts$, in the range 36 to 60 MPa for granite,
 843 Cox, 2010; Etheridge, 1983; Sibson, 2003; Sibson et al., 1988). Therefore, during D_2 - D_3 ductile
 844 shearing: (i) there is a difference in the maximum $\Delta\sigma$ of ~ 25 - 50 MPa between weak shear zones
 845 (< 10 MPa) and in the low-strain granite (< 60 MPa); (ii) the strength of both high-strain shear
 846 zone and low strain granite domains is limited by tensional veining related to fluid overpressure,
 847 which in turn implies (iii) low permeability in the low strain granite during ductile deformation.
 848 D_2 ductile shear zones might have acted as higher-permeability fluid conduits, but overall the
 849 permeability was not high enough to allow the dissipation of P_f build-up to supralithostatic
 850 conditions.

851 During further cooling and exhumation ($T < 350$ °C, $P = 0.2$ - 0.4 GPa), pre-existent
 852 misoriented structures failed to be reactivated (Fig. 9d). The development of new conjugate
 853 faults (D_{3B}) suggests increasing $\Delta\sigma$ ($> 5.6 \cdot Ts$) and decreasing P_f (probably close to hydrostatic
 854 conditions) during strike-slip deformation across the brittle-ductile transition. The decreased P_f
 855 was also related to the increased porosity and permeability of the granite during this deformation
 856 stage. High permeability of such deformation structures is documented by the pervasive
 857 occurrence of mineralized open veins along fault shear planes (Fig. 5a), as well as by the

858 occurrence of high-porosity hydrothermal alteration and the development of episyenites
859 (Pennacchioni et al., 2016).

860 At shallow crustal levels ($T < 200$ °C, $P < 0.2$ GPa), D₄ zeolite- and gouge-bearing faults
861 reactivated the rock fabrics and pre-existent structural heterogeneities instead of developing new
862 fractures and fault zones (Fig. 9d). Fluids leading to the crystallization of zeolites percolated
863 through the highly permeable network of pre-existing fractures and structural heterogeneities.
864 Similar zeolite-bearing fractures and faults are reported from the granitoid plutons of the Central
865 and Eastern Alps (e.g., Adamello: Pennacchioni et al., 2006; Rieserferner: Ceccato &
866 Pennacchioni, 2018), as well as from all the crystalline massifs of the Central Alps (e.g.,
867 Weisenberger and Bucher, 2010). For instance, in the Adamello, similarly to the Rotondo, zeolite
868 veins and gouges are observed to intrude the pre-existent fracture and fault network, locally
869 reactivating fault planes (Pennacchioni et al., 2006). The observed complex kinematics of
870 reactivation and the fluid-overpressure inferred from the occurrence of zeolite-bearing veins and
871 gouges were interpreted to be the result of earthquake swarm activity at shallow crustal levels
872 (Dempsey et al., 2014). In that case, zeolite-bearing gouges were developed during transient
873 high-stress or high pore-fluid pressure events. In the RG, low P_f of 10-30 MPa were estimated
874 from the stability of fault zeolite paragenesis (Lützenkirchen & Loew, 2011). In addition,
875 shearing planes in the granite are highly misoriented with respect to the NW-SE Alpine
876 shortening direction. Thus, transient high differential stress would have promoted the
877 development of new conjugate shear fractures, rather than reactivating misoriented planes.
878 Nonetheless, D₄ structures localize on D₁-D₂-D₃ structures (Lützenkirchen & Loew, 2011),
879 which are characterized by phyllosilicate-bearing fabrics that affect the frictional and cohesion
880 properties of the shearing planes at brittle conditions (Bistacchi et al., 2012; Volpe et al., 2022;
881 Pozzi et al., 2022). In addition, the low frictional properties of the fault gouges developed during
882 shearing might have further promoted the localization of brittle faulting on highly misoriented,
883 and otherwise frictionally-locked, fault planes during the latest stages of Alpine brittle
884 deformation (Bistacchi et al., 2012; Collettini et al., 2019; Volpe et al., 2023).

885

886 6. Conclusions

887 The P - T - t - d evolution of the Rotondo granite is recorded by a brittle-ductile-brittle
888 structural evolution. D₁ breccias and cataclasites develop in the Rotondo granite before the
889 attainment of the Alpine peak metamorphic conditions, the latter occurring between 34 and 20
890 Ma and recorded by U-Pb in garnet. Peak metamorphic conditions are closer to the amphibolite
891 facies ($T > 550$ °C, $P > 0.7$ GPa) than those previously proposed for the ECMs and the Gotthard
892 nappe ($T < 450$ - 500 °C, $P < 0.5$ - 0.6 GPa; Todd and Engi, 1997). Retrograde exhumation was
893 then controlled by reverse ductile shearing on D₂ ductile shear zones, localized on pre-existent
894 structural and compositional heterogeneities. The very limited shear strength of D₂ ductile shear
895 zones allowed it to accommodate fast exhumation of the Gotthard nappe at 1-3 km/Myr between
896 20 and 14 Ma. Further exhumation was accommodated at slower rates by D₃ greenschist facies
897 ($T < 400$ °C, $P < 0.4$ GPa) ductile and brittle-ductile shear zones, developed as a local response to
898 the regional strike-slip activity of the Simplon-Rhone fault system.

899 Based on the common structural and tectonometamorphic history of the Rotondo granite
900 and the other ECMs in the Central and Western Alps, we can extrapolate the results obtained

901 from the Rotondo to infer fundamental implications for the rheology of the European continental
902 crust during Alpine collision:

- 903 • The European continental crust, now exposed in the ECMs, was extremely weak
904 during Alpine continental collision and deformation at amphibolite-to-greenschist
905 facies.
- 906 • The occurrence of inherited tectonic and primary (e.g., magmatic) fabrics and
907 structures, although highly misoriented, clearly controlled strain geometry and
908 localization throughout their entire rheological and metamorphic evolution.
- 909 • The main weakening event occurred during retrograde conditions.

910 The weakness of the European continental crust during Alpine collision allowed it to
911 focus and localize collisional strain in the external domains of the orogen, promoting the
912 localized and fast exhumation of the crystalline massifs ahead of the advancing dry and strong
913 Adriatic lower crust. At the scale of the orogen, collisional shortening was therefore
914 accommodated through the localized, and fast exhumation of the External Crystalline Massifs,
915 by means of the activity of weak ductile shear zones, localized on pre-existing tectonic and
916 primary fabrics.

917

918 **Acknowledgments**

919 This paper is FEAR Publication #19. This research is supported by ETH Zurich research
920 funds to WMB and the European Research Council (ERC) Synergy project “Fault Activation and
921 Earthquake Rupture” (FEAR) (grant 856559) granted to Domenico Giardini, Stefan Wiemer,
922 Massimo Cocco, and Florian Amman. Markus Rast is warmly thanked for the introduction to the
923 Bedretto tunnel geology and for providing the sample B19-1417 and thin sections adopted for
924 Rb-Sr analysis of biotite. Neil Mancktelow and Bernardo Cesare are thanked for fruitful
925 discussions about regional geology and garnet petrography. The authors acknowledge Luiz G.
926 Morales and ScopeM for their support and assistance during SEM data acquisition and
927 processing. Julien Allaz is thanked for EPMA data acquisition and technical assistance. Remy
928 Lüchinger and Lydia Zender are gratefully acknowledged for their support during thin section
929 preparation and XRF analyses, respectively. The crew of the Capanna Piansecco and SAC-CAS
930 Bellinzona & Valli are warmly thanked for their logistic support, and their friendly and
931 unconditional hospitality during fieldwork in the Rotondo area. The authors acknowledge the
932 logistic support from the Bedretto Lab team.

933

934 **Open Research**

935 Chemical and geochronological data supporting the conclusions of the present study are
936 reported in the main text and in the Supplementary Information files. The dataset is also
937 available at ETH Zurich Research Collection via <https://doi.org/10.3929/ethz-b-000644819> with
938 Creative Commons Attribution 4.0 International license (Ceccato et al., 2023).

939

940

941 **References**

- 942 Aysal, N. et al., 2023, A New Natural Secondary Reference Material for Garnet U-Pb
943 Dating by TIMS and LA-ICP-MS. *Geostandards and Geoanalytical Research*, p. ggr.12493,
944 doi:10.1111/ggr.12493.
- 945 Ballèvre, M., Manzotti, P., & Dal Piaz, G. V. (2018). Pre-Alpine (Variscan) inheritance:
946 a key for the location of the future Valaisan basin (Western Alps). *Tectonics*, 37(3), 786–817.
947 <https://doi.org/10.1002/2017tc004633>
- 948 Behr, W. M., & Platt, J. P. (2014). Brittle faults are weak, yet the ductile middle crust is
949 strong: Implications for lithospheric mechanics. *Geophysical Research Letters*, 41(22), 8067-
950 8075. <https://doi.org/10.1002/2014GL061349>
- 951 Behr, W. M., & Platt, J. P. (2013). Rheological evolution of a Mediterranean subduction
952 complex. *Journal of Structural Geology*, 54, 136-155. <https://doi.org/10.1016/j.jsg.2013.07.012>
- 953 Bellahsen, N., Mouthereau, F., Boutoux, A., Bellanger, M., Lacombe, O., Jolivet, L., &
954 Rolland, Y. (2014). Collision kinematics in the western external Alps. *Tectonics*, 33(6), 1055–
955 1088. <https://doi.org/10.1002/2013TC003453>
- 956 Bellanger, M., Bellahsen, N., Jolivet, L., Baudin, T., Augier, R., & Boutoux, A. (2014).
957 Basement shear zones development and shortening kinematics in the Ecrins Massif, Western
958 Alps. *Tectonics*, 33(2), 84–111. <https://doi.org/10.1002/2013TC003294>
- 959 Beltrando, M., Frasca, G., Compagnoni, R., & Vitale-Brovarone, A. (2012). The Valaisan
960 controversy revisited: Multi-stage folding of a Mesozoic hyper-extended margin in the Petit St.
961 Bernard pass area (Western Alps). *Tectonophysics*, 579, 17–36.
962 <https://doi.org/10.1016/J.TECTO.2012.02.010>
- 963 Beltrando, M., Manatschal, G., Mohn, G., Dal Piaz, G. V., Vitale Brovarone, A., &
964 Masini, E. (2014). Recognizing remnants of magma-poor rifted margins in high-pressure
965 orogenic belts: The Alpine case study. *Earth-Science Reviews*, 131, 88–115.
966 <https://doi.org/10.1016/J.EARSCIREV.2014.01.001>
- 967 Bergemann, C., Gnos, E., Berger, A., Janots, E., & Whitehouse, M. J. (2020). Dating
968 tectonic activity in the Lepontine Dome and Rhone-Simplon Fault regions through hydrothermal
969 monazite-(Ce). *Solid Earth*, 11(1), 199–222. <https://doi.org/10.5194/se-11-199-2020>
- 970 Berger, A., Mercolli, I. P., Herwegh, M., & Gnos, E. (2017). Explanatory Notes to the
971 Geological map of the Aar massif, Tavetsch and Gotthard nappes, Geological special map No.
972 129. Wabern: Federal Office of Topography swisstopo.
- 973 Berger, A., Engi, M., Erne-Schmid, S., Glotzbach, C., Spiegel, C., de Goede, R., &
974 Herwegh, M. (2020). The relation between peak metamorphic temperatures and subsequent
975 cooling during continent–continent collision (western Central Alps, Switzerland). *Swiss Journal*
976 *of Geosciences*, 113(1), 1–18. <https://doi.org/10.1186/S00015-020-00356-4>
- 977 Bertini, G., Marcucci, M., Nevini, R., Passerini, P., & Sguazzoni, G. (1985). Patterns of
978 faulting in the Mont Blanc granite. *Tectonophysics*, 111(1–2), 65–106.
979 [https://doi.org/10.1016/0040-1951\(85\)90066-6](https://doi.org/10.1016/0040-1951(85)90066-6)

- 980 Bistacchi, A., Massironi, M., Menegon, L., Bolognesi, F., & Donghi, V. (2012). On the
981 nucleation of non-Andersonian faults along phyllosilicate-rich mylonite belts. *Geological*
982 *Society, London, Special Publications*, 367(1), 185-199. <https://doi.org/10.1144/SP367.13>
- 983 Boston, K. R., Rubatto, D., Hermann, J., Engi, M., & Amelin, Y. (2017). Geochronology
984 of accessory allanite and monazite in the Barrovian metamorphic sequence of the Central Alps,
985 Switzerland. *Lithos*, 286–287, 502–518. <https://doi.org/10.1016/J.LITHOS.2017.06.025>
- 986 Bühler, M., Zurbriggen, R., Berger, A., Herwegh, M., & Rubatto, D. (2022). Late
987 Carboniferous Schlingen in the Gotthard nappe (Central Alps) and their relation to the Variscan
988 evolution. *International Journal of Earth Sciences*, 1–26. [https://doi.org/10.1007/S00531-022-](https://doi.org/10.1007/S00531-022-02247-5)
989 [02247-5](https://doi.org/10.1007/S00531-022-02247-5)
- 990 Bürgmann, R., & Dresen, G. (2008). Rheology of the lower crust and upper mantle:
991 Evidence from rock mechanics, geodesy, and field observations. *Annu. Rev. Earth Planet. Sci.*,
992 36, 531-567. <https://doi.org/10.1146/annurev.earth.36.031207.124326>
- 993 Bussien, D., Bussy, F., Masson, H., Magna, T., & Rodionov, N. (2008). Variscan
994 lamprophyres in the Lower Penninic domain (Central Alps): Age and tectonic significance.
995 *Bulletin de La Societe Geologique de France*, 179(4), 369–381.
996 <https://doi.org/10.2113/gssgfbull.179.4.369>
- 997 Campani, M., Mancktelow, N., Seward, D., Rolland, Y., Müller, W., & Guerra, I. (2010).
998 Geochronological evidence for continuous exhumation through the ductile-brittle transition
999 along a crustal-scale low-angle normal fault: Simplon Fault Zone, central Alps. *Tectonics*, 29(3).
1000 <https://doi.org/10.1029/2009TC002582>
- 1001 Candioti, L. G., Duretz, T., Moulas, E., & Schmalholz, S. M. (2021). Buoyancy versus
1002 shear forces in building orogenic wedges. *Solid Earth*, 12(8), 1749–1775.
1003 <https://doi.org/10.5194/se-12-1749-2021>
- 1004 Ceccato, A., & Pennacchioni, G. (2018). Structural evolution of the Rieserferner pluton
1005 in the framework of the Oligo-Miocene tectonics of the Eastern Alps. *Journal of Structural*
1006 *Geology*, 116, 64-80. <https://doi.org/10.1016/j.jsg.2018.08.004>
- 1007 Ceccato, A., Menegon, L., Warren, C. J., & Halton, A. M. (2020). Structural and
1008 metamorphic inheritance controls strain partitioning during orogenic shortening (Kalak Nappe
1009 Complex, Norwegian Caledonides). *Journal of Structural Geology*, 136, 104057.
1010 <https://doi.org/10.1016/j.jsg.2020.104057>
- 1011 Ceccato, A., Goncalves, P., & Menegon, L. (2022). On the petrology and microstructures
1012 of small-scale ductile shear zones in granitoid rocks: An overview. *Journal of Structural*
1013 *Geology*, 161(June), 104667. <https://doi.org/10.1016/j.jsg.2022.104667>
- 1014 Ceccato, A., Behr, W. M., Zappone, A. S., Tavazzani, L., Giuliani, A., (2023). Datasets
1015 for "Structural evolution, exhumation rates, and rheology of the European crust during Alpine
1016 collision: constraints from the Rotondo granite – Gotthard nappe". *ETH Zurich Research*
1017 *Collection*. DOI 10.3929/ethz-b-000644819
- 1018 Cesare, B., Nestola, F., Johnson, T., Mugnaioli, E., Della Ventura, G., Peruzzo, L.,
1019 Bartoli, O., Viti, C. & Erickson, T. (2019). Garnet, the archetypal cubic mineral, grows
1020 tetragonal. *Scientific Reports*, 9(1), 14672. <https://doi.org/10.1038/s41598-019-51214-9>

- 1021 Célini, N., Mouthereau, F., Lahfid, A., Gout, C., & Callot, J. P. (2023). Rift thermal
1022 inheritance in the SW Alps (France): insights from RSCM thermometry and 1D thermal
1023 numerical modelling. *Solid Earth*, 14(1), 1–16. <https://doi.org/10.5194/SE-14-1-2023>
- 1024 Cenki-Tok, B., Darling, J. R., Rolland, Y., Dhuime, B., & Storey, C. D. (2014). Direct
1025 dating of mid-crustal shear zones with synkinematic allanite: new in situ U-Th-Pb
1026 geochronological approaches applied to the Mont Blanc massif. *Terra Nova*, 26(1), 29–37.
1027 <https://doi.org/10.1111/TER.12066>
- 1028 Challandes, N., Marquer, D., & Villa, I. M. (2008). P-T-t modelling, fluid circulation,
1029 and ^{39}Ar - ^{40}Ar and Rb-Sr mica ages in the Aar Massif shear zones (Swiss Alps). *Swiss Journal*
1030 *of Geosciences*, 101(2), 269–288. <https://doi.org/10.1007/s00015-008-1260-6>
- 1031 Collettini, C., Tesei, T., Scuderi, M. M., Carpenter, B. M., & Viti, C. (2019). Beyond
1032 Byerlee friction, weak faults and implications for slip behavior. *Earth and Planetary Science*
1033 *Letters*, 519, 245–263. <https://doi.org/10.1016/j.epsl.2019.05.011>
- 1034 Connolly, J. A. D. (2005). Computation of phase equilibria by linear programming: A
1035 tool for geodynamic modeling and its application to subduction zone decarbonation. *Earth and*
1036 *Planetary Science Letters*, 236(1–2), 524–541. <https://doi.org/10.1016/J.EPSL.2005.04.033>
- 1037 Cook, K. L., & Royden, L. H. (2008). The role of crustal strength variations in shaping
1038 orogenic plateaus, with application to Tibet. *Journal of Geophysical Research: Solid Earth*,
1039 113(B8). <https://doi.org/10.1029/2007JB005457>
- 1040 Cox, S. F. (2010). The application of failure mode diagrams for exploring the roles of
1041 fluid pressure and stress states in controlling styles of fracture-controlled permeability
1042 enhancement in faults and shear zones. *Geofluids*, 10(1–2), 217–233.
1043 <https://doi.org/10.1111/j.1468-8123.2010.00281.x>
- 1044 Dal Piaz, G. V., Bistacchi, A., & Massironi, M. (2003). Geological outline of the Alps.
1045 *Episodes*, 26(3), 175–180. <https://doi.org/https://doi.org/10.18814/epiugs/2003/v26i3/004>
- 1046 Dall’Asta, N., Hoareau, G., Manatschal, G., Centrella, S., Denèle, Y., Ribes, C., & Kalifi,
1047 A. (2022). Structural and petrological characteristics of a Jurassic detachment fault from the
1048 Mont-Blanc massif (Col du Bonhomme area, France). *Journal of Structural Geology*,
1049 159(March). <https://doi.org/10.1016/j.jsg.2022.104593>
- 1050 Deng, X.-D., Li, J.-W., Luo, T., and Wang, H.-Q., 2017, Dating magmatic and
1051 hydrothermal processes using andradite-rich garnet U–Pb geochronometry. *Contributions to*
1052 *Mineralogy and Petrology*, v. 172, p. 71, doi:10.1007/s00410-017-1389-2.
- 1053 Egli, D., Müller, W., & Mancktelow, N. (2016). Laser-cut Rb–Sr microsampling dating
1054 of deformational events in the Mont Blanc-Aiguilles Rouges region (European Alps). *Terra*
1055 *nova*, 28(1), 35–42. <https://doi.org/10.1111/ter.12184>
- 1056 Egli, D., Mancktelow, N., & Spikings, R. (2017). Constraints from $^{40}\text{Ar}/^{39}\text{Ar}$
1057 geochronology on the timing of Alpine shear zones in the Mont Blanc-Aiguilles Rouges region
1058 of the European Alps. *Tectonics*, 36(4), 730–748. <https://doi.org/10.1002/2016TC004450>
- 1059 Etheridge, M. A. (1983). Differential stress magnitudes during regional deformation and
1060 metamorphism: Upper bound imposed by tensile fracturing. *Geology*, 11(4), 231–234.
1061 [https://doi.org/10.1130/0091-7613\(1984\)12](https://doi.org/10.1130/0091-7613(1984)12)

- 1062 Fitzpayne, A., Giuliani, A., Hergt, J., Woodhead, J. D., & Maas, R. (2020). Isotopic
1063 analyses of clinopyroxenes demonstrate the effects of kimberlite melt metasomatism upon the
1064 lithospheric mantle. *Lithos*, 370, 105595. <https://doi.org/10.1016/j.lithos.2020.105595>
- 1065 Galli, A., Mancktelow, N., Reusser, E., & Caddick, M. (2007). Structural geology and
1066 petrography of the Naret region (northern Valle Maggia, N.Ticino, Switzerland). *Swiss Journal*
1067 *of Geosciences*, 100(1), 53–70. <https://doi.org/10.1007/s00015-007-1211-7>
- 1068 Gapais, D., Bale, P., Choukroune, P., Cobbold, P. R., Mahjoub, Y., & Marquer, D.
1069 (1987). Bulk kinematics from shear zone patterns: some field examples. *Journal of Structural*
1070 *Geology*, 9(5–6), 635–646. [https://doi.org/10.1016/0191-8141\(87\)90148-9](https://doi.org/10.1016/0191-8141(87)90148-9)
- 1071 Girault, J. B., Bellahsen, N., Boutoux, A., Rosenberg, C. L., Nanni, U., Verlaguet, A., &
1072 Beyssac, O. (2020). The 3-D Thermal Structure of the Helvetic Nappes of the European Alps:
1073 Implications for Collisional Processes. *Tectonics*, 39(3), e2018TC005334.
1074 <https://doi.org/10.1029/2018TC005334>
- 1075 Giuliani, A., Oesch, S., Guillong, M., Howarth G.H. Mica Rb-Sr dating by laser ablation
1076 ICP-MS/MS using an isochronous calibration material and application to West African
1077 kimberlites. Submitted to *Chemical Geology*.
- 1078 Glotzbach, C., Reinecker, J., Danišík, M., Rahn, M., Frisch, W., & Spiegel, C. (2010).
1079 Thermal history of the central Gotthard and Aar massifs, European Alps: Evidence for steady
1080 state, long-term exhumation. *Journal of Geophysical Research: Earth Surface*, 115(F3).
1081 <https://doi.org/10.1029/2009JF001304>
- 1082 Goncalves, P., Oliot, E., Marquer, D., & Connolly, J. A. D. (2012). Role of chemical
1083 processes on shear zone formation: An example from the grimsel metagranodiorite (Aar massif,
1084 Central Alps). *Journal of Metamorphic Geology*, 30(7), 703–722. <https://doi.org/10.1111/j.1525-1314.2012.00991.x>
- 1086 Goncalves, P., Poilvet, J. C., Oliot, E., Trap, P., & Marquer, D. (2016). How does shear
1087 zone nucleate? An example from the Suretta nappe (Swiss Eastern Alps). *Journal of Structural*
1088 *Geology*, 86, 166–180. <https://doi.org/10.1016/j.jsg.2016.02.015>
- 1089 Green, E., Holland, T., & Powell, R. (2007). An order-disorder model for omphacitic
1090 pyroxenes in the system jadeite-diopside-hedenbergite-acmite, with applications to eclogitic
1091 rocks. *American Mineralogist*, 92(7), 1181–1189. <https://doi.org/10.2138/AM.2007.2401>
- 1092 Groome, W. G., Koons, P. O., & Johnson, S. E. (2008). Metamorphism, transient mid-
1093 crustal rheology, strain localization and the exhumation of high-grade metamorphic rocks.
1094 *Tectonics*, 27(1). <https://doi.org/10.1029/2006TC001992>
- 1095 Guermani, A., & Pennacchioni, G. (1998). Brittle precursors of plastic deformation in a
1096 granite: An example from the Mont Blanc massif (Helvetic, western Alps). *Journal of Structural*
1097 *Geology*, 20(2–3), 135–148. [https://doi.org/10.1016/S0191-8141\(97\)00080-1](https://doi.org/10.1016/S0191-8141(97)00080-1)
- 1098 Guillong, M., Hametner, K., Reusser, E., Wilson, S. A., & Günther, D. (2005).
1099 Preliminary characterisation of new glass reference materials (GSA-1G, GSC-1G, GSD-1G and
1100 GSE-1G) by laser ablation-inductively coupled plasma-mass spectrometry using 193 nm, 213 nm
1101 and 266 nm wavelengths. *Geostandards and Geoanalytical Research*, 29(3), 315–331.
1102 <https://doi.org/10.1111/j.1751-908X.2005.tb00903.x>

- 1103 Guillong, M., von Quadt, A., Sakata, S., Peytcheva, I., & Bachmann, O. (2014). LA-ICP-
1104 MS Pb–U dating of young zircons from the Kos–Nisyros volcanic centre, SE Aegean arc. *J.*
1105 *Anal. At. Spectrom.*, 29(6), 963–970. <https://doi.org/10.1039/C4JA00009A>
- 1106 Hafner, S. (1958). Petrographie des südwestlichen Gotthardmassives (zwischen St.
1107 Gotthardpass und Nufenenpass). *Schweizerische Mineralogische und Petrographische*
1108 *Mitteilungen* (Vol. 38). <https://doi.org/10.3929/ethz-a-000097546>
- 1109 Handy, M. R., M. Schmid, S., Bousquet, R., Kissling, E., & Bernoulli, D. (2010).
1110 Reconciling plate-tectonic reconstructions of Alpine Tethys with the geological-geophysical
1111 record of spreading and subduction in the Alps. *Earth-Science Reviews*, 102(3–4), 121–158.
1112 <https://doi.org/10.1016/j.earscirev.2010.06.002>
- 1113 Hentschel, F., Janots, E., Trepmann, C. A., Magnin, V., & Lanari, P. (2020). Corona
1114 formation around monazite and xenotime during greenschist-facies metamorphism and
1115 deformation. *European Journal of Mineralogy*, 32(5), 521-544. [https://doi.org/10.5194/ejm-32-](https://doi.org/10.5194/ejm-32-521-2020)
1116 [521-2020](https://doi.org/10.5194/ejm-32-521-2020)
- 1117 Herwegh, M., Berger, A., Baumberger, R., Wehrens, P., & Kissling, E. (2017). Large-
1118 Scale Crustal-Block-Extrusion During Late Alpine Collision. *Scientific Reports*, 7(1), 1–10.
1119 <https://doi.org/10.1038/s41598-017-00440-0>
- 1120 Herwegh, M., Berger, A., Glotzbach, C., Wangenheim, C., Mock, S., Wehrens, P., et al.
1121 (2020). Late stages of continent-continent collision: Timing, kinematic evolution, and
1122 exhumation of the Northern rim (Aar Massif) of the Alps. *Earth-Science Reviews*, 200, 102959.
1123 <https://doi.org/10.1016/J.EARSCIREV.2019.102959>
- 1124 Hogmalm K. J., Zack T., Karlsson A. K. O., Sjöqvist A. S. L. and Garbe-Schönberg D.
1125 (2017) In situ Rb–Sr and K–Ca dating by LA-ICP-MS/MS: an evaluation of N₂O and SF₆ as
1126 reaction gases. *Journal of Analytical Atomic Spectrometry* 32, 305-313.
1127 DOI:10.1039/C6JA00362A
- 1128 Holland, T. J. B., & Powell, R. (1998). An internally consistent thermodynamic data set
1129 for phases of petrological interest. *Journal of Metamorphic Geology*, 16(3), 309–343.
1130 <https://doi.org/10.1111/J.1525-1314.1998.00140.X>
- 1131 Holland, T. J. B., & Powell, R. (2011). An improved and extended internally consistent
1132 thermodynamic dataset for phases of petrological interest, involving a new equation of state for
1133 solids. *Journal of Metamorphic Geology*, 29(3), 333–383. [https://doi.org/10.1111/J.1525-](https://doi.org/10.1111/J.1525-1314.2010.00923.X)
1134 [1314.2010.00923.X](https://doi.org/10.1111/J.1525-1314.2010.00923.X)
- 1135 Horstwood, M.S.A., Košler, J., Gehrels, G., Jackson, S.E., McLean, N.M., Paton, C.,
1136 Pearson, N.J., Sircombe, K., Sylvester, P., Vermeesch, P., Bowring, J.F., Condon, D.J., Schoene,
1137 B., 2016. Community-Derived Standards for LA - ICP - MS U-(Th-)Pb Geochronology –
1138 Uncertainty Propagation, Age Interpretation and Data Reporting. *Geostand Geoanal Res* 40,
1139 311–332. <https://doi.org/10.1111/j.1751-908X.2016.00379.x>
- 1140 Jamtveit, B., Petley-Ragan, A., Incel, S., Dunkel, K. G., Aupart, C., Austrheim, H.,
1141 Corfu, F., Menegon, L. & Renard, F. (2019). The effects of earthquakes and fluids on the
1142 metamorphism of the lower continental crust. *Journal of Geophysical Research: Solid Earth*,
1143 124(8), 7725-7755. <https://doi.org/10.1029/2018JB016461>

- 1144 Janots, E., & Rubatto, D. (2014). U-Th-Pb dating of collision in the external Alpine
1145 domains (Urseren zone, Switzerland) using low temperature allanite and monazite. *Lithos*, 184–
1146 187, 155–166. <https://doi.org/10.1016/j.lithos.2013.10.036>
- 1147 Janots, E., Engi, M., Berger, A., Allaz, J., Schwarz, J. O., & Spandler, C. (2008).
1148 Prograde metamorphic sequence of REE minerals in pelitic rocks of the Central Alps:
1149 Implications for allanite-monzazite-xenotime phase relations from 250 to 610°C. *Journal of*
1150 *Metamorphic Geology*, 26(5), 509–526. <https://doi.org/10.1111/j.1525-1314.2008.00774.x>
- 1151 Janots, E., Engi, M., Rubatto, D., Berger, A., Gregory, C., & Rahn, M. (2009).
1152 Metamorphic rates in collisional orogeny from in situ allanite and monazite dating. *Geology*,
1153 37(1), 11–14. <https://doi.org/10.1130/G25192A.1>
- 1154 Jébrak, M. (1997). Hydrothermal breccias in vein-type ore deposits: A review of
1155 mechanisms, morphology and size distribution. *Ore Geology Reviews*, 12(3), 111–134.
1156 [https://doi.org/10.1016/S0169-1368\(97\)00009-7](https://doi.org/10.1016/S0169-1368(97)00009-7)
- 1157 Jenkin, G. R., Ellam, R. M., Rogers, G., & Stuart, F. M. (2001). An investigation of
1158 closure temperature of the biotite Rb-Sr system: The importance of cation exchange. *Geochimica*
1159 *et Cosmochimica Acta*, 65(7), 1141–1160. [https://doi.org/10.1016/S0016-7037\(00\)00560-3](https://doi.org/10.1016/S0016-7037(00)00560-3)
- 1160 Kralik, M., Clauer, N., Holnsteiner, R., Huemer, H., & Kappel, F. (1992). Recurrent fault
1161 activity in the Grimsel Test Site (GTS, Switzerland) : revealed by Rb-Sr, K-Ar and tritium
1162 isotope techniques. *Journal - Geological Society (London)*, 149(2), 293–301.
1163 <https://doi.org/10.1144/GSJGS.149.2.0293>
- 1164 Lacombe, O., & Mouthereau, F. (2002). Basement-involved shortening and deep
1165 detachment tectonics in forelands of orogens: Insights from recent collision belts (Taiwan,
1166 Western Alps, Pyrenees). *Tectonics*, 21(4), 12–1. <https://doi.org/10.1029/2001TC901018>
- 1167 Lemoine, M., Bas, T., Arnaud-Vanneau, A., Arnaud, H., Dumont, T., Gidon, M., et al.
1168 (1986). The continental margin of the Mesozoic Tethys in the Western Alps. *Marine and*
1169 *Petroleum Geology*, 3(3), 179–199. [https://doi.org/10.1016/0264-8172\(86\)90044-9](https://doi.org/10.1016/0264-8172(86)90044-9)
- 1170 Leydier, T., Goncalves, P., Lanari, P., & Oliot, E. (2019). On the petrology of brittle
1171 precursors of shear zones – An expression of concomitant brittle deformation and fluid–rock
1172 interactions in the ‘ductile’ continental crust? *Journal of Metamorphic Geology*, 37(8), 1129–
1173 1149. <https://doi.org/10.1111/jmg.12504>
- 1174 Lützenkirchen, V., & Loew, S. (2011). Late Alpine brittle faulting in the Rotondo granite
1175 (Switzerland): Deformation mechanisms and fault evolution. *Swiss Journal of Geosciences*,
1176 104(1), 31–54. <https://doi.org/10.1007/s00015-010-0050-0>
- 1177 Ma, X., Hertrich, M., Amann, F., Bröker, K., Doonechaly, N. G., Gischig, V., et al.
1178 (2022). Multi-disciplinary characterizations of the BedrettoLab-A new underground geoscience
1179 research facility. *Solid Earth*, 13(2), 301–322. <https://doi.org/10.5194/se-13-301-2022>
- 1180 Mancktelow, N., & Pennacchioni, G. (2010). Why calcite can be stronger than quartz.
1181 *Journal of Geophysical Research: Solid Earth*, 115(10), 1–16.
1182 <https://doi.org/10.1029/2009JB006526>
- 1183 Mancktelow, N., & Pennacchioni, G. (2020). Intermittent fracturing in the middle
1184 continental crust as evidence for transient switching of principal stress axes associated with the

- 1185 subduction zone earthquake cycle. *Geology*, 48(11), 1072–1076.
1186 <https://doi.org/10.1130/G47625.1>
- 1187 McDonough, W. F., & Sun, S. S. (1995). The composition of the Earth. *Chemical*
1188 *geology*, 120(3-4), 223-253. [https://doi.org/10.1016/0009-2541\(94\)00140-4](https://doi.org/10.1016/0009-2541(94)00140-4)
- 1189 Melosh, B. L., Rowe, C. D., Smit, L., Groenewald, C., Lambert, C. W., & Macey, P.
1190 (2014). Snap, Crackle, Pop: Dilational fault breccias record seismic slip below the brittle–plastic
1191 transition. *Earth and Planetary Science Letters*, 403, 432-445.
1192 <https://doi.org/10.1016/j.epsl.2014.07.002>
- 1193 Menegon, L., & Pennacchioni, G. (2010). Local shear zone pattern and bulk deformation
1194 in the Gran Paradiso metagranite (NW Italian Alps). *International Journal of Earth Sciences*,
1195 99(8), 1805–1825. <https://doi.org/10.1007/S00531-009-0485-6>
- 1196 Menegon, L., Nasipuri, P., Stünitz, H., Behrens, H., & Ravna, E. (2011). Dry and strong
1197 quartz during deformation of the lower crust in the presence of melt. *Journal of Geophysical*
1198 *Research: Solid Earth*, 116(B10). <https://doi.org/10.1029/2011JB008371>
- 1199 Mohn, G., Manatschal, G., Beltrando, M., & Hauptert, I. (2014). The role of rift-inherited
1200 hyper-extension in Alpine-type orogens. *Terra Nova*, 26(5), 347-353.
1201 <https://doi.org/10.1111/ter.12104>
- 1202 Mouthereau, F., Watts, A. B., & Burov, E. (2013). Structure of orogenic belts controlled
1203 by lithosphere age. *Nature geoscience*, 6(9), 785-789. <https://doi.org/10.1038/ngeo1902>
- 1204 Musso Piantelli, F., Mair, D., Berger, A., Schlunegger, F., Wiederkehr, M., Kurmann, E.,
1205 et al. (2022). 4D reconstruction of the Doldenhorn nappe-basement system in the Aar massif:
1206 Insights into late-stage continent-continent collision in the Swiss Alps. *Tectonophysics*, 843,
1207 229586. <https://doi.org/10.1016/J.TECTO.2022.229586>
- 1208 Newton, R. C., Charlu, T. V., & Kleppa, O. J. (1980). Thermochemistry of the high
1209 structural state plagioclases. *Geochimica et Cosmochimica Acta*. [https://doi.org/10.1016/0016-](https://doi.org/10.1016/0016-7037(80)90283-5)
1210 [7037\(80\)90283-5](https://doi.org/10.1016/0016-7037(80)90283-5)
- 1211 Nibourel, L., Berger, A., Egli, D., Heuberger, S., & Herwegh, M. (2021). Structural and
1212 thermal evolution of the eastern Aar Massif: insights from structural field work and Raman
1213 thermometry. *Swiss Journal of Geosciences*, 114(1). [https://doi.org/10.1186/s00015-020-00381-](https://doi.org/10.1186/s00015-020-00381-3)
1214 [3](https://doi.org/10.1186/s00015-020-00381-3)
- 1215 Oliot, E., Goncalves, P., & Marquer, D. (2010). Role of plagioclase and reaction
1216 softening in a metagranite shear zone at mid-crustal conditions (Gotthard Massif, Swiss Central
1217 Alps). *Journal of Metamorphic Geology*, 28(8), 849–871. [https://doi.org/10.1111/j.1525-](https://doi.org/10.1111/j.1525-1314.2010.00897.x)
1218 [1314.2010.00897.x](https://doi.org/10.1111/j.1525-1314.2010.00897.x)
- 1219 Oliot, E., Goncalves, P., Schulmann, K., Marquer, D., & Lexa, O. (2014). Mid-crustal
1220 shear zone formation in granitic rocks: Constraints from quantitative textural and
1221 crystallographic preferred orientations analyses. *Tectonophysics*, 612–613, 63–80.
1222 <https://doi.org/10.1016/j.tecto.2013.11.032>
- 1223 Paton, C., Hellstrom, J., Paul, B., Woodhead, J. and Hergt, J. (2011) Iolite: Freeware for
1224 the visualisation and processing of mass spectrometric data. *Journal of Analytical Atomic*
1225 *Spectrometry*. doi:10.1039/c1ja10172b.

- 1226 Pennacchioni, G., Di Toro, G., Brack, P., Menegon, L., & Villa, I. M. (2006). Brittle–
1227 ductile–brittle deformation during cooling of tonalite (Adamello, Southern Italian Alps).
1228 *Tectonophysics*, 427(1-4), 171-197. <https://doi.org/10.1016/j.tecto.2006.05.019>
- 1229 Pennacchioni, G., Ceccato, A., Fioretti, A. M., Mazzoli, C., Zorzi, F., & Ferretti, P.
1230 (2016). Episyenites in meta-granitoids of the Tauern Window (Eastern Alps): unpredictable?
1231 *Journal of Geodynamics*, 101, 73–87. <https://doi.org/10.1016/j.jog.2016.04.001>
- 1232 Pfiffner, O. A. (2016). Basement-involved thin-skinned and thick-skinned tectonics in the
1233 Alps. *Geological Magazine*, 153(5-6), 1085-1109. doi:10.1017/S0016756815001090
- 1234 Piccolo, A., Faccenda, M., Carosi, R., Montomoli, C., & Visonà, D. (2018). Crustal
1235 strength control on structures and metamorphism in collisional orogens. *Tectonophysics*, 746,
1236 470-492. <https://doi.org/10.1016/j.tecto.2017.09.018>
- 1237 Pleuger, J., Mancktelow, N., Zwingmann, H., & Manser, M. (2012). K–Ar dating of
1238 synkinematic clay gouges from Neoalpine faults of the Central, Western and Eastern Alps.
1239 *Tectonophysics*, 550–553, 1–16. <https://doi.org/10.1016/J.TECTO.2012.05.001>
- 1240 Pozzi, G., Scuderi, M. M., Tinti, E., Nazzari, M., & Collettini, C. (2022). The role of fault
1241 rock fabric in the dynamics of laboratory faults. *Journal of Geophysical Research: Solid Earth*,
1242 127(6), e2021JB023779. <https://doi.org/10.1029/2021JB023779>
- 1243 Redaa A., Farkaš J., Gilbert S., Collins A. S., Wade B., Löhr S., Zack T. & Garbe-
1244 Schönberg D. (2021) Assessment of elemental fractionation and matrix effects during in situ Rb–
1245 Sr dating of phlogopite by LA-ICP-MS/MS: implications for the accuracy and precision of
1246 mineral ages. *Journal of Analytical Atomic Spectrometry* 36, 322-344. DOI:
1247 <https://doi.org/10.1039/D0JA00299B>
- 1248 Redaa A., Farkaš J., Gilbert S., Collins A. S., Löhr S., Vasegh D., Forster M., Blades M.,
1249 Zack T., Giuliani A., Maas R., Baldermann A., Dietzel M. & Garbe-Schönberg D. (2023)
1250 Testing Nano-Powder and Fused-Glass Mineral Reference Materials for In Situ Rb-Sr Dating of
1251 Glauconite, Phlogopite, Biotite and Feldspar via LA-ICP-MS/MS. *Geostandards and*
1252 *Geoanalytical Research* 47, 23-48. <https://doi.org/10.1111/ggr.12467>
- 1253 Ribeiro, B. V., Kirkland, C. L., Kelsey, D. E., Reddy, S. M., Hartnady, M. I., Faleiros, F.
1254 M., ... & Clark, C. (2023). Time-strain evolution of shear zones from petrographically
1255 constrained Rb–Sr muscovite analysis. *Earth and Planetary Science Letters*, 602, 117969.
1256 <https://doi.org/10.1016/j.epsl.2022.117969>
- 1257 Rast, M., Galli, A., Ruh, J. B., Guillong, M., & Madonna, C. (2022). Geology along the
1258 Bedretto tunnel: kinematic and geochronological constraints on the evolution of the Gotthard
1259 Massif (Central Alps). *Swiss Journal of Geosciences*, 115(1). <https://doi.org/10.1186/s00015-022-00409-w>
- 1261 Ricchi, E., Bergemann, C., Gnos, E., Berger, A., Rubatto, D., & Whitehouse, M. J.
1262 (2019). Constraining deformation phases in the Aar Massif and the Gotthard Nappe
1263 (Switzerland) using Th-Pb crystallization ages of fissure monazite-(Ce). *Lithos*, 342–343, 223–
1264 238. <https://doi.org/10.1016/J.LITHOS.2019.04.014>
- 1265 Rolland, Y., & Rossi, M. (2016). Two-stage fluid flow and element transfers in shear
1266 zones during collision burial-exhumation cycle: Insights from the Mont Blanc Crystalline Massif
1267 (Western Alps). *Journal of Geodynamics*, 101, 88-108. <https://doi.org/10.1016/j.jog.2016.03.016>

- 1268 Rolland, Y., Rossi, M., Cox, S. F., Corsini, M., Mancktelow, N., Pennacchioni, G., et al.
1269 (2008). $^{40}\text{Ar}/^{39}\text{Ar}$ dating of synkinematic white mica: Insights from fluid-rock reaction in low-
1270 grade shear zones (Mont Blanc Massif) and constraints on timing of deformation in the NW
1271 external Alps. *Geological Society Special Publication*, 299, 293–315.
1272 <https://doi.org/10.1144/SP299.18>
- 1273 Rolland, Y., Cox, S. F., & Corsini, M. (2009). Constraining deformation stages in brittle-
1274 ductile shear zones from combined field mapping and $^{40}\text{Ar}/^{39}\text{Ar}$ dating: The structural
1275 evolution of the Grimsel Pass area (Aar Massif, Swiss Alps). *Journal of Structural Geology*,
1276 31(11), 1377–1394. <https://doi.org/10.1016/j.jsg.2009.08.003>
- 1277 Rosenberg, C. L., & Kissling, E. (2013). Three-dimensional insight into Central-Alpine
1278 collision: Lower-plate or upper-plate indentation? *Geology*, 41(12), 1219–1222.
1279 <https://doi.org/10.1130/G34584.1>
- 1280 Rosenberg, C. L., Bellahsen, N., Rabaute, A., & Girault, J. B. (2021). Distribution, style,
1281 amount of collisional shortening, and their link to Barrovian metamorphism in the European
1282 Alps. *Earth-Science Reviews*, 222, 103774. <https://doi.org/10.1016/j.earscirev.2021.103774>
- 1283 Rubatto, D., Hermann, J., Berger, A., & Engi, M. (2009). Protracted fluid-induced
1284 melting during Barrovian metamorphism in the Central Alps. *Contributions to Mineralogy and
1285 Petrology*, 158, 703–722. <https://doi.org/10.1007/s00410-009-0406-5>
- 1286 Sanchez, G., Rolland, Y., Schneider, J., Corsini, M., Oliot, E., Goncalves, P., Verati, C.,
1287 Lardeaux, J.M. & Marquer, D. (2011). Dating low-temperature deformation by $^{40}\text{Ar}/^{39}\text{Ar}$ on
1288 white mica, insights from the Argentera-Mercantour Massif (SW Alps). *Lithos*, 125(1–2), 521–
1289 536. <https://doi.org/10.1016/J.LITHOS.2011.03.009>
- 1290 Sarkar, S., Giuliani, A., Dalton, H., Phillips, D., Ghosh, S., Misev, S., & Maas, R. (2023).
1291 Derivation of Lamproites and Kimberlites from a Common Evolving Source in the Convective
1292 Mantle: the Case for Southern African ‘Transitional Kimberlites’. *Journal of Petrology*, 64(7),
1293 egad043. <https://doi.org/10.1093/petrology/egad043>
- 1294 Schmid, S. M., Fügenschuh, B., Kissling, E., & Schuster, R. (2004). Tectonic map and
1295 overall architecture of the Alpine orogen. *Eclogae Geologicae Helvetiae*, 97(1), 93–117.
1296 <https://doi.org/10.1007/S00015-004-1113-X>
- 1297 Seman, S., Stockli, D.F., and McLean, N.M., 2017, U-Pb geochronology of grossular-
1298 andradite garnet: *Chemical Geology*, v. 460, p. 106–116, doi:10.1016/j.chemgeo.2017.04.020.
- 1299 Sibson, R. H. (1985). Stopping of earthquake ruptures at dilational fault jogs. *Nature*,
1300 316(6025), 248–251. <https://doi.org/10.1038/316248a0>
- 1301 Sibson, R. H. (1987). Earthquake rupturing as a mineralizing agent in hydrothermal
1302 systems. *Geology*, 15(8), 701–704. [https://doi.org/10.1130/0091-
1303 7613\(1987\)15%3C701:ERAAMA%3E2.0.CO;2](https://doi.org/10.1130/0091-7613(1987)15%3C701:ERAAMA%3E2.0.CO;2)
- 1304 Sibson, R. H. (2003). Brittle-failure controls on maximum sustainable overpressure in
1305 different tectonic regimes. *American Association of Petroleum Geologists Bulletin*, 87(6), 901–
1306 908. <https://doi.org/10.1306/01290300181>

- 1307 Sibson, R. H., Robert, F., & Poulsen, K. H. (1988). High-angle reverse faults, fluid-
1308 pressure cycling, and mesothermal gold-quartz deposits. *Geology*, 16(June), 551–555.
1309 [https://doi.org/doi.org/10.1130/0091-7613\(1988\)016%3C0551:HARFFP%3E2.3.CO;2](https://doi.org/doi.org/10.1130/0091-7613(1988)016%3C0551:HARFFP%3E2.3.CO;2)
- 1310 Simonetti, M., Carosi, R., Montomoli, C., Cottle, J. M., & Law, R. D. (2020).
1311 Transpressive Deformation in the Southern European Variscan Belt: New Insights From the
1312 Aiguilles Rouges Massif (Western Alps). *Tectonics*, 39(6), e2020TC006153.
1313 <https://doi.org/10.1029/2020TC006153>
- 1314 Spear, F. S. (2010). Monazite–allanite phase relations in metapelites. *Chemical Geology*,
1315 279(1-2), 55-62. <https://doi.org/10.1016/j.chemgeo.2010.10.004>
- 1316 Steck, A. (1976). Albit-Oligoklas-Mineralgesellschaften der Peristeritlücke aus
1317 alpinmetamorphen Granitgneisen des Gotthardmassivs. *Schweizerische Mineralogische Und*
1318 *Petrographische Mitteilungen*, 56, 269–292. <https://doi.org/10.5169/seals-43687>
- 1319 Steck, A., & Burri, G. (1971). Chemismus und Paragenesen von Granaten aus
1320 Granitgneisen der Grünschiefer- und Amphiholitfazies der Zentralalpen. *Schweizerische*
1321 *Mineralogische Und Petrographische Mitteilungen*, 51(2–3), 534–538.
- 1322 Vanardois, J., Trap, P., Roger, F., Melleton, J., Marquer, D., Paquette, J. L., Goncalves,
1323 P., Cagnard, F., & Le Bayon, B. (2022). Deformation, crustal melting and magmatism in the
1324 crustal-scale East-Variscan Shear Zone (Aiguilles-Rouges and Mont-Blanc massifs, Western
1325 Alps). *Journal of Structural Geology*, 163, 104724. <https://doi.org/10.1016/J.JSG.2022.104724>
- 1326 Vermeesch, P. (2018). IsoplotR: A free and open toolbox for geochronology. *Geoscience*
1327 *Frontiers*, 9(5), 1479-1493. <https://doi.org/10.1016/j.gsf.2018.04.001>
- 1328 Vogt, K., Willingshofer, E., Matenco, L., Sokoutis, D., Gerya, T., & Cloetingh, S. (2018).
1329 The role of lateral strength contrasts in orogenesis: A 2D numerical study. *Tectonophysics*, 746,
1330 549–561. <https://doi.org/10.1016/J.TECTO.2017.08.010>
- 1331 Volpe, G., Pozzi, G., & Colletini, C. (2022). YBPR or SCC'? Suggestion for the
1332 nomenclature of experimental brittle fault fabric in phyllosilicate-granular mixtures. *Journal of*
1333 *Structural Geology*, 165, 104743. <https://doi.org/10.1016/j.jsg.2022.104743>
- 1334 Volpe, G., Pozzi, G., Colletini, C., Spagnuolo, E., Achtziger-Zupančič, P., Zappone, A.,
1335 Aldega, L., Meier, M.A., Giardini, D., & Cocco, M. (2023). Laboratory simulation of fault
1336 reactivation by fluid injection and implications for induced seismicity at the BedrettoLab, Swiss
1337 Alps. *Tectonophysics*, 862, 229987. <https://doi.org/10.1016/j.tecto.2023.229987>
- 1338 Waldbaum, D. R., & Thompson Jr., J. B. (1968). Mixing properties of sanidine
1339 crystalline solutions; [Part] 2, Calculations based on volume data. *American Mineralogist*.
- 1340 Wehrens, P., Berger, A., Peters, M., Spillmann, T., & Herwegh, M. (2016). Deformation
1341 at the frictional-viscous transition: Evidence for cycles of fluid-assisted embrittlement and
1342 ductile deformation in the granitoid crust. *Tectonophysics*, 693, 66–84.
1343 <https://doi.org/10.1016/j.tecto.2016.10.022>
- 1344 Weisenberger, T., & Bucher, K. (2010). Zeolites in fissures of granites and gneisses of
1345 the Central Alps. *Journal of Metamorphic Geology*, 28(8), 825–847.
1346 <https://doi.org/10.1111/J.1525-1314.2010.00895.X>

- 1347 White, R. W., Powell, R., Holland, T. J. B., Johnson, T. E., & Green, E. C. R. (2014).
1348 New mineral activity–composition relations for thermodynamic calculations in metapelitic
1349 systems. *Journal of Metamorphic Geology*, 32(3), 261–286. <https://doi.org/10.1111/JMG.12071>
- 1350 Whitney, D. L., & Evans, B. W. (2010). Abbreviations for names of rock-forming
1351 minerals. *American Mineralogist*, 95(1), 185–187. <https://doi.org/10.2138/am.2010.3371>
- 1352 Wiederkehr, M., Bousquet, R., Ziemann, M. A., Berger, A., & Schmid, S. M. (2011). 3-D
1353 assessment of peak-metamorphic conditions by Raman spectroscopy of carbonaceous material:
1354 An example from the margin of the Lepontine dome (Swiss Central Alps). *International Journal*
1355 *of Earth Sciences*, 100(5), 1029–1063. <https://doi.org/10.1007/S00531-010-0622-2>
- 1356 Willingshofer, E., Sokoutis, D., & Burg, J. P. (2005). Lithospheric-scale analogue
1357 modelling of collision zones with a pre-existing weak zone. *Geological Society, London, Special*
1358 *Publications*, 243(1), 277-294. <https://doi.org/10.1144/GSL.SP.2005.243.01.18>
- 1359 Wolf, S. G., Huisman, R. S., Braun, J., & Yuan, X. (2022). Topography of mountain
1360 belts controlled by rheology and surface processes. *Nature*, 606(7914), 516-521.
1361 <https://doi.org/10.1038/s41586-022-04700-6>
- 1362 Zertani, S., Menegon, L., Pennacchioni, G., Buisman, I., Corfu, F., & Jamtveit, B. (2023).
1363 Protracted localization of metamorphism and deformation in a heterogeneous lower-crustal shear
1364 zone. *Journal of Structural Geology*, 104960. <https://doi.org/10.1016/j.jsg.2023.104960>

1 **Structural evolution, exhumation rates, and rheology of the European crust**
2 **during Alpine collision: constraints from the Rotondo granite – Gotthard nappe**
3

4 **A. Ceccato¹, W. M. Behr¹, A. S. Zappone², L. Tavazzani³, and A. Giuliani³**

5
6 ¹Structural Geology and Tectonics Group, Geological Institute, Department of Earth Sciences,
7 ETH Zurich, Sonneggstrasse 5, 8092 Zurich, Switzerland.

8 ²Swiss Seismological Service, ETHZ, Zurich, 8092, Switzerland.

9 ³Institute of Geochemistry and Petrology, Department of Earth Sciences, ETH Zurich,
10 Clausiusstrasse 25, 8092 Zurich, Switzerland.

11
12 Corresponding author: Alberto Ceccato (aceccato@erdw.ethz.ch)
13

14 **Key Points:**

- 15 • Garnet U-Pb, mica Rb-Sr dating constrain exhumation of Rotondo granite from
16 amphibolite facies at 34-20 Ma to greenschist facies at 15-14 Ma
- 17 • Fast exhumation (1-3 mm/yr) accommodated by ductile shearing of weak shear zones
18 localized on pre-collisional brittle deformation structures
- 19 • The European crust was extremely weak during collision, rheology was controlled by
20 metamorphic and fluid evolution in localized shear zones
21

22

Abstract

23

24

25

26

27

28

29

30

31

32

33

34

35

36

37

38

39

40

41

42

43

1 Introduction

44

45

46

47

48

49

50

51

52

53

54

55

56

57

58

59

60

61

62

63

64

65

The rheology of crystalline units controls the large-scale deformation geometry and dynamics of collisional orogens. Defining a time-constrained rheological evolution of such units may help unravel the details of collisional dynamics. Here, we integrate field analysis, pseudosection calculations and in-situ garnet U-Pb and mica Rb-Sr geochronology to define the structural and rheological evolution of the Rotondo granite (Gotthard nappe, Central Alps). We identify a sequence of four (D₁-D₄) deformation stages. Pre-collisional D₁ brittle faults developed before Alpine peak metamorphism, which occurred at 34-20 Ma (U-Pb garnet ages) at 590 ± 25°C and 0.95 ± 0.1 GPa. The reactivation of D₁ structures controlled the rheological evolution, from D₂ reverse mylonitic shearing at amphibolite facies (520 ± 40°C and 0.85 ± 0.1 GPa) at 18-20 Ma (white mica Rb-Sr ages), to strike-slip, brittle-ductile shearing at greenschist-facies D₃ (395 ± 25 °C and 0.4 ± 0.1 GPa) at 14-15 Ma (white and dark mica Rb-Sr ages), and then to D₄ strike-slip faulting at shallow conditions. Although highly misoriented for the Alpine collisional stress orientation, D₁ brittle structures controlled the localization of D₂ ductile mylonites accommodating fast (1-3 mm/yr) exhumation rates due to their weak shear strength (<10 MPa). This structural and rheological evolution is common across External Crystalline Massifs (e.g., Aar, Mont Blanc), suggesting that the entire European crust was extremely weak during Alpine collision, its strength controlled by weak ductile shear zones localized on pre-collisional deformation structures, that in turn controlled localized exhumation at the scale of the orogen.

During mountain-building events, rheological contrasts between lithospheric plates are first-order controls on the geometry of collision (Faccenda et al., 2008; Vogt et al., 2018, Candiotti et al., 2021), the development of topography (Cook & Royden, 2008; Wolf et al., 2022), and the styles and rates of regional deformation and metamorphism (Willingshofer et al., 2005; Piccolo et al., 2018). Rheological contrasts may result from different crustal compositions, ages, geological histories, and/or thermal regimes of the lithospheric plates involved in collision (Audet & Burgmann, 2011; Mouthereau et al., 2013). For example, depending on the composition and the fluid content, lithospheric plates may present different mechanical behavior (brittle vs. viscous deformation) and strength at the same depth and temperature conditions during collision (Bürgmann & Dresen, 2008; Menegon et al., 2011; Behr & Platt, 2014, Jamtveit et al., 2019). Furthermore, the occurrence of anisotropic structural fabrics (foliations and fractures), strictly related to the geological history of crustal sections, may promote or hinder deformation depending on their suitability to be reactivated, and/or their ability to promote or hinder fluid infiltration (Ceccato et al., 2020, Zertani et al., 2023). Pressure, temperature, fluid, and structural fabrics evolve with the tectono-metamorphic evolution of a collisional orogen, and so does their effects on the rheological contrast between colliding plates (Groome et al., 2008; Behr & Platt, 2013; Bellanger et al., 2014; Ceccato et al., 2020).

Most of the deformation and shortening in the core of collisional belts is accommodated through deformation of crystalline basement units (Lacombe & Mouthereau, 2002; Rosenberg & Kissling, 2013; Pfiffner, 2016). Such crystalline units are typically characterized by poly-metamorphic histories, with wet and/or dry mineral assemblages, and multiple tectonic fabrics, all of them strongly affecting the rheology during collision (Audet & Burgmann, 2011;

66 Mouterau et al., 2013). Moreover, pre-collisional events such as lithospheric rifting, prograde
67 burial, and subduction, lead to the development of additional deformation structures (e.g., rift-
68 related normal fault zones) and tectonic fabrics (e.g., prograde foliations), which may introduce
69 rheological heterogeneity that later influences collisional dynamics (Mohn et al., 2014). The
70 European Alps is a region where both inherited compositional and fabric variations, as well as
71 pre-collisional tectonics, are thought to have strongly influenced later syn-orogenic development.
72 For example, rheological contrast between the upper (Adriatic) and lower (European) crust
73 varies along the strike of the orogen, and resulted in different patterns of strain partitioning,
74 amounts of shortening and exhumation, and collisional styles between the Western, Central and
75 Eastern Alps (Bellahsen et al., 2014; Rosenberg & Kissling, 2013). In the Central Alps, in
76 particular, the Adriatic upper plate indents into the weaker, thickened European crust (Rosenberg
77 & Kissling, 2013). The European thickened crust is composed of stacked slices of crystalline
78 basement derived from the thinned Mesozoic European margin, now exposed in the Aar massif,
79 Gotthard nappe, and Lepontine dome (Fig. 1). The thickened European crust is considered here
80 to be much weaker than the juxtaposed Adriatic continental lithosphere, represented by the
81 almost undeformed, lower-crustal Ivrea-Verbano complex (Fig. 1). However, constraints on the
82 factors controlling this “weakness” are sparse, including whether the crust was weak since the
83 beginning of burial and subduction, or if it was initially strong and then progressively weakened
84 during collision. Both tectonic inheritance related to Mesozoic rifting (Bellahsen et al., 2014) and
85 syn-collisional Barrovian metamorphism (Rosenberg & Kissling, 2013) might have contributed
86 to the weakening of the European continental crust in this part of the Alps.

87 To better understand this weakening process, and the extent to which different factors
88 (temperature, fluids, inherited fabrics) contributed to it, a detailed characterization of the
89 structural and rheological evolution of the crystalline basement is required. Providing a time-
90 integrated evolution of the rheology and of the geological parameters controlling this evolution
91 might help us to quantitatively constrain the relationship between the rheology of crystalline
92 basement units and the large-scale geometry and dynamics of the Alpine orogen.

93 In this regard, previous investigations have revealed a recurrent brittle-to-ductile
94 structural evolution (i.e., ductile shear zone related to collisional processes overprinting pre-
95 existent brittle faults and fractures) of crystalline basement units in the Western and Central Alps
96 (e.g., Mont Blanc: Guermani & Pennacchioni, 1998; Gran Paradiso: Menegon & Pennacchioni,
97 2010; Aar-Gotthard: Oliot et al., 2014; Rolland et al., 2009; Wehrens et al., 2016; Lepontine
98 Dome: Goncalves et al., 2016). Several hypotheses were proposed to explain such brittle-to-
99 ductile evolution, including the occurrence of prograde brittle deformation during burial
100 (Guermani & Pennacchioni, 1998), and mid-crustal seismicity at peak metamorphic conditions
101 (Wehrens et al., 2016). Previous authors have also speculated on the occurrence of pervasive
102 extensional faulting related to the Mesozoic rifting of the European margin, providing field
103 evidence for limited reactivation of structures inherited from rifting (Ballèvre et al., 2018;
104 Dall’Asta et al., 2022; Herwegh et al., 2017, 2020; Nibourel et al. 2021; Musso-Piantelli et al.,
105 2022).

106 Here we present an integrated field and petrochronological study of the deformation
107 features of the Rotondo granite in the Gotthard nappe (Fig. 1). The Gotthard nappe represents a
108 sliver of European crust now exposed in the Central Swiss Alps. The Rotondo granite is a Post-
109 Variscan pluton (i.e., not affected by Variscan tectonometamorphic events), intruded into the
110 European polymetamorphic crust. Differently from its host polymetamorphic host rock, the lack

111 of Variscan pervasive fabrics (foliations) and the homogeneous texture of the granite allow us to
 112 define a sequence of (localized) deformation structures probably related to Alpine deformation.
 113 We use structural and petrochronological data to:

- 114 i. Define the pressure-temperature-time-deformation (P - T - t - d) path of the Rotondo
 115 granite;
- 116 ii. Examine the time-constrained structural and rheological evolution of the
 117 thickened crust of the lower plate during Alpine continental collision;
- 118 iii. Investigate the geological factors that affect the rheological evolution of the
 119 crystalline unit.

120 **2 Geological setting**

121 The European Alps (Fig. 1) are a double-verging orogen resulting from the continental
 122 collision between Europe and Adria, following the closure and subduction of the Mesozoic
 123 Tethys ocean (Dal Piaz et al., 2003). European and Adriatic polymetamorphic crustal sections
 124 were each strongly modified by the Variscan orogeny during the formation of the Pangean
 125 supercontinent. The Permo-Mesozoic breakup of Pangea led to the development of the Tethys
 126 Ocean, including the Liguro-Piemontese ocean and Valais trough. The development of the
 127 Liguro-Piemontese ocean divided Europe from Adria (210-140 Ma) by 200-400 km (Ballèvre et
 128 al., 2018; Beltrando et al., 2014). A second, more short-lived rifting phase took place on the
 129 European margin to the north of the Liguro-Piemontese ocean and led to the development of the
 130 Valais trough during Late-Jurassic to Early Cretaceous (140-120 Ma), separating the European
 131 distal margin from the southern Briançonnais microcontinent (Beltrando et al., 2012; Célini et
 132 al., 2023; Handy et al., 2010). This former paleogeography is now preserved in the Internal
 133 (Penninic) domains of the Central and Western Alps, exposing the remnants of the Valaisan,
 134 Briançonnais and Liguro-Piemontese units (Fig. 1). The proximal European passive margin is
 135 now exposed in the External Crystalline Massifs (ECMs), including: Aar, Mont Blanc, Aiguille
 136 Rouges, Belledonne, Pelvoux-Oisian massifs as well as in the Gotthard nappe (Fig. 1a; Lemoine
 137 et al., 1986).

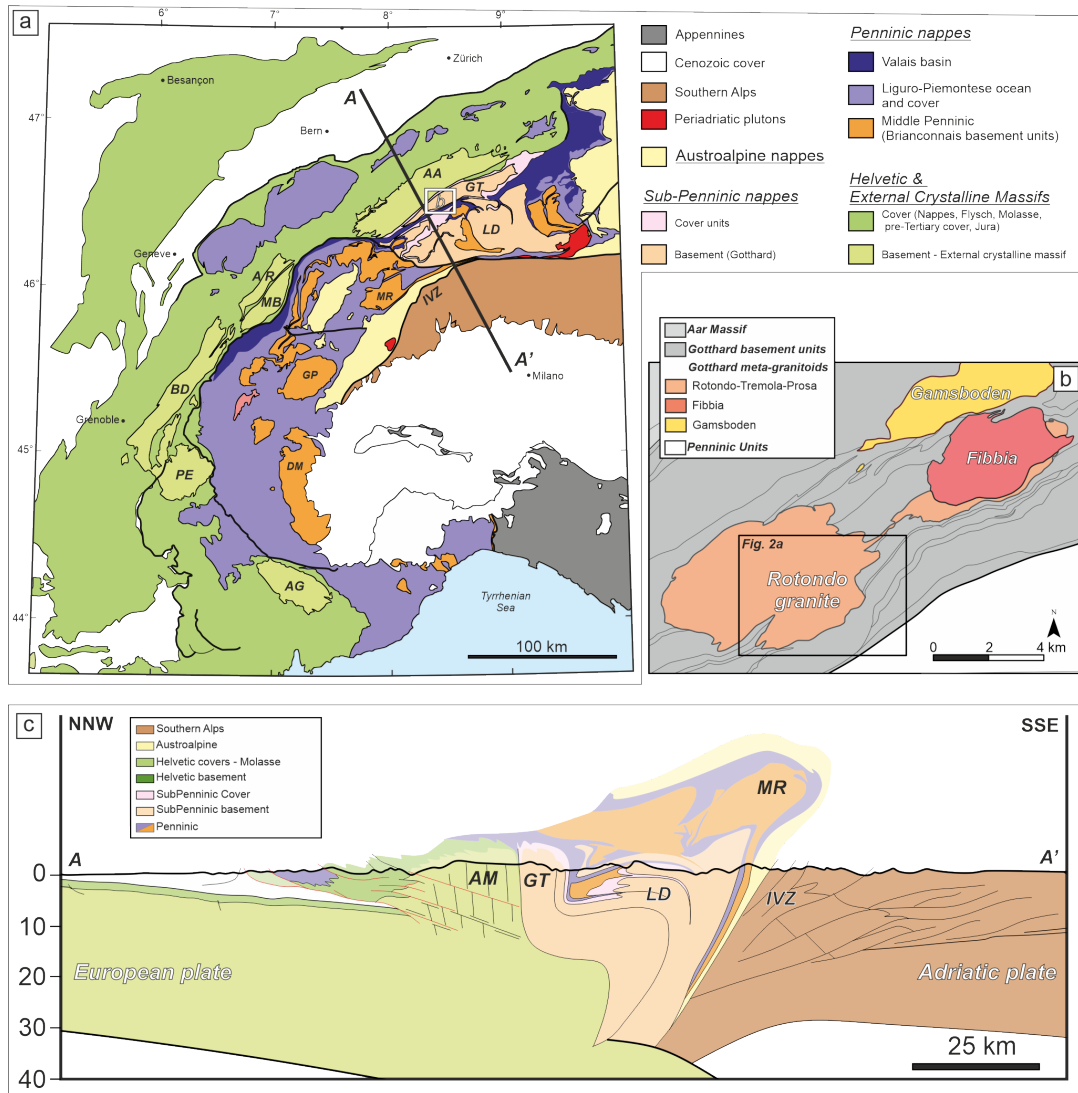
138 The study area is located in the Gotthard nappe (Swiss Alps, Fig. 1a). The Gotthard
 139 nappe includes a series of polymetamorphic Ordovician-Silurian crystalline units intruded by
 140 late-Variscan granitoids (Berger et al., 2017). The crystalline units include high-grade gneisses of
 141 the Val Nalps, Paradis and Streifegneis complexes (Fig. 2a; Berger et al., 2017). The Val Nalps
 142 and Paradis Complexes preserve evidence of an Early- to Mid-Ordovician (~470 Ma) high grade
 143 metamorphism, later affected by Silurian (~440 Ma) magmatism (Berger et al., 2017). Between
 144 340 and 300 Ma, these complexes were affected by Variscan amphibolite facies metamorphism
 145 and transpressional shearing (Bühler et al., 2022; Simonetti et al., 2020; Vanardois et al., 2022).
 146 Post-Variscan magmatism led to the intrusion of several granitic plutons into the
 147 polymetamorphic basement, including the Cristallina granodiorite, the Fibbia and Gamsboden
 148 granite-gneisses and the Rotondo granite (Fig., 1b; Berger et al., 2017).

149 At the regional scale, the European crust was affected by the development of Permo-
 150 Mesozoic transtensional basins, resulting eventually in the formation of the Valais trough in the
 151 Jurassic-Cretaceous period (Ballèvre et al., 2018; Célini et al., 2023; Handy et al., 2010). The
 152 units now included in the Gotthard nappe were part of the distal European passive margin
 153 located north of the Valais trough (Schmid et al., 2004). From the Late Cretaceous onwards,
 154 convergence between Europe and Adria led to the subduction of the Liguro-Piemontese ocean

155 and to progressive development of the Penninic accretionary wedge facing the advancing
156 Adriatic upper plate (Dal Piaz et al., 2003). Progressive convergence led to burial and
157 underthrusting of the European passive margin, eventually leading to continental collision. The
158 Gotthard nappe was buried beneath the advancing Penninic accretionary wedge around 35 Ma
159 (Handy et al., 2010), reaching greenschist-facies conditions between 35 and 22 Ma (Herwegh et
160 al., 2020; Janots et al., 2009). Subsequently, continental collision between Europe and Adria led
161 to the rapid exhumation of the crystalline units of the Gotthard-Aar massifs at around 22-17 Ma,
162 through the activation of greenschist facies sub-vertical ductile shear zones with reverse
163 kinematics ($T = 450\text{-}500\text{ }^{\circ}\text{C}$ and $P = 0.7\text{-}0.8\text{ GPa}$; Challandes et al., 2008; Goncalves et al., 2012;
164 Herwegh et al., 2017; Oliot et al., 2010; Rolland et al., 2008, 2009). From 14 Ma onward, the
165 Gotthard nappe was then affected by regional strike-slip tectonics related to the activity of the
166 Simplon-Rhone transtensional fault system (Campani et al., 2010; Herwegh et al., 2017).
167 Shallow brittle faulting has affected the Gotthard nappe since the Late Miocene, leading to the
168 activation of brittle gouge-bearing faults up to recent times (Kralik et al., 1992; Pleuger et al.,
169 2012).

170 2.1 The Rotondo granite

171 The Rotondo Granite (RG) is an Early-Permian (295 Ma, U-Pb on zircon, Rast et al.,
172 2022) peraluminous granite, crosscut by mafic dykes (290-285 Ma, U-Pb on zircon, Bussien et
173 al., 2008). It includes two main magmatic facies (equigranular RG₁ and porphyritic RG₂) both
174 composed of $\text{Qz} + \text{Kfs} + \text{Pl} + \text{Bt} \pm \text{Wm} \pm \text{Grt} \pm \text{Ep} \pm \text{Chl} \pm \text{Zr} \pm \text{Spn} \pm \text{Cal} \pm \text{Py}$ (Rast et al.,
175 2022, mineral abbreviations from Whitney & Evans, 2010; Wm: white mica). RG₁ and RG₂
176 facies only differ by mineral proportions and the occurrence of a Bt-Kfs foliation in RG₂ (Rast et
177 al., 2022). This meso-scale bulk foliation has been attributed to an Alpine greenschist facies
178 overprint, based on field and microstructural observations (Gapais et al., 1987; Steck, 1976;
179 Steck & Burri, 1971). Another evidence of Alpine greenschist facies metamorphism is the
180 occurrence of atoll-like garnets in the Rotondo granite (Steck, 1976; Steck & Burri, 1971). The
181 peculiar atoll-like shape, and their Ca-rich composition, have been interpreted by Steck & Burri
182 (1971) to reflect two metamorphic growth stages at different temperature and/or fluid activity
183 conditions. However, the textural relationship between the atoll-garnets and the bulk foliation
184 was not addressed in detail. A set of steep, NW-dipping ductile shear zones, with top-to-SE dip-
185 slip reverse kinematics developed during the same Alpine retrograde event (Lützenkirchen &
186 Loew, 2011). The ductile shear zones have been classified in two main groups (Rast et al., 2022):
187 (i) granitic shear zones, composed of fine-grained mylonite with feldspar augens in a biotite-
188 bearing foliation; and (ii) quartz-biotite-rich shear zones, characterized by the occurrence of
189 sigmoidal quartz veins with rigid cm-sized calcite clasts. Ductile shear zones were exploited as
190 nucleation sites for late brittle faulting at upper crustal levels, as inferred from the stability of
191 syn- to post-kinematic zeolite minerals, and the formation of clay-rich gouges (Lützenkirchen &
192 Loew, 2011). Despite the general understanding of the regional and local scale tectonic
193 evolution, a detailed and holistic description of the structural and tectonometamorphic features,
194 and absolute timing of deformation events in this area are still missing.



195
 196 **Figure 1:** Geological setting of the study area. (a) Tectonic sketch of the Central-Western
 197 Alps (redrawn from Ballèvre et al., 2018, Schmid et al., 2004). AA: Aar; AG: Argentera; AR:
 198 Aiguilles rouges; BD: Belledonne; DM: Dora Maira; GP: Gran Paradiso; GT: Gotthard; IVZ:
 199 Ivrea-Verbano Zone; LD: Lepontine Dome; MB: Mont Blanc; MR: Monte Rosa; PE: Pelvoux.
 200 (b) Tectonic sketch of the Central-Western Gotthard massif showing the spatial distribution of
 201 the meta-granitoid intrusion (Rotondo, Fiabba, Gamsboden). (c) Geological section across the
 202 Central Swiss Alps.

203 **3 Material and Methods**

204 **3.1. Field structural analysis**

205 This work further extends the previous work of Lützenkirchen & Loew (2011) and Rast
 206 et al. (2022), improving the detail of structural description, and adding absolute age constraints
 207 on the deformation structures, with implications on regional tectonic and rheological evolution. It
 208 provides a detailed description of the structural evolution and inventory of the deformation
 209 structures affecting the rock massif hosting the Bedretto Underground Laboratory for

210 Geosciences and Geoenergies (BULGG; Ma et al., 2022). Field survey was focused on the
211 analyses of deformation features and the collection of structural data at 205 structural stations
212 (“Waypoints” – WP in Fig. 2a), resulting in a georeferenced dataset of 473 structural
213 measurements, each of which includes a structural description, orientation of shear plane
214 (Dip/Dip direction) and lineation (Trend/Plunge), kinematics, mineralogy, deformation fabric
215 (brittle vs. ductile), thickness, length, and throw. These structures were then subdivided into sets
216 based on kinematic compatibility, mineralogy, and texture. Oriented samples were collected for
217 further microstructural and petrochronological analysis. The geographic coordinates of relevant
218 waypoints are reported in the Supplementary Information (SI) Table S1. The Structural dataset is
219 available in the SI Dataset DS1

220 3.2. Optical/Scanning Electron Microscopy and Electron Probe Micro Analyses

221 Thin sections were cut parallel to the lineation direction (X kinematic direction) and
222 perpendicular to the foliation plane (XY kinematic plane). Backscattered electron (BSE) images
223 and Energy Dispersion Spectrometry (EDS) mapping were performed at ScopeM (ETH) with a
224 Hitachi SU5000 Scanning Electron Microscope (SEM). Quantitative compositional analyses
225 were performed at the Institute for Geochemistry and Petrology (ETH) with a JEOL JXA-8230
226 Electron Probe Microanalyzer equipped with five Wavelength Dispersion Spectrometers (WDS).
227 Further details on analytical conditions are reported in the SI Text S1. Mineral compositions are
228 reported in the SI Table S2.

229 3.3. P-T pseudosection calculation

230 The bulk rock compositions adopted for pseudosection calculation were obtained by X-
231 Ray Fluorescence spectroscopy at the Institute for Geochemistry and Petrology (ETH) with a
232 WD-XRF PANalytical AXIOS equipped with five diffraction crystals (bulk compositions are
233 reported in the SI Table S3). Pressure-temperature pseudosection calculations were performed
234 with *Perple_X* 6.9.1 (Connolly, 2005) adopting the thermodynamic database of pure end-
235 members from Holland & Powell, (2011; *hp62ver.dat*). Adopted solid solution models and
236 computational details are reported in the SI Text S1. The chemical system used for the
237 calculation is MnO-Na₂O-CaO-K₂O-FeO-MgO-Al₂O₃-SiO₂-H₂O-TiO₂-Fe₂O₃
238 (MNCKFMASHTO). In the text, the term “observed” refers to the paragenesis observed in thin
239 section and to the phase chemistry obtained from EPMA analyses; the term “computed” refers to
240 the chemistry and mineral paragenesis calculated by pseudosection computations. Results of
241 pseudosections and related files are available in the SI Dataset DS2.

242 3.4. In-situ LA-ICP-MS U-Pb & Trace Element analyses

243 In-situ Garnet U-Pb dating, and trace element analyses were performed on polished thin
244 sections by laser ablation-inductively coupled plasma-mass spectrometry (LA-ICP-MS) at the
245 ERDW department of ETH Zurich using an ASI RESOLUTION S-155 excimer (ArF, 193 nm) laser
246 ablation system coupled to a Thermo Scientific Element XR sector-field ICP-MS (Guillong et
247 al., 2014). Instrumentation and data acquisition parameters for U-Pb dating are summarized in SI
248 Dataset DS3 reporting standards of Horstwood et al. (2016). All data from the session, including
249 details on the data reduction strategies and results of validation reference materials can be found
250 in SI Dataset DS3.

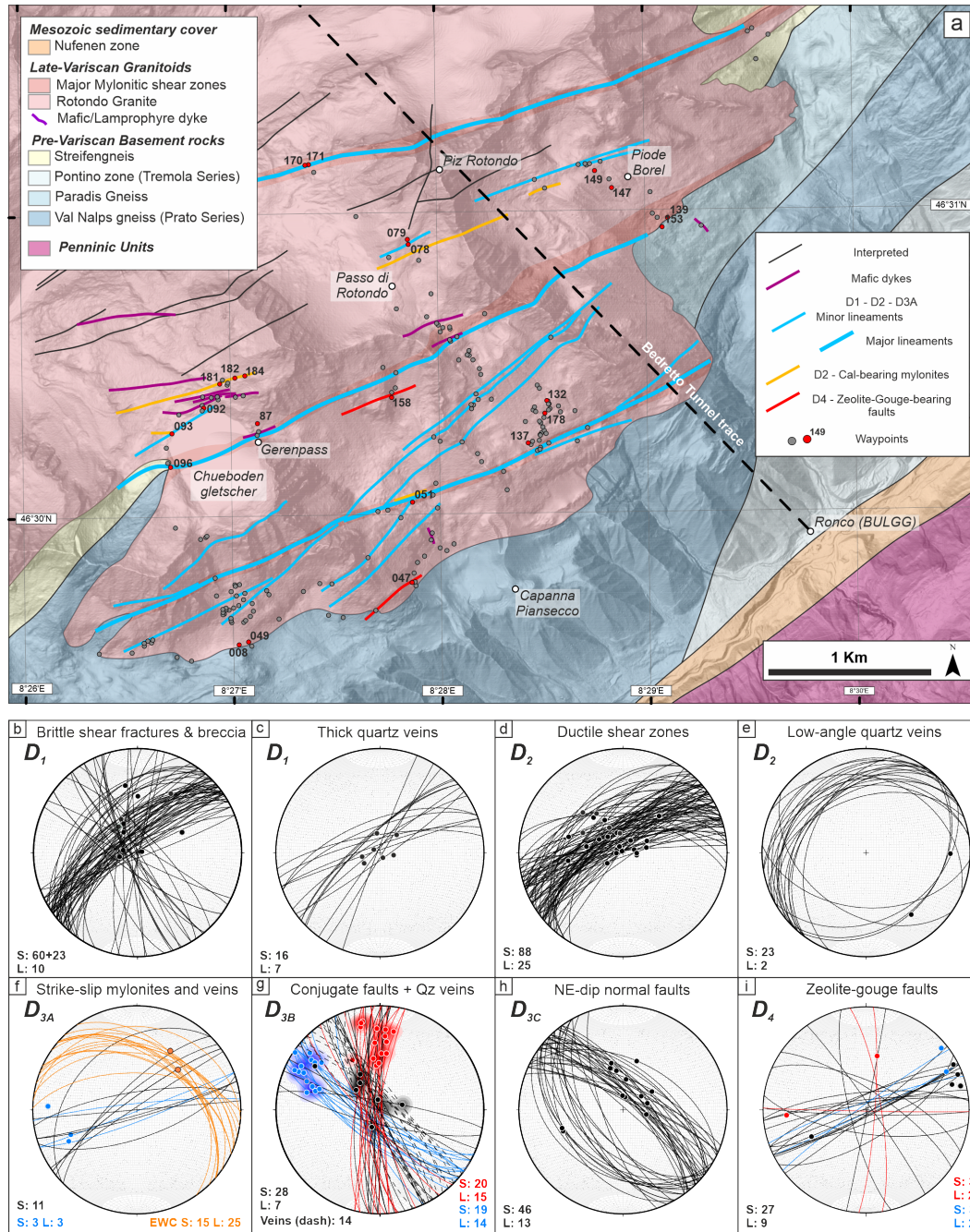
251 3.5. In-situ LA-ICP-MS Rb-Sr analyses

252 In situ Rb-Sr isotope analyses of mica in thin section were undertaken using an ASI
253 RESolution 193 nm excimer laser probe interfaced to an Agilent 8800 ICP-MS/MS at ETH
254 Zurich following the procedure outlined in Giuliani et al. (2023). This method employs an
255 isochronous in-house mica reference material from the Wimbledon lamproite (Sarkar et al.,
256 2023) to calibrate the Rb/Sr fractionation in mica unknowns following initial calibration of
257 $^{87}\text{Sr}/^{86}\text{Sr}$ and $^{87}\text{Rb}/^{86}\text{Sr}$ using the silicate glass reference material NIST 610. This method is
258 validated by analyses of micas from the Bultfontein kimberlite with ages independently
259 constrained by isotope-dilution Rb-Sr dating (Fitzpayne et al., 2020). All the details pertaining
260 analytical conditions, reference materials and data processing can be found in the SI Text S1.
261 The Rb-Sr age data are summarized in Table 1 and all the Rb-Sr analyses can be found in SI
262 Dataset DS4.

263 **4. Results**

264 4.1 Field observations – Sequence of localized deformation structures

265 In the following, we describe the sequence of subsolidus deformation structures,
266 numbered following their relative chronology (from the oldest D₁, to the youngest D₄), as
267 inferred from field analyses of crosscutting and overprinting relationships, mineralogy, texture,
268 and kinematics. Structural data are summarized in Fig. 2b-i. Field images of the described
269 structure sets are reported in Figs. 3-4-5. In the SI Text S2, additional data about the magmatic
270 structures (aplitic and mafic dykes), and the tectonometamorphic evolution of the RG-host rocks
271 are presented.



272

273 **Figure 2.** Structural map and data of the surveyed area in the Rotondo granite. (a)
 274 Structural field map of the southern rim of the Rotondo Granite summarizing the field
 275 observations and showing the location of investigated areas (modified after Berger et al., 2017).
 276 (b-i) Equal area, lower-hemisphere stereographic projections of the structural data for each set of
 277 deformation structures. Great circles: slip planes (S); Dots and contour: lineations (L). Blue and
 278 red planes and dots represent dextral and sinistral kinematics, respectively. Contours are
 279 calculated as Area percentage, minimum contour is 5 area% - computed with Stereonet 11
 280 (<https://www.rickallmendinger.net/stereonet>). (b) D₁ shear fractures, cataclasites and breccias;

281 (c) D₁ plane-parallel thick quartz veins; (d) D₂ ductile shear zones, dip-slip, top-to-SE reverse
 282 kinematics; (e) low-angle quartz veins kinematically related to D₂ shear zones; (f) D_{3A} ductile
 283 shear zones (black great circles) showing strike-slip reactivation and associated extensional wing
 284 cracks (EWC) and quartz-veins developed in dilational jogs (orange great circles); (g) D_{3B}
 285 conjugate, brittle-ductile shear zones (solid great circles) and extensional veins (dashed great
 286 circles); (h) D_{3C} normal faults; (i) D₄ Zeolite- and gouge-bearing brittle fault zones.

287 4.1.1. D₁ brittle shear fractures, cataclasites and breccias

288 The D₁ set consists of brittle shear fractures (Fig 3a), cataclasites (Fig. 3b) and breccias
 289 (Fig. 3c-d) containing a dark, fine-grained matrix that surrounds angular clasts of undeformed
 290 granite (Fig. 3c-d). Milky quartz veins are common along these structures, ranging in thickness
 291 from a few mm (Fig. 3e), to >1 m (Fig. 3e-f), and showing mutual overprinting relationship with
 292 the dark fine-grained matrix (Fig. 3e-h). In some cases, large breccia bodies are observed,
 293 characterized by a transitional texture from crackle-breccias to fine grained cataclasites. A
 294 peculiar feature of D₁ structures is the occurrence of mm-size garnets overgrowing the dark
 295 matrix (Fig. 3b,c,d,g). D₁ structures are steeply dipping, SE-verging, and ENE-WSW-striking
 296 (Fig. 2b-c). A subset of D₁ cataclasites (23 planar measurements) presents an orientation at high
 297 angle to the main set (Fig. 2b). The kinematics of set D₁ structures is rather difficult to constrain,
 298 given that they are overprinted by the following stage of ductile deformation. A dip-slip lineation
 299 L₁ is observed on the exposed surface of the matrix (Fig. 3g), and incipient breccias and shear
 300 fractures commonly show either strike-slip dextral or normal-sense displacement of crosscut
 301 markers in the present orientation (Fig. 3h). Garnet is only observed in D₁ structures not heavily
 302 overprinted by the ductile deformation related to D₂ shear zones (Fig. 3b-c).

303 4.1.2. D₂ Dip-slip, reverse ductile shear zones

304 The D₂ set consists of mylonitic ductile shear zones. D₂ shear zones exploit as nucleation
 305 site the pre-existing structural and/or compositional heterogeneities in the host Rotondo granite,
 306 such as aplitic and mafic dykes, veins, and D₁ structures (Fig. 4). Deformed aplitic and mafic
 307 dykes develop an oblique homogeneous foliation abruptly terminating at the dyke selvage
 308 against the undeformed host RG. D₂ shear zones exploiting D₁ brittle structures preserve the
 309 geometric and textural complexity of the precursor, developing an heterogeneous Bt-Wm-
 310 bearing foliation wrapping around low-strain granite clasts and lithons (Fig. 4b). D₂ structures
 311 strike ENE-WSW, showing a dip-slip, L₂ Bt-Wm-bearing lineation (Fig. 2d). The dominant
 312 kinematics is reverse, top-to-SE, even though dip-slip normal kinematics are observed on rare
 313 SE-steeply-dipping shear planes. Overall, the D₂ ductile shear zones form a large-scale network
 314 defined by subparallel zones of high strain surrounding high-aspect-ratio lozenges of
 315 undeformed granite (Gapais et al., 1987). Sheared quartz + calcite veins are common in high
 316 strain D₂ ductile shear zones (Fig. 4a; see also Fig. 11 of Rast et al. 2022). Locally, calcite-rich
 317 shear zones are observed, showing thick homogeneous calcite-rich layers close to layers clearly
 318 resembling sheared calcite-bearing breccias (Fig. 4d). A set of shallowly NW-dipping quartz +
 319 feldspar veins and non-mineralized joints also occur (Figs. 2e, 4b), and commonly abut major
 320 mylonitic shear zones, with vein tips dragged into the main mylonitic foliation (Fig. 4b).

321 4.1.3. D₃. Strike-slip, brittle-ductile shear zones

322 D₃ structures include: (i) D_{3A}, strike-slip mylonitic shear zones reactivating pre-existent
 323 D₁-D₂ structures; (ii) D_{3B}, a set of conjugate, brittle-ductile strike-slip faults; (iii) D_{3C}, a set of

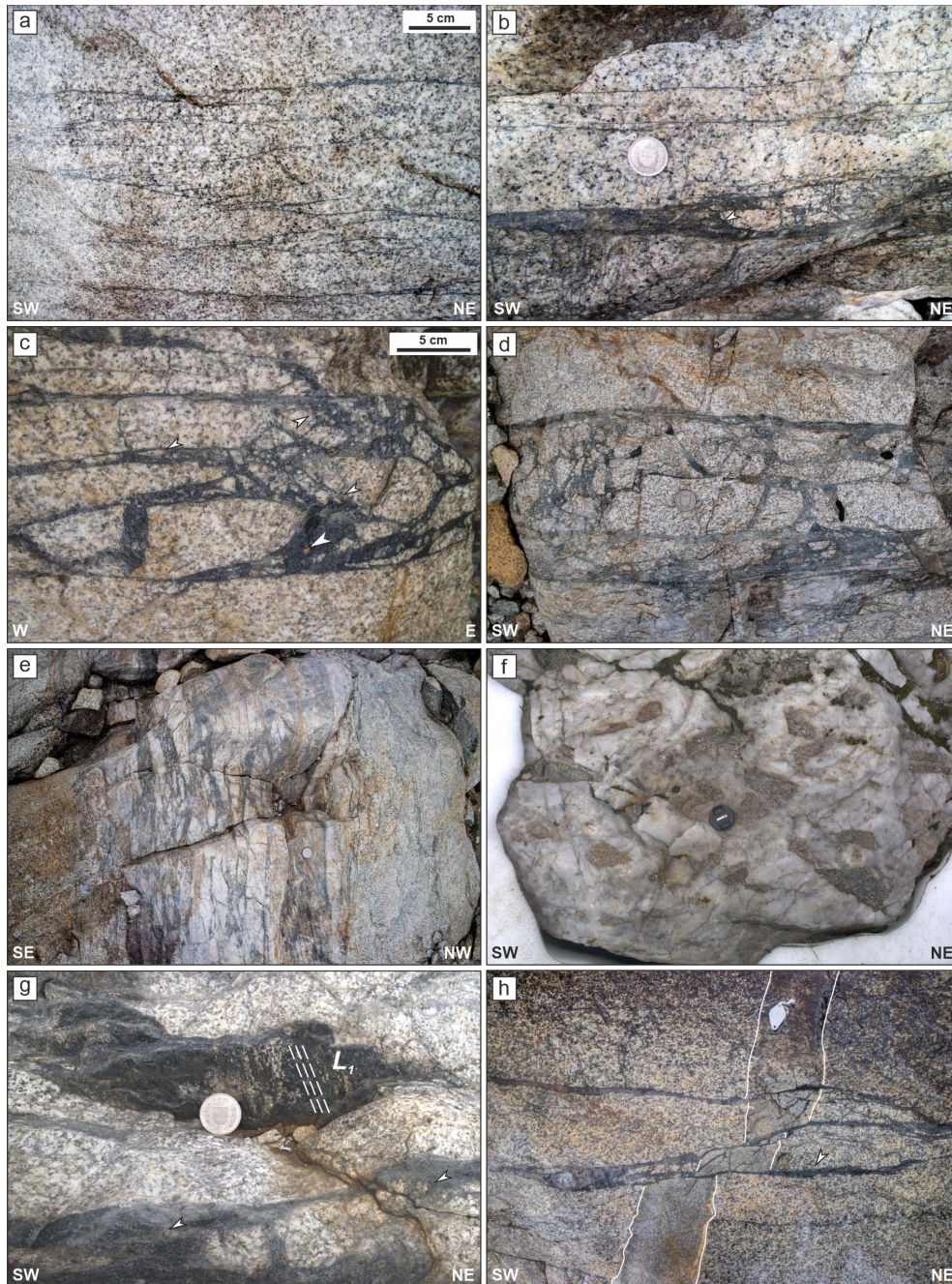
324 conjugate, normal dip-slip faults. D₁-D₂ structures are reactivated under brittle-ductile conditions
 325 with a dominant strike-slip kinematics (Fig. 4e-h), as inferred from the development of a sub-
 326 horizontal L_{3A} lineation overprinting the pre-existing dip-slip L₂ (Fig. 4e). The orientation of D_{3A}
 327 structures reflects the pre-existent ENE-WSW mylonitic shear zones (Fig. 2f). A heterogeneous
 328 S-C fabric is developed in major mylonitic zones, showing dominant dextral kinematics (Fig. 4e-
 329 f, same outcrop of the shear zone a few meters far from Fig. 4a). Tensile wing cracks (Figs. 4g,
 330 2f), brecciated dilational jogs (Fig. 4h), and quartz + feldspar veins develop at high angle to D₁-
 331 D₂ shear fractures and mylonites during re-shearing under strike-slip orientations. These veins
 332 and dilational breccias can be distinguished from previous D₁ quartz-veins and breccias based on
 333 their orientation and their content of coarse quartz clear crystals.

334 The D_{3B} structures consist of brittle-ductile discrete faults and mylonites, arranged in
 335 conjugate sets (Fig. 5a). N-S-striking set of sinistral, strike-slip fault planes is conjugated to a
 336 WNW-ESE-striking set of dextral strike-slip fault planes (Fig. 2g). In both cases, the L_{3B}
 337 lineation is oblique (Fig. 2g), shallowly plunging toward ENE or WNW, respectively. The
 338 conjugate fault sets crop out in low-strain domains bounded by major D_{3A} shear zones. A very
 339 localized mylonitic foliation is observed along the discrete fault planes. The conjugate set of
 340 brittle-ductile faults is associated with subvertical, NW-SE-striking tensional Qz + Chl + Wm +
 341 Py + Hem veins (Fig. 5a). Such mineralization and veins are observed also in extensional jogs
 342 between overlapping en-echelon fault segments (Fig. 5a). Episyenites (i.e., quartz-depleted,
 343 vuggy altered granites) are observed close to mineralized veins and shearing planes
 344 (Pennacchioni et al., 2016).

345 D_{3C} structures consist of NW-SE striking faults with a dip-slip, Qz + Wm-bearing L_{3C}
 346 lineation with normal kinematics (Figs. 5b, 2h). They occur as discrete shear planes, with a near-
 347 constant spacing on the m-scale (Fig. 5b). They crop out mainly in the southern part of the RG,
 348 and they are less developed elsewhere. The dominant set of shear planes dips NE, with a pure
 349 dip-slip L_{3C} lineation. Conjugate, SW-dipping shear planes with normal kinematics also occur. In
 350 some cases, the shear plane is also characterized by a weak ductile foliation in the host rock. D_{3C}
 351 shows mutual crosscutting relationships with D_{3B} structures.

352 4.1.4. D₄ Zeolite- and gouge-bearing brittle faults

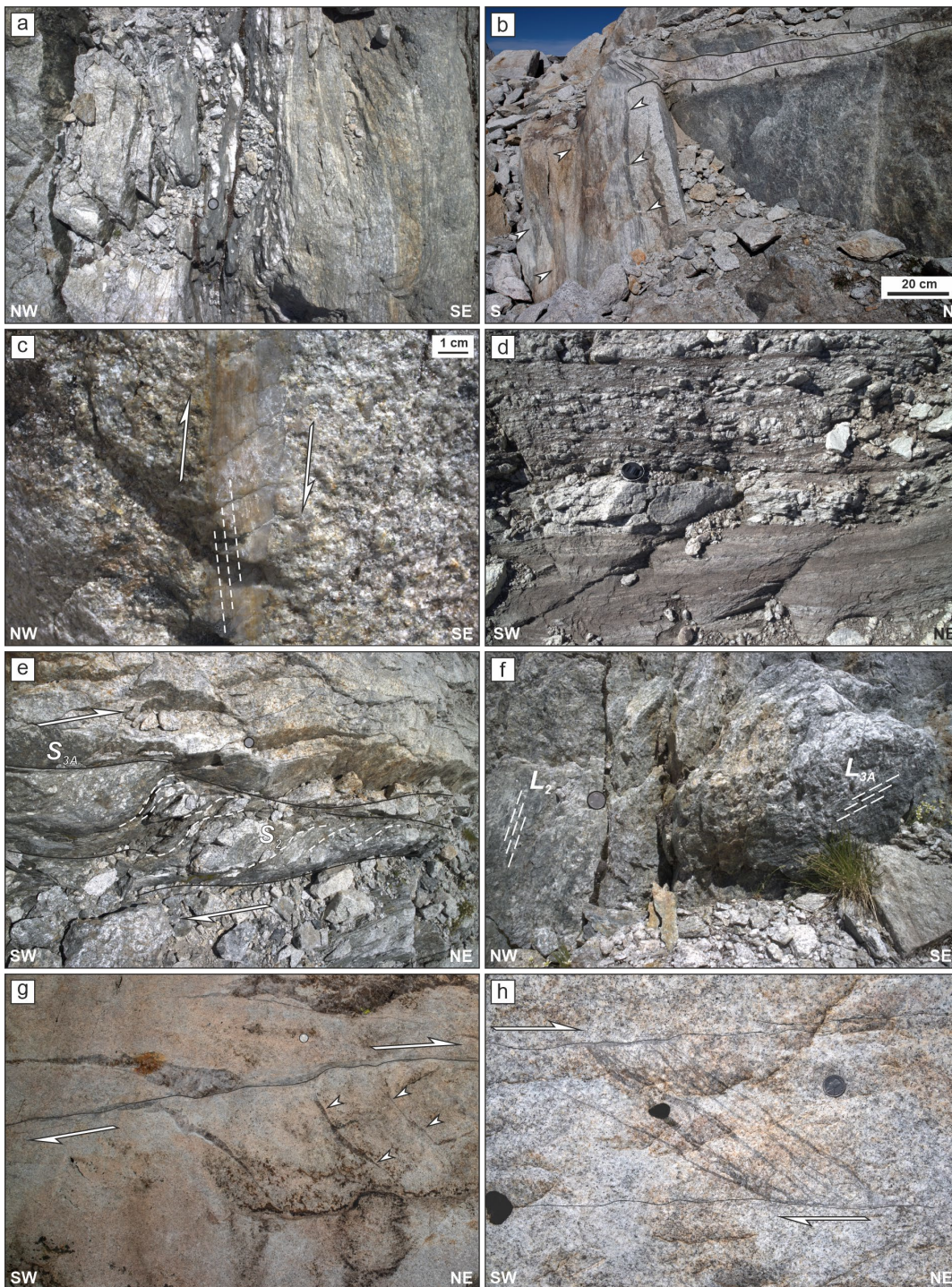
353 The latest set of deformation structures D₄ includes zeolite- and gouge-bearing brittle
 354 faults (Fig. 5c-d). They form gullies and valleys in the topography of the RG, and thus their
 355 exposure is very limited and, when present, badly preserved. When observed, the L₄ lineation is
 356 subhorizontal, consistent with a dominant dextral kinematics inferred from the few planes
 357 showing offset markers (Fig. 2i). Zeolite-bearing, fine-grained breccias are observed on
 358 anastomosing planes exploiting pre-existent D₁ shear fractures. Gouge-bearing fault zones are
 359 observed to develop at the contact between major quartzo-feldspathic mylonites and the
 360 undeformed granite (Fig. 5c-d). D₄ structures exploit pre-existent structural discontinuities, and
 361 the structural data in Fig. 2i show that D₄ structures actually reactivate and exploit the entire set
 362 of pre-existent structures.



363 **Figure 3.** D₁ structures. Note that D₁ brittle structures contain clast and lithons only of
 364 undeformed granite. White arrow points to garnet in the matrix. (a) Set of quartz-biotite-bearing
 365 shear fractures showing en-echelon spatial arrangement (Wp004). (b) A cataclasite, showing
 366 limited ductile reactivation and preserving angular clasts of undeformed granite (Wp078). (c-d)
 367 Example of breccias (outcrop of sample ACB35; Wp149). (e) Sheared breccia showing moderate
 368 ductile reactivation and sheared clasts (resulting from the reworking of a thick quartz vein
 369 (Wp149). (f) Thick, plane-parallel quartz vein preserving breccia structures and undeformed
 370 granite clasts (Wp051). (g) Example of lineated surfaces in the breccia matrix (Wp149). (h)

371 Cataclasites displacing with dextral (and normal) strike-slip kinematics a subvertical pegmatitic-
372 aplitic dyke. Handlens (3 cm) for scale.

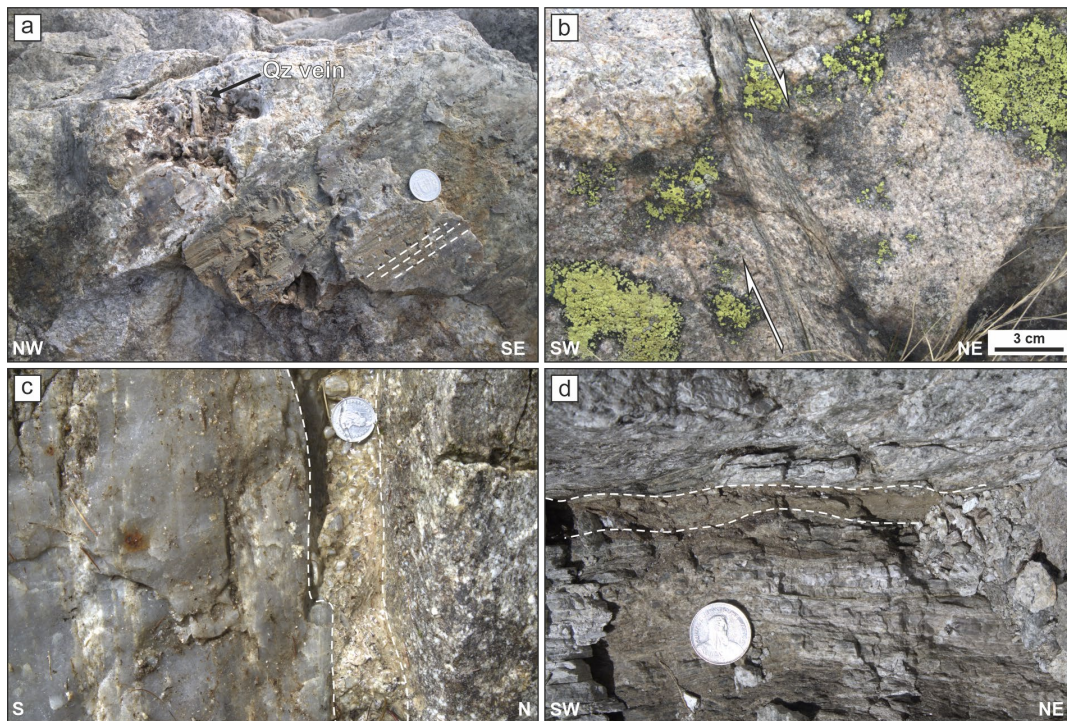
373



374

375 **Figure 4.** D₂-D₃ structures. (a) Dip-slip D₂ shear zone localized on a mafic dyke, parallel
376 to a set of D₁ shear fractures (left hand side of the image) and characterized by the pervasive

377 occurrence of sheared quartz + calcite veins. (Wp170). (b) Heterogeneous D₂ ductile shear zone
 378 (foliation marked by white arrows) with reverse kinematics and the associated low-angle Qz-vein
 379 (black arrows) (Wp087). (c) Sheared D₂ quartz + feldspar vein showing homogeneous internal
 380 foliation, suggesting top-to-SE reverse kinematics (Wp020). (d) D₂ calcite-bearing mylonite
 381 showing the boundary between a homogeneous calcite-mylonite (bottom) and a sheared breccia
 382 (top) with granitoid clasts (Wp182). (e) D_{3A} mylonitic shear zone showing S-C fabric related to
 383 strike-slip reactivation of a former dip-slip D₂ ductile shear zone (Wp171). (f) Detail of the D_{3A}
 384 shear zone reported in (e) showing the occurrence of the L_{3A}, strike-slip lineation and the L₂-dip-
 385 slip lineation on adjacent shear planes; L_{3A} lineation occurs on S-C planes of the mylonitic shear
 386 zone wrapping around lensoid domains where L₂ is still preserved. (g) D_{3A} shear fractures,
 387 showing the development of quartz + feldspar wing cracks suggesting dextral strike-slip
 388 reactivation (Wp178). (h) D_{3A} brecciated dilational jog between two reactivated D₁ shear
 389 fractures (Wp137).



390

391 **Figure 5.** D₃-D₄ structures. (a) D_{3B} shear plane of a sinistral brittle-ductile fault, showing
 392 the oblique L_{3B} lineation and the occurrence of mineralized jogs (quartz vein) (Wp092). (b) D_{3C}
 393 brittle-ductile normal fault characterized by cm-scale heterogeneous foliation along the shear
 394 plane. (c) D₄ zeolite-bearing cataclasite (delimited by dashed white curves) localized at the
 395 contact between a major quartzo-feldspathic D₂ mylonite (left-hand side of the picture) and the
 396 undeformed granite (right-hand side of the picture, Wp047). (d) D₄ gouge-bearing fault localized
 397 on D₂ mylonitic foliation (Wp158).

398

399

400 4.2 Microstructures & petrochronology

401 We report here the results of microstructural, chemical and petrochronological
 402 characterization of representative samples from three of the four classes of deformation
 403 structures, including: (i) ACB35, D₁ brittle breccia (Fig. 3d-e); (ii) ACB27a, major dip-slip D₂
 404 ductile shear zone with tip-to-SE kinematics; (iii) ACB37b, D_{3A} brittle-ductile shear zones with
 405 dextral strike-slip reactivation (Fig. 4f). Microstructure and petrography are presented together
 406 with the mineral composition obtained from EPMA. Representative mineral compositions,
 407 diagrams, and bulk rock chemical compositions are reported in the SI Tables S2-S3, and in SI
 408 Fig. S3.

409 4.2.1. Microstructures, mineral paragenesis and pseudosection calculations

410 4.2.1.1. D₁ Qz-Bt-bearing breccia

411 D₁ breccias are composed of cm-size angular granite clasts, weakly flattened and
 412 sheared, embedded in a fine-grained matrix showing homogeneous grain size and a weak
 413 pervasive foliation defined by Bt (Fig. 6b). The matrix mineral paragenesis in ACB35 includes
 414 Qz + Bt (Mg# = 0.40-0.45; Ti = 0.02 apfu) + Kfs + Grt + Ep/Aln + Ab ± Pl ± Wm ± Chl + Ap +
 415 Zrc + Nb-Y-REE oxides and silicates (Gadolinite group). Rare Mnz grains are observed scattered
 416 in the recrystallized matrix. Grt crystals range from 100 μm to 5-10 mm, showing a wide range
 417 of crystal morphologies, from euhedral grains containing angular inclusions (Fig. 6a), to grains
 418 showing anhedral shapes, resorbed rims, and poikiloblastic/honeycomb textures (Fig 6b). In most
 419 samples of pristine D₁ breccia, euhedral Grt includes a random pattern of Qz + Pl + Kfs angular
 420 inclusions with no shape preferred orientation (Fig. 6a). These inclusions are only preserved
 421 within euhedral garnets and are here interpreted to reflect the fine-grained cataclastic matrix of
 422 the D₁ breccia on which Grt grew. There is no evidence of Grt growth and shearing coeval with
 423 D₁ brecciation. Grt grains containing angular inclusions are typically enveloped by a weak
 424 mylonitic foliation overprinting the breccia matrix (Fig. 6a-b). In some cases, Grt is weakly
 425 pleochroic, suggesting a non-cubic crystal symmetry (e.g., Cesare et al., 2019). The Grt in
 426 sample ACB35 shows an elongated shape, parallel to the foliation, with an honeycomb texture,
 427 characterized by a heterogeneous distribution of oriented inclusions (Fig. 6b). The inclusions are
 428 mainly euhedral Ep and Aln with a peculiar texture (Fig. 6c-d). Aln is observed at the core,
 429 surrounded by Ep forming the euhedral rim (Fig. 6d). Ep in the recrystallized breccia matrix
 430 shows a concentric, rhythmic zoning with brighter rims, without Aln cores (Fig. 6e-f). Ep
 431 aggregates in the recrystallized matrix contain spongy Zrc crystals, and partially destabilized
 432 Thorite-Xenotime at their core (Fig. 6f).

433 Grt compositional variability in this structural domain ranges from Alm₃₆Sps₃₀Grs₃₂Prp₂
 434 (Grt_A) to Alm₃₆Sps₂₆Grs₃₆Prp₂ (Grt_B), describing a smooth gradient from the inclusion-free layer
 435 (Grt_A in Fig. 6c) toward the outer, inclusion-rich rims with honeycomb microstructure (Grt_B in
 436 Fig. 6c).

437 Garnets with similar compositions are also observed in sheared D₁ shear fractures and
 438 veins (samples ACB_Sp3d and ACB18, Alm₃₄₋₄₁Sps₂₆₋₁₈Grs₃₈₋₃₉Prp₁; Fig. 6b; SI Fig. S2a). Grt in
 439 ACB35 shows resorbed rims and embayment at the contact with the sheared granular matrix and
 440 phyllosilicates, indicating that Grt is likely metastable in the sheared mineral paragenesis (Fig.
 441 6b-d).

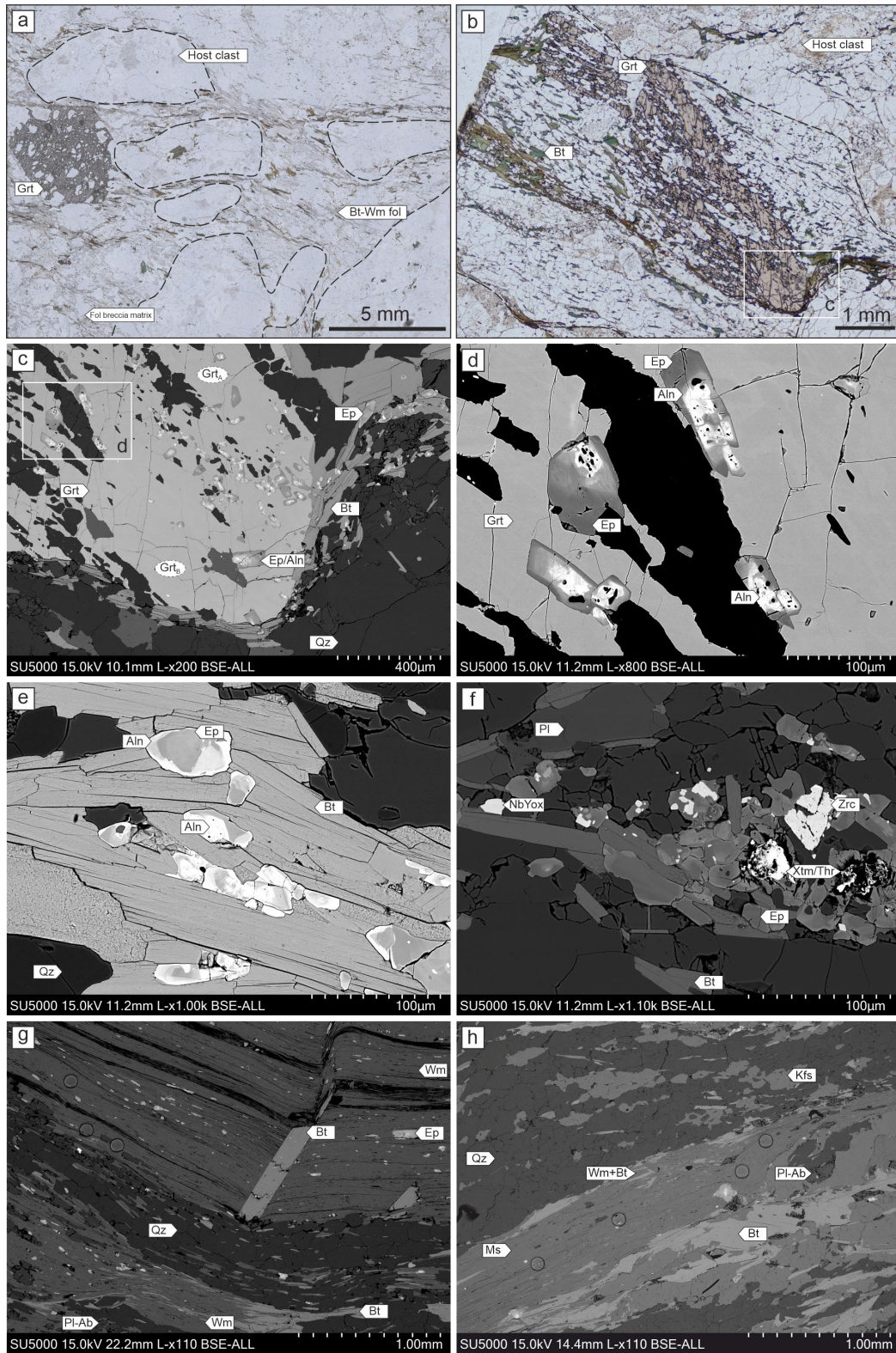
442 The pseudosection for sample ACB35 was computed with an H₂O amount equal to the
 443 LOI content retrieved from XRF analyses (SI Table S2; Fig. 7a). The bulk composition adopted
 444 for the calculation reflects the recrystallized matrix of the breccia. Its composition is highly
 445 enriched in SiO₂ compared to the undeformed granite (SI Table S3). The observed paragenesis
 446 Qz + Bt + Kfs + Grt + Ep + Ab is computed to be stable over a wide range of *P-T* conditions (*T*
 447 < ~550 °C, *P* < 0.9 GPa). The variation of computed Bt composition is limited and not useful to
 448 further constrain *P-T* conditions of apparent equilibrium. The observed Grt_A and Grt_B
 449 compositions are computed to be stable at *T* = 590 ± 10 °C, and *P* = 0.94 GPa for Grt_A, *P* = 1.02
 450 GPa for Grt_B. However, under those conditions, Ep and Ab are not stable. This misfit between
 451 observed and computed paragenesis suggests that the observed paragenesis might be metastable,
 452 preserving a porphyroclastic Grt in a recrystallized and equilibrated fine-grained matrix. In any
 453 case, similar *P-T* estimates are retrieved from pseudosection calculations using samples ACB18
 454 (590 ± 25 °C, 1.0 ± 0.1 GPa), as well as ACB25 (575 ± 15 °C, 0.9 ± 0.1 GPa), the latter
 455 representing the seared contact between granite and the host rock (SI Text S2-S3).

456 4.2.1.2. D₂ Dip-slip, reverse shear zones

457 The sample ACB27a represents a high-strain domain of a D₂ ductile shear zone. D₂
 458 ductile shear zones are characterized by a pervasive and homogeneous mylonitic foliation
 459 including Qz + Kfs + Wm (Si = 6.6-6.8) + Ep/Aln + Bt (Mg# = 0.55; Ti = 0.04 apfu) + Ab ± Pl
 460 enveloping mm-sized Wm + Bt porphyroblasts (Fig. 6g). The pseudosection was computed
 461 adopting an H₂O amount as obtained from the LOI content retrieved from XRF analyses (Fig.
 462 8a). The observed paragenesis Qz + Bt + Wm + Kfs + Ep + Ab is computed to be stable over a
 463 wide range of *P-T* conditions, at H₂O-saturated conditions. Computed Wm(Si) is comparable to
 464 the observed composition. Considering the observed Wm(Si), Bt(Ti) = 0.03 and Bt(Mg#) > 0.5,
 465 the stability field of the observed paragenesis is constrained to *T* = 520 ± 40 °C and *P* = 0.83
 466 ± 1.25 GPa.

467 4.2.1.3. D₃ Strike-slip, dextral shear zones

468 The ACB37b mineral paragenesis includes Qz + Kfs + Wm + Bt (Mg# = 0.58; Ti = 0.05
 469 apfu) + Pl + Ab + Ep/Aln + Ap ± Chl (Fig. 6h). The main foliation is defined by anastomosing
 470 S-C shear planes of fine-grained Wm, incorporating Bt and Ep/Aln inclusions, wrapping around
 471 recrystallized Qz + Pl + Ab + Kfs lenses. Wm(Si) is rather variable, forming two main
 472 compositional groups which have no microstructural correspondence: Wm(Si)₁ = 6.40 apfu and
 473 Wm(Si)₂ = 6.65-6.85 (SI Fig. S3a-b). The pseudosection has been computed at H₂O-saturated
 474 conditions (Fig. 8b). The observed paragenesis is stable over a wide range of *P-T* conditions.
 475 Computed Wm(Si)₁, and Bt(Ti) isopleths define a field centered at *T* = 395 ± 25 °C and *P* =
 476 0.4 ± 0.1 GPa. The variability of the computed Bt(Mg#) is rather limited (0.52-0.55) and slightly
 477 underestimates the observed composition. Spn is predicted in very small amounts (>1 vol%) but
 478 not observed.



479

480 **Figure 6.** Microstructures of the analyzed deformation zones. (a) Optical plane-polarized
 481 light micrograph of D₁ breccias. Note the occurrence of the random pattern of inclusions in Grt
 482 formed by angular clasts. Dashed curves delimit mm-to-cm clasts of the host granite. (b) Optical

483 plane-polarized light micrograph of the recrystallized matrix of a D₁ breccia (sample ACB35),
 484 showing the analyzed honeycomb Grt. (c) BSE image of Grt in sample ACB35 showing the
 485 alignment of Ep/Aln inclusions. See text for explanations. (d) BSE image of the Ep/Aln
 486 inclusions in the Grt of sample ACB35, showing the Aln, inclusion-rich cores with resorption
 487 textures and euhedral Ep rims. (e) BSE image of Ep crystals included in Bt in the fine-grained
 488 matrix of sample ACB35, showing rhythmic zoning between Ep-rich and Aln-rich layers. (f)
 489 BSE image of Ep aggregates along the mylonitic foliation in sample ACB35, including Zircon
 490 (Zrc), Nb-Y-oxides (NbYox), and Xtm/Thr aggregates likely resulting from the destabilization of
 491 Monazite. (g) BSE image of sample ACB27a showing the Wm porphyroblast and mylonitic
 492 foliation. Note the craters due to laser ablation analyses. (h) BSE image of the mylonitic foliation
 493 of sample ACB37b showing the occurrence of fine-grained aggregates of Wm + Bt. Note the
 494 craters due to laser ablation analyses.

495 4.2.2. In-situ U-Pb on Garnet

496 We report here the results of U-Pb and trace element analyses from a set of samples
 497 representing D₁ breccias (ACB35; ACB_Sp8; ACB_Sp7), and sheared Qz-veins and fractures
 498 (ACB18, ACB_Sp3) (Fig. 6; SI Fig. S2).

499 The analyses of Grt in ACB35 show two distinct populations, defining two separate
 500 trends in a Tera-Wasserburg concordia diagram (Fig. 7b). A first population of U-Pb data forms
 501 a linear array defining a lower intercept age of 128.0 ± 9.3 Ma (n=26, MSWD=2.9). A second
 502 population can be fitted by a regression line with a lower intercept corresponding to an age of
 503 34.0 ± 4.4 Ma (n=25, MSWD=2.8). The combination of U-Pb ratios and trace element
 504 concentrations reveals that the first population contains elevated Zr amounts (up to 7000 ppm),
 505 which are indicative of contamination of the analysis by ablation of zircon inclusions in the
 506 garnet. As shown in the trace element maps of Fig. 7c, some of the ablation spots fall adjacent to
 507 or on top of Grt areas where high amounts of Zr are detected. Therefore, to avoid contamination
 508 artifacts, we have excluded from the final age calculation all the U-Pb data with Zr content >20-
 509 30 ppm (depending on the sample). This approach filters out the anomalously old, spurious U-Pb
 510 intercept age (~128 Ma) defined above.

511 The pooled lower intercept Tera-Wasserburg age obtained from analyses of several small
 512 (inclusion-free) Grt grains for this (ACB35) and the other samples are reported in Table 1. Other
 513 samples range between 26.9 ± 1.3 Ma (n=54, MSWD=1.9) for ACB_Sp3b (Fig. 7e), and $20.1 \pm$
 514 1.0 Ma (n=33, MSWD=0.86) for ACB_Sp8d (Fig. 7f). Additional details of U-Pb analyses,
 515 including Tera-Wasserburg plots, are reported in the SI Text S2 and Fig. S2.

516 The REE patterns of analyzed garnets (Fig. 7d) are characterized by a high variability in
 517 REE contents, ranging between two end members (Grt-Type1 and Grt-Type2 in Fig. 7d inset).
 518 Grt-Type1 is characterized by significant depletion of LREE with a negative anomaly of Ce, and
 519 a steep HREE slope. Grt-Type2 is characterized by a rather flat LREE-HREE profile, along with
 520 a low Sm/La (Fig. 7d). In addition, the ablation maps reveal a weak trace element zoning in Grt
 521 (Fig. 7c). A similar variation in LREE content is also observed in samples ACB18, ACB_Sp3b,
 522 ACB_Sp8c/d, ACB_Sp7d (Fig. 7d).

524 **Figure 7.** *P-T-t* data for sample of D1 structures. (a) Computed pseudosections for
 525 sample ACB35; (b) Tera-Wasserburg (TW) diagram of U-Pb garnet and trace element data for
 526 samples ACB35, showing the two populations of data, with analyses plotted according to their Zr
 527 content. (c) Laser ablation maps for selected isotopic masses, including ^{55}Mn , ^{31}P , ^{90}Zr , ^{139}La ,
 528 ^{172}Yb , ^{238}U , on ACB35 Grt (see area delimited in Fig. 6b). (d) Chondrite-normalized
 529 (McDonough and Sun, 1995) REE-patterns of the analyzed Grt in samples ACB35, ACB18,
 530 ACB_Sp3b, ACB_Sp7c, ACB_Sp8c/d; the inset shows the compositions of the two identified
 531 end-members (Grt-Type1, Grt-Type2) characterized by either flat LREE or steep LREE profile.
 532 (e -f) TW diagram for Grt in ACB_Sp3b and ACB_Sp8d, respectively.

533 4.2.3. In-situ Rb-Sr on white mica and biotite

534 We report here the results of in-situ Rb-Sr analyses of white mica defining the main
 535 foliation in the samples ACB27a, ACB37b, already described before, as well as in an additional
 536 sample ACB12b. Then, Rb-Sr data for biotite in the undeformed granite B19-1417 are presented.

537 4.2.3.1. D₂ Dip-slip, reverse shear zone

538 In ACB27A the mica grains show a large spread in $^{87}\text{Rb}/^{86}\text{Sr}$ from 119 to 3125 with
 539 corresponding variations in $^{87}\text{Sr}/^{86}\text{Sr}$ between 0.82 and 1.42 ($n = 39$). A regression through these
 540 data generates an isochron with a slope corresponding to an age of 18.1 ± 0.9 Ma (2se, $n = 38/39$,
 541 MSWD = 1.5) and a $^{87}\text{Sr}/^{86}\text{Sr}$ intercept of 0.799 ± 0.010 (Fig. 7e).

542 4.2.3.2. D₃ Strike-slip, dextral shear zone

543 The analyses of mica in sample ACB37B provide different age results. Most of the
 544 analyzed grains cluster at $^{87}\text{Rb}/^{86}\text{Sr}$ between 700-1000 with four measurements extending to
 545 higher $^{87}\text{Rb}/^{86}\text{Sr}$ (up to 3030) and one to lower $^{87}\text{Rb}/^{86}\text{Sr}$ (4.1). $^{87}\text{Sr}/^{86}\text{Sr}$ values are similarly
 546 clustered between 0.86 and 0.99 with three higher (up to 1.44) and one lower value (0.77). The
 547 corresponding Rb-Sr isochron provides an age of 14.7 ± 1.5 Ma and an initial $^{87}\text{Sr}/^{86}\text{Sr}$ of 0.767
 548 ± 0.018 ($n = 35$, MSWD = 1.3; Fig. 7f). These values change marginally if the high Sr analysis,
 549 for which contribution by a Sr-bearing phase is likely, is removed (e.g., 13.1 ± 2.1 Ma).

550 4.2.3.3. D₂ bulk foliation in RG₂ granite

551 Sample ACB12b represents the foliated RG₂ granite, where the Wm-bearing bulk
 552 foliation wraps around the porphyric Kfs and the partially recrystallized quartz domains. The
 553 recrystallized matrix along the foliation is mainly composed of Qz + Wm + Ab + Ep. White mica
 554 shows limited $^{87}\text{Rb}/^{86}\text{Sr}$ spread (≤ 352) including two relatively low values of 8.0 due to ablation
 555 of Sr-rich impurities. $^{87}\text{Sr}/^{86}\text{Sr}$ is also limited compared to the previous samples (≤ 0.83) with
 556 $^{87}\text{Sr}/^{86}\text{Sr}$ of 0.73 for the two low-Rb/Sr samples. The age of the Rb-Sr isochron (18.6 ± 1.9 Ma; n
 557 $= 35$; MSWD = 0.76; $^{87}\text{Sr}/^{86}\text{Sr}_i = 0.729 \pm 0.005$) is largely constrained by the two low Rb/Sr
 558 analyses. Exclusion of these two analyses returns a similar although much less precise of $16.3 \pm$
 559 3.7 Ma. For all these samples (ACB27a, ACB37b and ACB12b) we prefer to consider the more
 560 precise isochron ages that include the high-Sr analyses because the high Sr impurities included in
 561 these analyses appear to be sourced from minerals (epidote) cogenetic with mica.

562

4.2.3.4. Undeformed RG₁ granite

563

564

565

566

567

568

Sample B19-1417 represents the undeformed RG₁ granite. Biotite in this undeformed granite provides similar ages to those of white mica in sheared sample ACB37B. This biotite shows very high and highly variable ⁸⁷Rb/⁸⁶Sr (2350-45720) corresponding to elevated ⁸⁷Sr/⁸⁶Sr between 1.22 and 10.5. The large spread in Rb-Sr data point results in a relatively precise isochron corresponding to an age of 15.2 ± 0.7 Ma (n = 28/30; MSWD = 0.34) but a poorly defined ⁸⁷Sr/⁸⁶Sr intercept of 0.68 ± 0.11 (Fig. 8f).

569

570

571

572

Biotite in RG₁ (sample B19-1417), foliated RG₂ (sample ACB14c, SI Text S4, Fig. S4) and D₂ localized shear zone in RG₂ (sample ACB3b, SI Text S4, Fig. S4) yielded indistinguishable ages (Table 1) which are all within uncertainty of the Rb-Sr age of white mica from the D_{3A} localized shear zone (Fig. 8d).

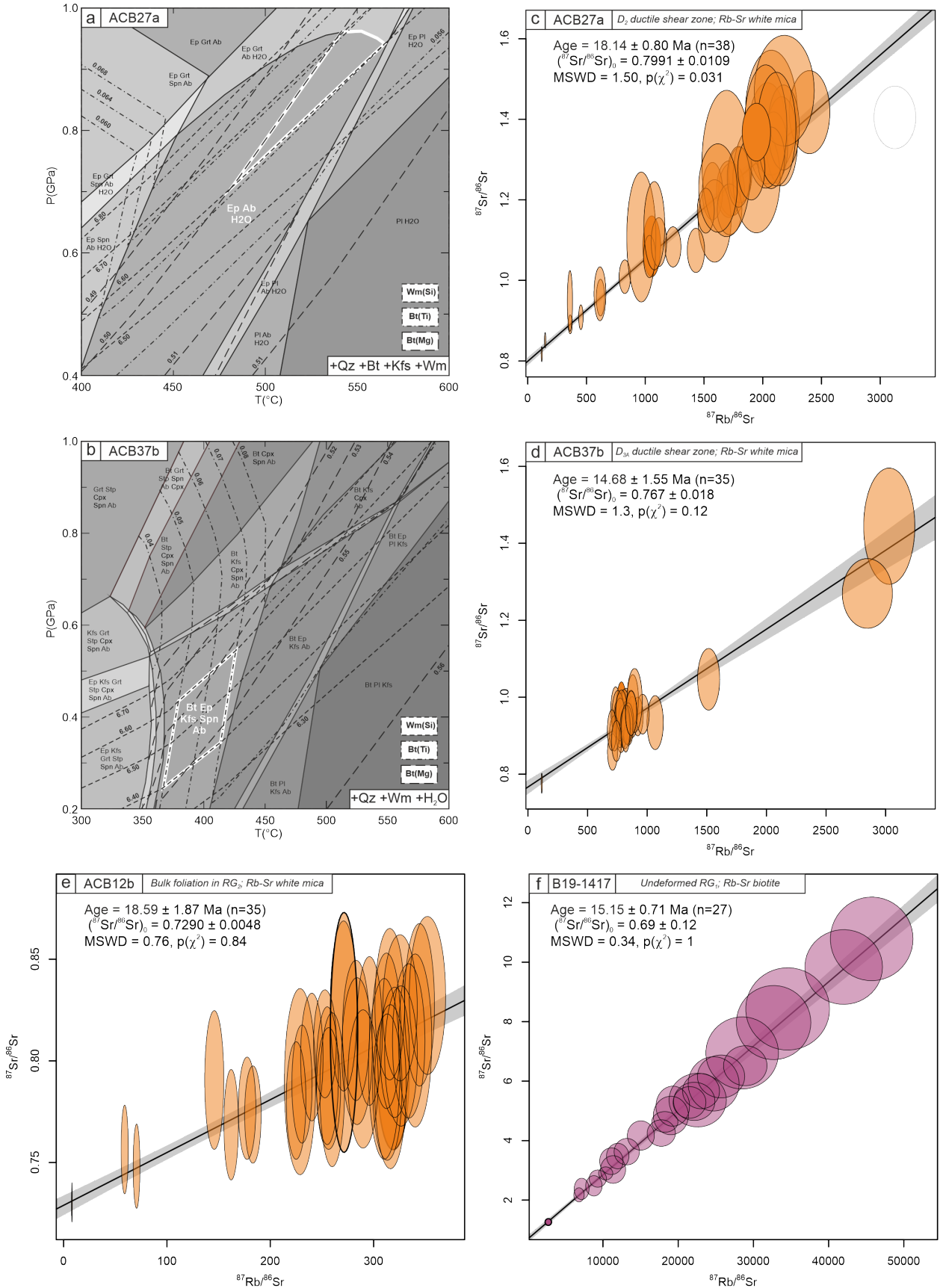
573

574

Sample	Description	Lower Intercept Age (Ma)	Uncert. Int. (±2σ, Ma)	Uncert. With Ssys (±2σ, Ma)*	Relative Uncertainty (±2σ, %)	Number of analyses	MSWD	p(χ ²)
ACB18	U-Pb Grt	23.23	3.58	3.60	15.48%	45 /55	3.40	0.0
ACB35	U-Pb Grt, Zr > 25 ppm	127.97	9.08	9.28	7.25%	26 /36	2.90	0.0
	U-Pb Grt, Zr < 25 ppm	34.04	4.37	4.40	12.93%	25 /35	2.80	0.0
ACB_Sp3b	U-Pb Grt	26.92	1.25	1.31	4.88%	54 /59	1.90	0.0
ACB_Sp7b	U-Pb Grt	30.51	6.79	6.81	22.31%	57 /58	0.47	1.0
ACB_Sp8c	U-Pb Grt	24.04	2.07	2.10	8.74%	68 /71	0.92	0.7
ACB_Sp8d	U-Pb Grt	20.09	1	1.04	5.20%	33 /33	0.86	0.7
B19-1417	Bt, Undeformed RG1	15.15	-	0.71	4.69%	27 /29	0.34	1.0
ACB3b	Bt, D2 in RG1	15.25	-	0.88	5.77%	28 /30	0.65	0.9
ACB12b	Wm, Bulk RG2 fol	18.59	-	1.87	10.06%	35 /37	0.76	0.8
ACB14c	Bt, Bulk RG2 fol	15.01	-	1.17	7.79%	30 /30	0.42	1.0
ACB27a	Wm, D2	18.14	-	0.8	4.41%	38 /39	1.50	0.0
ACB37b	Wm, D3	14.68	-	1.55	10.56%	35 /36	1.30	0.1
ACB_Sp6	Bt, Bulk RG2 fol	14.77	-	0.74	5.01%	30 /30	0.65	0.9
*Systematic, long-term excess variance used for propagation is 1.5%								
Note. Samples in bold are discussed in the main text.								

575

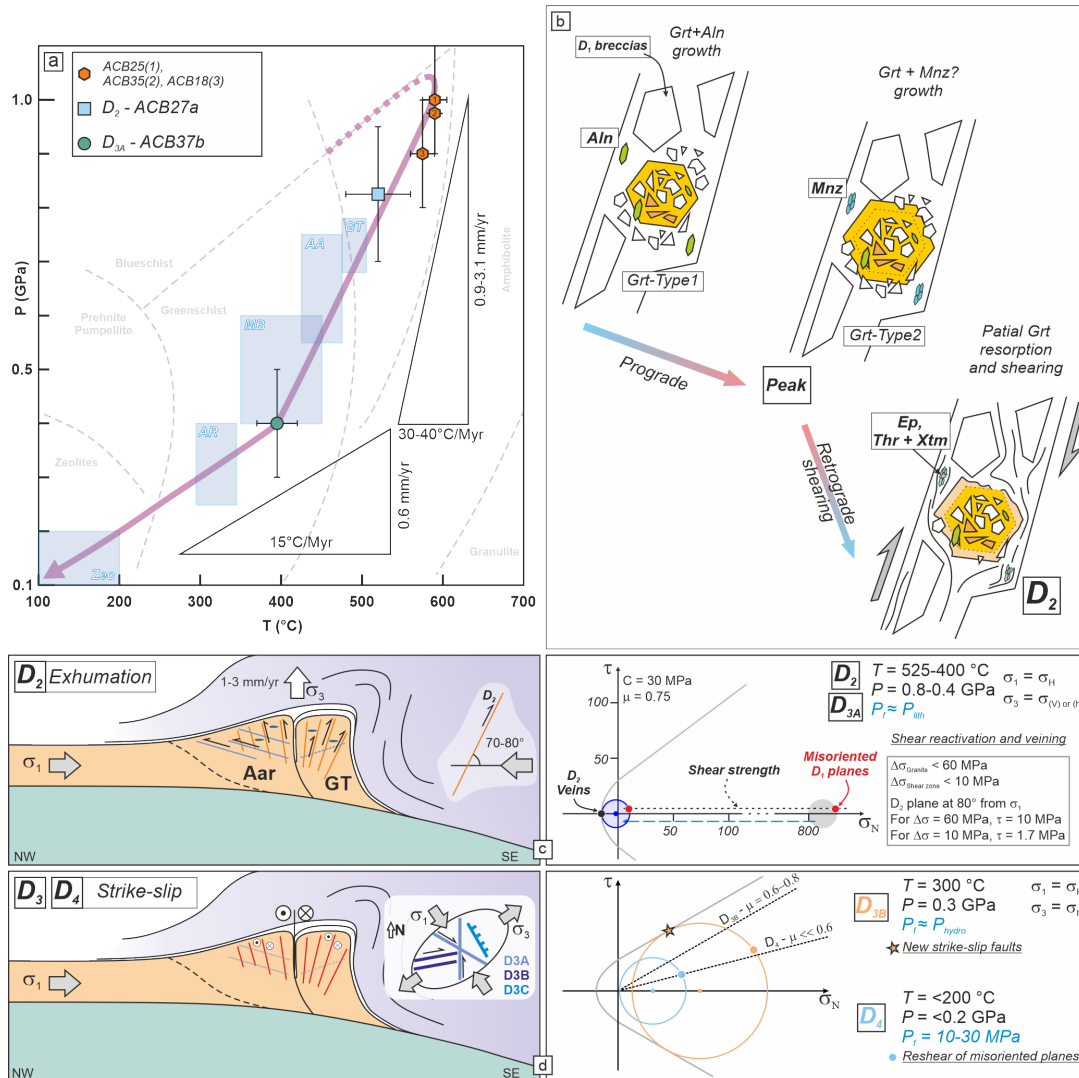
Table 1. Summary of the results from U-Pb in garnet and Rb-Sr in mica analyses.



577 **Figure 8.** *P-T-t* data for sample ACB27a-ACB37b. (a-b) Computed pseudosections for
 578 sample ACB27a and ACB37b, respectively. (c) ACB27a, (d) ACB37b, (e) ACB12b and (f) B19-
 579 1417 mica Rb-Sr isochrones including their corresponding ages (slope) and initial $^{87}\text{Sr}/^{86}\text{Sr}$
 580 composition (intercept). The size of the ellipses indicates internal 2SE (standard error).
 581 Isochronous regressions are plotted as black lines with their 95% confidence level as gray
 582 envelopes. All plots were generated using IsoplotR (Vermeesch, 2018).

583 **5. Discussion**

584 Here, we discuss and interpret the field observation and petrochronological data to (1)
 585 define the time-constrained *P-T-d* path and (2) to characterize the rheological evolution of the
 586 Rotondo granite, including the factors controlling it, during collisional tectonics.



587 **Figure 9.** *P-T-t* path for the Rotondo granite and sketch of its tectonic evolution. (a)
 588 Diagram summarizing the *P-T* conditions of deformation retrieved from thermodynamic
 589 modeling. Light blue boxes report the *P-T* conditions of peak/retrograde shear zone from other
 590 ECMs (AA: Aar/Grimsel, Goncalves et al., 2012; AR: Aiguille Rouges, Egli et al., 2017; MB:
 591 Mont Blanc: Rolland et al., 2009; GT: Gotthard-Fibbia, Oliot et al., 2014; Zeo: zeolite-faults
 592

593 from Lützenkirchen & Loew, 2011). Exhumation and cooling rates are reported. (b) Sketch
 594 representing the possible microstructural evolution and Grt nucleation between D₁ and D₂
 595 deformation stages. See text for explanation. (c-d) Sketch (not to scale) of the tectonic and
 596 rheological evolution of the Rotondo granite and Gotthard nappe through the D₂-D₄ deformation
 597 stages. See text for explanation. σ_v : vertical principal stress; σ_H : major horizontal stress; σ_h :
 598 minor horizontal stress. Mohr plots computed with MohrPlotter
 599 (<https://www.rickallmendinger.net/mohrplotter>). GT: Gotthard nappe; Penninic a.w.: Penninic
 600 accretionary wedge.

601 5.1. P-T-t-d path and tectonic evolution

602 The *P-T-t-d* path summarizing the structural, petrochronological, and rheological
 603 evolution of the granite is presented in Fig. 9.

604 5.1.1. Brittle-to-ductile evolution and Alpine peak metamorphic conditions

605 The oldest structures observed in the granite consist of D₁ shear fractures, cataclasites and
 606 breccias. Similar brittle structures pre-dating ductile shear zones are reported from several other
 607 crystalline units of the Alps (External and Internal Crystalline Massifs: Bertini et al., 1985;
 608 Ceccato et al., 2022; Goncalves et al., 2012; Guermani & Pennacchioni, 1998; Menegon &
 609 Pennacchioni, 2010; Oliot et al., 2014; Rolland et al., 2009; Wehrens et al., 2016; Tauern
 610 Window: Leydier et al., 2019; Mancktelow & Pennacchioni, 2020; Suretta nappe: Goncalves et
 611 al., 2016). In many cases these brittle structures were interpreted to have formed in the biotite
 612 stability field, suggesting they were formed at relatively high T (>350 °C) and mid-to-lower
 613 crustal conditions (Goncalves et al., 2016; Wehrens et al., 2016). Accordingly, they have been
 614 interpreted to represent either (a) a pro-grade phase of brittle Alpine deformation (Guermani &
 615 Pennacchioni, 1998), or (b) brittle (seismic) deformation at mid-crustal depths at the Alpine peak
 616 metamorphic conditions (Leydier et al., 2019; Mancktelow & Pennacchioni, 2020; Wehrens et
 617 al., 2016). It is interesting to note that such brittle-to-ductile evolution at peak metamorphic
 618 conditions has been reported from different crystalline units across the Alps spanning the whole
 619 range of “peak metamorphic conditions” recorded for the different case studies, from sub-
 620 greenschist to high-pressure amphibolite facies (see Ceccato et al., 2022; Fig. 9a). Conversely,
 621 recent studies proposed an inherited origin for similar brittle structures occurring in the ECMs,
 622 suggesting their development during the Permo-Mesozoic rifting (Ballèvre et al., 2018;
 623 Dall’Asta et al., 2022; Herwegh et al., 2020).

624 Although we don’t have quantitative constraints on the timing or exact *P-T* conditions of
 625 formation of D₁ structures, their micro and macro-structural relationships provide several clues
 626 about their relative timing with respect to Alpine collision, and their deformation conditions. In
 627 terms of relative timing, firstly, a key observation is that D₁ structures are overprinted by D₂
 628 mylonitic shear zones without mutual cross-cutting relationship. Secondly, in the present
 629 orientation, D₁ structures are oriented at high angles (70-80°) with respect to the long-term
 630 NNW-SSE shortening direction and maximum principal stress σ_1 during Alpine convergence and
 631 D₂ reverse shearing (Fig. 9d-e). This high-angle orientation (much larger than the ~30° expected
 632 for Andersonian thrust faults) makes it difficult to explain the origin of D₁ structures as reverse
 633 brittle faults during Alpine convergence. As discussed by Herwegh et al. (2020) for similar
 634 brittle structures occurring in the Aar massif, exaggerated rotation (>60°) of the entire massif
 635 would be necessary to re-orient low-angle thrust planes into the observed D₁ orientation. Indeed,

636 such high angle orientation would be more consistent with the development of faults and
637 fractures under a strike-slip or extensional tectonic regime (Sibson, 2003). The steep orientation
638 of D₁ structures is a common feature of many of the shear zones presenting a brittle-to-ductile
639 evolution in the ECMs (e.g., Bertini et al., 1985; Guermani & Pennacchioni, 1998; Oliot et al.,
640 2014; Rolland et al., 2009; Wehrens et al., 2016; Herwegh et al., 2017, 2020). If we extrapolate
641 our observations from the Rotondo to the other massifs, the common D₁ steep orientation
642 suggests that little or no reorientation occurred regionally, and that this orientation might
643 represent an original feature of the brittle deformation structures at the regional scale. These
644 observations suggest the D₁ structures pre-date Alpine convergence, rather than being
645 synkinematic with cyclical brittle-ductile deformation at peak metamorphic conditions, as
646 instead proposed for other case studies (Herwegh et al., 2017; Mancktelow & Pennacchioni,
647 2020; Wehrens et al., 2016).

648 The geochemical and age relationships observed in Grt porphyroblasts that overprint D₁
649 structures provide further constraints on the earliest stages of Rotondo granite deformation and
650 the transition from D₁ to D₂ structures. Firstly, Grt postdates breccia formation, statically
651 overprinting the pre-existing texture (Fig. 6a). Later deformation during peak to D₂ retrograde
652 shearing led to foliation development in the matrix surrounding the Grt. The foliation-parallel,
653 elongated, and honeycomb-like crystal shapes (Fig. 6b) may suggest that Grt partially re-
654 equilibrated or crystallized synkinematically to early D₂ shearing at conditions close to peak
655 metamorphism. However, most of the D₂ shear zones do not contain Grt, probably indicating its
656 metastability during the main phase of retrograde D₂ shearing related to exhumation. Thus, we
657 define three main stages of early Rotondo evolution (Fig. 9b): (i) D₁ brecciation and cataclasis,
658 (ii) Grt growth at a post-kinematic stage relative to D₁; (iii) shearing and likely Grt
659 destabilization during D₂.

660 A diachronous two-stage evolution of Grt is supported by its REE and U-Pb systematics.
661 The two Grt compositions (Grt-Type1, Grt-Type2), characterized by different LREE patterns
662 have to be interpreted along with accessory mineral phases (Aln, Ep, Mnz) observed as
663 inclusions and in the ductile matrix overprinting D₁ breccia in sample ACB35. The depletion of
664 LREE observed for Grt-Type1 is consistent with growth of Grt in apparent equilibrium with
665 accessory phases preferentially partitioning LREE, such as Aln. Indeed, Aln inclusions are (only)
666 observed in some of the analyzed garnets. Similarly, the enrichment of LREE observed in Grt-
667 Type2 is consistent with garnet growth at conditions where LREE-rich phases (e.g., Aln) are not
668 stable anymore and the only phase capable of incorporating LREEs is garnet. In fact, Ep-
669 rich/Aln-poor grains are observed in the paragenesis of the sheared breccia matrix, surrounding
670 Xtm/Thr aggregates, in turn resulting from the destabilization of first generation Aln or Mnz
671 (Fig. 6f; Janots et al., 2008; Hentschel et al., 2020). In summary, a first phase of Grt (Grt-Type1)
672 crystallization in apparent equilibrium with Aln is followed by a second phase of crystallization
673 of Grt (Grt-Type2) during which Aln was not stable anymore, replaced by Mnz during prograde
674 metamorphism (e.g. Janots et al., 2008, 2009; Spear, 2010). The exact *T* of transition from Aln-
675 bearing to Mnz-bearing paragenesis could shift from *T* ~ 350 °C to *T* ~ 550 °C depending on the
676 bulk CaO and REE content of the rock (Spear, 2010). A similar prograde crystallization
677 sequence has been reported from metapelites in the south-eastern Gotthard nappe described by
678 Janots et al. (2008, 2009). In that case, prograde destabilization of Aln close to peak conditions
679 of about 560-580 °C formed the Mnz and REE-poor Ep aggregates observed in the recrystallized
680 metapelite hosting the Grt (Janots et al., 2008). Mnz is rare in our samples, and it is likely that
681 Mnz destabilization during retrograde D₂ shearing at amphibolite-to-greenschist facies

682 conditions may have led to the formation of the Ep + Xtm/Thr aggregates observed in the
 683 recrystallized breccia matrix (e.g., Hentschel et al., 2020). Therefore, Ep/Aln microstructures in
 684 ACB35 Grt likely record a prograde-to-peak crystallization sequence (Fig. 9b). Interestingly, in
 685 both ACB35 and especially ACB18 samples, the compositional zoning of garnet suggests
 686 increasing P - T conditions from core to rim (Fig. 7a, SI Fig. S2b).

687 U-Pb dating of Grt results in scattered ages ranging from ~34 to ~20 Ma, which is
 688 broadly consistent with the ages for the regional peak metamorphism obtained from other case
 689 studies in the Gotthard nappe (22-19 Ma, Janots et al., 2009; Janots & Rubatto, 2014; Boston et
 690 al., 2017) and nearby Lepontine Dome (32-22 Ma, Rubatto et al., 2009). The peak metamorphic
 691 conditions are constrained by pseudosections calculated for different samples (ACB35, ACB25,
 692 ACB18) at 590 ± 15 °C and 0.9 ± 0.1 GPa. The obtained P - T conditions are consistent with
 693 recent estimates of Alpine peak metamorphic conditions from the southern Aar massif and
 694 Gotthard nappe (Berger et al., 2020; Janots et al., 2008, 2009; Nibourel et al., 2021; Wiederkehr
 695 et al., 2011), as well as the Penninic units of the Northern Lepontine dome (Boston et al., 2017;
 696 Galli et al., 2007). The 34-20 Ma age spread would describe a prolonged thermal peak in the
 697 Gotthard nappe lasting for ~10 Myrs (Fig. 9b). This conclusion is consistent with
 698 geochronological data supporting the occurrence of a prolonged thermal peak starting at ~32-34
 699 Ma in several other ECMs and Penninic units, lasting until 22-17 Ma when the main phase of
 700 exhumation occurred (Boston et al., 2017; Cenko-Tok et al., 2014; Egli et al., 2016; Girault et al.,
 701 2020; Janots et al., 2008, 2009; Rolland & Rossi, 2016; Rubatto et al., 2009; Sanchez et al.,
 702 2011).

703

704 5.1.3. Exhumation – D₂ shear zones

705 The reverse kinematics of D₂ shear zones and the occurrence of associated shallowly
 706 dipping tensional veins constrain a subhorizontal σ_1 , parallel to a NW-SE trending maximum
 707 shortening axis ϵ_1 , and perpendicular to a subvertical σ_3 (Fig. 9c). Based on the results of
 708 pseudosection calculation, these shear zones were already active at 520 ± 40 °C and 0.82 ± 0.12
 709 GPa. The conditions of re-equilibration of the analyzed samples (ACB27a $T > 500$ °C) are
 710 similar to the closure temperature for Rb-Sr in white mica inferred for similar case studies of
 711 granitoid shear zones ($T \leq 500$ -550 °C; e.g., Egli et al., 2015; Ribeiro et al., 2023). Therefore, it
 712 is very likely that the obtained Rb-Sr date of 18.1 ± 0.8 Ma (Fig. 8) reflects the (re-)
 713 crystallization of white mica in D₂ ductile shear zones. D₂ ductile shear zones accommodate the
 714 main phase of tectonic exhumation of the Gotthard nappe through reverse shearing on NW-
 715 steeply dipping planes. Rb-Sr dating of white mica indicates that the bulk foliation of RG₂
 716 developed during the same amphibolite-facies deformation event at 18.6 ± 1.9 Ma (sample
 717 ACB12b, Fig. 8e). However, biotite in D₂ shear zones (15.3 ± 0.9 Ma, sample ACB3b, SI Text
 718 S4, Fig. S4) provides a younger Rb-Sr age which indicates either a later deformation event or,
 719 more likely, reflects the lower closure temperature of the Rb-Sr isotope system in biotite (≤ 350 -
 720 400 °C; e.g., Jenkin et al., 2001) compared to white mica (≤ 500 °C). The exhumation of the ECMs
 721 in the Central and Western Alps have been accommodated by similar steeply-dipping, reverse
 722 shear zones developed during retrograde greenschist facies conditions between 22 and 17 Ma
 723 (Cenko-Tok et al., 2014; Goncalves et al., 2012; Herwegh et al., 2020; Rolland et al., 2008).

724

725 5.1.4. Strike-slip tectonics – D₃-D₄

726 The kinematics and geometrical relationships of D_{3A} and D_{3B} structures constrain their
 727 development under a transpressional strain field developed during NW-SE convergence (D_{3A}-
 728 D_{3B}), associated with NE-SW-directed extension (D_{3B} tensional veins and D_{3C} normal faults; Fig.
 729 9d). The kinematics of D₃ shear zones and tensional veins constrain a subhorizontal σ_1 and
 730 maximum shortening axis ϵ_1 oriented ~NW-SE and a sub-horizontal, NE-SW-oriented σ_3 (Fig.
 731 9d). Strike-slip D_{3A} shearing is constrained to develop at 395 ± 25 °C and 0.4 ± 0.1 GPa. At these
 732 temperature conditions, the Rb-Sr chronometer applied to white mica constraints the age of mica
 733 (re-)crystallization because the closure temperature of Sr diffusion in white mica is considerably
 734 higher (see previous section). Hence, the 14.7 ± 1.6 Ma age of white mica in D_{3A} sample
 735 ACB37b (Fig. 8) probably constrains the age of this deformation event. The occurrence of
 736 similar Rb-Sr ages for white mica (ACB37b, D_{3A}) and biotite (B19-1417, undeformed granite:
 737 15.5 ± 0.7 Ma; ACB3b and ACB14c, foliated granite: 15.3 ± 0.9 Ma and 15.0 ± 1.2 Ma,
 738 respectively; Table 1, Fig. 8, and SI Fig. S4), regardless of the intensity of sample deformation,
 739 suggests that the D_{3A} deformation event occurred at conditions broadly corresponding to the
 740 closure temperature of the Rb-Sr chronometer in biotite, that is $\sim \leq 350$ °C (e.g., Jenkins et al.,
 741 2001). If the temperatures were substantially higher (e.g., 400-500 °C), white mica would have
 742 recorded an older age due to its higher closure temperature for the Rb-Sr isotope system. In other
 743 words, the ~15 Ma age of biotite in the undeformed Rotondo granite represents a cooling age.
 744 The overlap of white mica and biotite Rb-Sr ages implies that ductile reactivation of D₂ under
 745 strike-slip conditions leading to D_{3A} shear zones occurred during a very short time period at ~15
 746 Ma. Further deformation during D₃ strike-slip tectonics was accommodated by brittle-ductile
 747 transpressional and extensional faults. The NW-SE-striking extensional veins associated to this
 748 brittle-ductile deformation event in the Lepontine dome and Aar-Gotthard area are consistently
 749 dated to <14 Ma (Bergemann et al., 2020). The contemporaneous (or cyclic) development of
 750 D_{3B}-D_{3C} extensional and transpressional structures is consistent with the regional tectonic setting
 751 during the activity of the Rhone-Simplon fault system (Campani et al., 2010), accommodating
 752 NE-SW extensional tectonics under a constant dominant NW-SE transpression.

753 Late D₄ zeolite- and gouge-bearing brittle faults reactivated the pre-existing, steeply
 754 dipping structural discontinuities under strike-slip conditions (Lützenkirchen & Loew, 2011).
 755 Their activity is constrained to have occurred between 12 and 3 Ma based on K-Ar illite dating
 756 (Kralik et al., 1992; Pleuger et al., 2012) at upper crustal levels ($T < 200$ °C, depth <7 km;
 757 Lützenkirchen & Loew, 2011). These chronological constraints are consistent with the prolonged
 758 Neogene activity of the Periadriatic-Simplon-Rhone fault system (Ricchi et al., 2019).

759 In conclusion, the brittle-ductile-brittle evolution inferred from the sequence of
 760 deformation structures in the Rotondo granite is the result of pre-Alpine tectonics overprinted by
 761 the peak-and-retrograde collisional Alpine tectonics. Pre-collisional structures apparently
 762 controlled the localization and accommodation of collisional strain in the crystalline unit.

763 5.1.5. Exhumation and cooling rates during Alpine collision

764 Rates of tectonic exhumation and cooling can be calculated considering the constraints on
 765 P , T , and age of deformation provided above (Fig. 9a). Rates are computed considering a
 766 geothermal gradient of 25 °C/km and a lithostatic pressure gradient of 27.5 MPa/km (e.g.,
 767 Nibourel et al., 2021). Exhumation from peak conditions at 590 °C and 0.9 GPa at 34 to 20 Ma
 768 (U-Pb of garnet) to 520 °C and 0.8 GPa (D₂ conditions) at 18 Ma (Rb-Sr in white mica) occurred

769 at a rate of 0.22 to 1.8 mm/yr (km/Myr), associated with a cooling rate ranging between 5 to 35
 770 °C/Myr, respectively for the oldest and youngest U-Pb ages. Most of the exhumation was
 771 accommodated through the activity of D₂ ductile reverse shear zones. They accommodated the
 772 exhumation from D₂ conditions (520 °C and 0.8 GPa) at 18 Ma (Rb-Sr on white mica) to D₃
 773 conditions (395 °C and 0.4 GPa) at ~14 Ma (Rb-Sr on white mica and biotite). Related
 774 exhumation rates range between 3.8 and 5.1 mm/yr, with an associated cooling rate of 30-40
 775 °C/Myr. On average, the exhumation from peak metamorphic conditions at 34-20 Ma to the
 776 brittle-ductile conditions recorded after D_{3A} deformation at 14 Ma occurred at an average
 777 exhumation rate of 0.9-3.0 mm/yr, associated with a cooling rate of 10-30 °C/Myr. Such
 778 exhumation rates are comparable to those retrieved from regional thermochronometry (~1-3
 779 mm/yr; Glotzback et al., 2010; Herwegh et al., 2020; Nibourel et al., 2021). Similarly, the high
 780 cooling rates recorded during D₂-D₃ exhumation are compatible with the estimates of 30-40
 781 °C/Myr provided by Janots et al. (2009) for the eastern Gotthard nappe.

782 After the exhumation through the brittle-ductile transition, and the switch to regional
 783 transpression, the exhumation became much slower, as constrained by comparing D₃ Rb-Sr
 784 white mica/biotite ages and the youngest K-Ar illite age (3 Ma) Kralik et al. (1992) and Pleuger
 785 et al. (2012) for gouge-bearing faults similar to D₄ structures. The obtained exhumation rate of
 786 ~0.6 mm/yr is associated with a cooling rate of ~15 °C/Myr (Fig. 9a), similarly to what
 787 previously reported from thermochronological constraints (Glotzback et al., 2010; Herwegh et
 788 al., 2020).

789

790 5.2. Rheological evolution of the Rotondo granite during Alpine collision

791 In the RG, collisional shortening is accommodated through the reactivation and shearing
 792 of pre-collisional D₁ structures and pre-existing compositional and structural heterogeneities at
 793 different scales. In the current orientation D₁ brittle structures are severely misoriented, forming
 794 high angles to the maximum principal stress expected during NW-directed Alpine convergence
 795 and collision (Rosenberg et al., 2021). Despite this fact, these structures influenced the rheology
 796 and localized strain throughout the whole D₂-D₄ evolution across different *P-T* and rheological
 797 conditions of the crystalline basement (Fig. 9c-d). In the following sections, we constrain the
 798 rheology, as well as the stress and fluid regimes at which D₁ to D₄ structures likely formed.

799 The current high-angle dip of the D₁ brittle structures would be more compatible with an
 800 extensional or strike-slip tectonic regime than with a compressional/convergent setting. Given
 801 the uncertainty regarding the tectonic regime and original orientation of D₁ structures, we can
 802 only speculate about the values of differential stress ($\Delta\sigma$) and pore fluid pressure (P_f) during D₁
 803 development. The occurrence of thin shear fractures and cataclasites may indicate a dynamic
 804 environment characterized by variable $\Delta\sigma$ ($> 4 \cdot T_s - 5.6 \cdot T_s$, with T_s : tensile strength) and low P_f .
 805 Furthermore, the mutual overprinting between breccias and (fault-)veins implies cyclical
 806 variation of P_f and permeability in the brittle regime. Fluid-assisted brecciation is related to
 807 transient fluid-pressure increase in low-permeability rocks and facilitated in extensional regimes,
 808 as well as along pre-existing structures (Jébrak, 1997; Sibson et al., 1988). Fault-veins (lenticular
 809 Qz-veins parallel to the shear plane) suggest the fluid-driven reactivation of a pre-existing
 810 structure, at low $\Delta\sigma$ and likely sublithostatic P_f (probably < 300 MPa in the brittle field; Sibson
 811 et al., 1988). Similar conclusions can be drawn from the geometry of breccias, locally resembling
 812 crackle and mosaic breccias with randomly distributed fractures (Fig. 3c-d). These geometries

813 indicate very low $\Delta\sigma$ ($< 4 \cdot Ts$), and effective σ_1 close to zero ($\Delta\sigma \sim Ts$; Woodcock et al., 2007),
 814 and they are in some instances interpreted as resulting from seismic activity (Sibson, 1985, 1987;
 815 Melosh et al., 2014). Nonetheless, we cannot exclude that at least part of the veining occurred
 816 during prograde (brittle) reactivation of D_1 misoriented faults under compression, defining a
 817 general fault-valve behavior (Sibson et al., 1988). Such activity, if present, was only limited to
 818 pre-peak and brittle conditions, given the lack of brittle-over-ductile overprint in D_1 structures.

819 During D_2 - D_3 retrograde shearing at amphibolite-to-upper greenschist facies conditions
 820 ($T = 400$ - 520 °C, $P = 0.4$ - 0.8 GPa), the granite was characterized by a network of high strain
 821 shear zones, localized on magmatic (aplitic, mafic dykes) and tectonic (D_1) precursors,
 822 delimiting low strain domains of relatively undeformed granite. D_2 shear zones are oriented at
 823 high angle (70 - 80°) to the principal stress σ_1 (Fig. 9d-e). Accordingly, shearing on D_2 planes
 824 developed even if the resolved shear stress was very small, thus suggesting a limited shear
 825 strength of such D_2 ductile shear zones. Shear zone strength was controlled by reaction-
 826 weakening processes related to plagioclase destabilization, which led to the activation of fluid-
 827 mediated grain-size sensitive deformation mechanisms, as observed in similar granitoid ductile
 828 shear zones (Ceccato et al., 2022; Oliot et al., 2014). This localized weakening might have been
 829 related to the higher fluid content of D_1 structures exploited by D_2 compared to the host rock.
 830 This higher fluid content is likely related to either a fluid-bearing mineral paragenesis of former
 831 D_1 structures, or to the increased permeability of the granite along D_1 structures promoting fluid
 832 flux during retrograde D_2 shearing (e.g., Oliot et al., 2010). Further analyses would be necessary
 833 to discern between the two options and to understand the origin of the fluids and weakening. In
 834 any case, ductile shear zones acted as fluid pathways during D_2 deformation as can be inferred
 835 from the occurrence of sheared Qz + Cal veins (Fig. 4a), including Cal porphyroclasts (Fig. 11 of
 836 Rast et al., 2022). Cal porphyroclasts in Qz-mylonites have been constrained to develop during
 837 ductile shearing at low $\Delta\sigma$ (< 10 MPa) at amphibolite facies, fluid-rich conditions (Mancktelow
 838 & Pennacchioni, 2010). This further suggest that the D_2 ductile shear zones were extremely weak
 839 and able to accommodate strain at very low shear stresses, probably on the order of few (1-4)
 840 MPa, considering a $\Delta\sigma$ of 10 MPa) and an orientation of 80 with respect to σ_1 (Fig. 9c).
 841 Accordingly, the pervasive occurrence of tensional veins in the undeformed granite indicates
 842 high (quasi-supralithostatic) P_f and limited $\Delta\sigma$ ($< 4 \cdot Ts$, in the range 36 to 60 MPa for granite,
 843 Cox, 2010; Etheridge, 1983; Sibson, 2003; Sibson et al., 1988). Therefore, during D_2 - D_3 ductile
 844 shearing: (i) there is a difference in the maximum $\Delta\sigma$ of ~ 25 - 50 MPa between weak shear zones
 845 (< 10 MPa) and in the low-strain granite (< 60 MPa); (ii) the strength of both high-strain shear
 846 zone and low strain granite domains is limited by tensional veining related to fluid overpressure,
 847 which in turn implies (iii) low permeability in the low strain granite during ductile deformation.
 848 D_2 ductile shear zones might have acted as higher-permeability fluid conduits, but overall the
 849 permeability was not high enough to allow the dissipation of P_f build-up to supralithostatic
 850 conditions.

851 During further cooling and exhumation ($T < 350$ °C, $P = 0.2$ - 0.4 GPa), pre-existent
 852 misoriented structures failed to be reactivated (Fig. 9d). The development of new conjugate
 853 faults (D_{3B}) suggests increasing $\Delta\sigma$ ($> 5.6 \cdot Ts$) and decreasing P_f (probably close to hydrostatic
 854 conditions) during strike-slip deformation across the brittle-ductile transition. The decreased P_f
 855 was also related to the increased porosity and permeability of the granite during this deformation
 856 stage. High permeability of such deformation structures is documented by the pervasive
 857 occurrence of mineralized open veins along fault shear planes (Fig. 5a), as well as by the

858 occurrence of high-porosity hydrothermal alteration and the development of episyenites
859 (Pennacchioni et al., 2016).

860 At shallow crustal levels ($T < 200$ °C, $P < 0.2$ GPa), D₄ zeolite- and gouge-bearing faults
861 reactivated the rock fabrics and pre-existent structural heterogeneities instead of developing new
862 fractures and fault zones (Fig. 9d). Fluids leading to the crystallization of zeolites percolated
863 through the highly permeable network of pre-existing fractures and structural heterogeneities.
864 Similar zeolite-bearing fractures and faults are reported from the granitoid plutons of the Central
865 and Eastern Alps (e.g., Adamello: Pennacchioni et al., 2006; Rieserferner: Ceccato &
866 Pennacchioni, 2018), as well as from all the crystalline massifs of the Central Alps (e.g.,
867 Weisenberger and Bucher, 2010). For instance, in the Adamello, similarly to the Rotondo, zeolite
868 veins and gouges are observed to intrude the pre-existent fracture and fault network, locally
869 reactivating fault planes (Pennacchioni et al., 2006). The observed complex kinematics of
870 reactivation and the fluid-overpressure inferred from the occurrence of zeolite-bearing veins and
871 gouges were interpreted to be the result of earthquake swarm activity at shallow crustal levels
872 (Dempsey et al., 2014). In that case, zeolite-bearing gouges were developed during transient
873 high-stress or high pore-fluid pressure events. In the RG, low P_f of 10-30 MPa were estimated
874 from the stability of fault zeolite paragenesis (Lützenkirchen & Loew, 2011). In addition,
875 shearing planes in the granite are highly misoriented with respect to the NW-SE Alpine
876 shortening direction. Thus, transient high differential stress would have promoted the
877 development of new conjugate shear fractures, rather than reactivating misoriented planes.
878 Nonetheless, D₄ structures localize on D₁-D₂-D₃ structures (Lützenkirchen & Loew, 2011),
879 which are characterized by phyllosilicate-bearing fabrics that affect the frictional and cohesion
880 properties of the shearing planes at brittle conditions (Bistacchi et al., 2012; Volpe et al., 2022;
881 Pozzi et al., 2022). In addition, the low frictional properties of the fault gouges developed during
882 shearing might have further promoted the localization of brittle faulting on highly misoriented,
883 and otherwise frictionally-locked, fault planes during the latest stages of Alpine brittle
884 deformation (Bistacchi et al., 2012; Collettini et al., 2019; Volpe et al., 2023).

885

886 6. Conclusions

887 The P - T - t - d evolution of the Rotondo granite is recorded by a brittle-ductile-brittle
888 structural evolution. D₁ breccias and cataclasites develop in the Rotondo granite before the
889 attainment of the Alpine peak metamorphic conditions, the latter occurring between 34 and 20
890 Ma and recorded by U-Pb in garnet. Peak metamorphic conditions are closer to the amphibolite
891 facies ($T > 550$ °C, $P > 0.7$ GPa) than those previously proposed for the ECMs and the Gotthard
892 nappe ($T < 450$ - 500 °C, $P < 0.5$ - 0.6 GPa; Todd and Engi, 1997). Retrograde exhumation was
893 then controlled by reverse ductile shearing on D₂ ductile shear zones, localized on pre-existent
894 structural and compositional heterogeneities. The very limited shear strength of D₂ ductile shear
895 zones allowed it to accommodate fast exhumation of the Gotthard nappe at 1-3 km/Myr between
896 20 and 14 Ma. Further exhumation was accommodated at slower rates by D₃ greenschist facies
897 ($T < 400$ °C, $P < 0.4$ GPa) ductile and brittle-ductile shear zones, developed as a local response to
898 the regional strike-slip activity of the Simplon-Rhone fault system.

899 Based on the common structural and tectonometamorphic history of the Rotondo granite
900 and the other ECMs in the Central and Western Alps, we can extrapolate the results obtained

901 from the Rotondo to infer fundamental implications for the rheology of the European continental
902 crust during Alpine collision:

- 903 • The European continental crust, now exposed in the ECMs, was extremely weak
904 during Alpine continental collision and deformation at amphibolite-to-greenschist
905 facies.
- 906 • The occurrence of inherited tectonic and primary (e.g., magmatic) fabrics and
907 structures, although highly misoriented, clearly controlled strain geometry and
908 localization throughout their entire rheological and metamorphic evolution.
- 909 • The main weakening event occurred during retrograde conditions.

910 The weakness of the European continental crust during Alpine collision allowed it to
911 focus and localize collisional strain in the external domains of the orogen, promoting the
912 localized and fast exhumation of the crystalline massifs ahead of the advancing dry and strong
913 Adriatic lower crust. At the scale of the orogen, collisional shortening was therefore
914 accommodated through the localized, and fast exhumation of the External Crystalline Massifs,
915 by means of the activity of weak ductile shear zones, localized on pre-existing tectonic and
916 primary fabrics.

917

918 **Acknowledgments**

919 This paper is FEAR Publication #19. This research is supported by ETH Zurich research
920 funds to WMB and the European Research Council (ERC) Synergy project “Fault Activation and
921 Earthquake Rupture” (FEAR) (grant 856559) granted to Domenico Giardini, Stefan Wiemer,
922 Massimo Cocco, and Florian Amman. Markus Rast is warmly thanked for the introduction to the
923 Bedretto tunnel geology and for providing the sample B19-1417 and thin sections adopted for
924 Rb-Sr analysis of biotite. Neil Mancktelow and Bernardo Cesare are thanked for fruitful
925 discussions about regional geology and garnet petrography. The authors acknowledge Luiz G.
926 Morales and ScopeM for their support and assistance during SEM data acquisition and
927 processing. Julien Allaz is thanked for EPMA data acquisition and technical assistance. Remy
928 Lüchinger and Lydia Zender are gratefully acknowledged for their support during thin section
929 preparation and XRF analyses, respectively. The crew of the Capanna Piansecco and SAC-CAS
930 Bellinzona & Valli are warmly thanked for their logistic support, and their friendly and
931 unconditional hospitality during fieldwork in the Rotondo area. The authors acknowledge the
932 logistic support from the Bedretto Lab team.

933

934 **Open Research**

935 Chemical and geochronological data supporting the conclusions of the present study are
936 reported in the main text and in the Supplementary Information files. The dataset is also
937 available at ETH Zurich Research Collection via <https://doi.org/10.3929/ethz-b-000644819> with
938 Creative Commons Attribution 4.0 International license (Ceccato et al., 2023).

939

940

941 **References**

- 942 Aysal, N. et al., 2023, A New Natural Secondary Reference Material for Garnet U-Pb
943 Dating by TIMS and LA-ICP-MS. *Geostandards and Geoanalytical Research*, p. ggr.12493,
944 doi:10.1111/ggr.12493.
- 945 Ballèvre, M., Manzotti, P., & Dal Piaz, G. V. (2018). Pre-Alpine (Variscan) inheritance:
946 a key for the location of the future Valaisan basin (Western Alps). *Tectonics*, 37(3), 786–817.
947 <https://doi.org/10.1002/2017tc004633>
- 948 Behr, W. M., & Platt, J. P. (2014). Brittle faults are weak, yet the ductile middle crust is
949 strong: Implications for lithospheric mechanics. *Geophysical Research Letters*, 41(22), 8067-
950 8075. <https://doi.org/10.1002/2014GL061349>
- 951 Behr, W. M., & Platt, J. P. (2013). Rheological evolution of a Mediterranean subduction
952 complex. *Journal of Structural Geology*, 54, 136-155. <https://doi.org/10.1016/j.jsg.2013.07.012>
- 953 Bellahsen, N., Mouthereau, F., Boutoux, A., Bellanger, M., Lacombe, O., Jolivet, L., &
954 Rolland, Y. (2014). Collision kinematics in the western external Alps. *Tectonics*, 33(6), 1055–
955 1088. <https://doi.org/10.1002/2013TC003453>
- 956 Bellanger, M., Bellahsen, N., Jolivet, L., Baudin, T., Augier, R., & Boutoux, A. (2014).
957 Basement shear zones development and shortening kinematics in the Ecrins Massif, Western
958 Alps. *Tectonics*, 33(2), 84–111. <https://doi.org/10.1002/2013TC003294>
- 959 Beltrando, M., Frasca, G., Compagnoni, R., & Vitale-Brovarone, A. (2012). The Valaisan
960 controversy revisited: Multi-stage folding of a Mesozoic hyper-extended margin in the Petit St.
961 Bernard pass area (Western Alps). *Tectonophysics*, 579, 17–36.
962 <https://doi.org/10.1016/J.TECTO.2012.02.010>
- 963 Beltrando, M., Manatschal, G., Mohn, G., Dal Piaz, G. V., Vitale Brovarone, A., &
964 Masini, E. (2014). Recognizing remnants of magma-poor rifted margins in high-pressure
965 orogenic belts: The Alpine case study. *Earth-Science Reviews*, 131, 88–115.
966 <https://doi.org/10.1016/J.EARSCIREV.2014.01.001>
- 967 Bergemann, C., Gnos, E., Berger, A., Janots, E., & Whitehouse, M. J. (2020). Dating
968 tectonic activity in the Lepontine Dome and Rhone-Simplon Fault regions through hydrothermal
969 monazite-(Ce). *Solid Earth*, 11(1), 199–222. <https://doi.org/10.5194/se-11-199-2020>
- 970 Berger, A., Mercolli, I. P., Herwegh, M., & Gnos, E. (2017). Explanatory Notes to the
971 Geological map of the Aar massif, Tavetsch and Gotthard nappes, Geological special map No.
972 129. Wabern: Federal Office of Topography swisstopo.
- 973 Berger, A., Engi, M., Erne-Schmid, S., Glotzbach, C., Spiegel, C., de Goede, R., &
974 Herwegh, M. (2020). The relation between peak metamorphic temperatures and subsequent
975 cooling during continent–continent collision (western Central Alps, Switzerland). *Swiss Journal*
976 *of Geosciences*, 113(1), 1–18. <https://doi.org/10.1186/S00015-020-00356-4>
- 977 Bertini, G., Marcucci, M., Nevini, R., Passerini, P., & Sguazzoni, G. (1985). Patterns of
978 faulting in the Mont Blanc granite. *Tectonophysics*, 111(1–2), 65–106.
979 [https://doi.org/10.1016/0040-1951\(85\)90066-6](https://doi.org/10.1016/0040-1951(85)90066-6)

- 980 Bistacchi, A., Massironi, M., Menegon, L., Bolognesi, F., & Donghi, V. (2012). On the
981 nucleation of non-Andersonian faults along phyllosilicate-rich mylonite belts. *Geological*
982 *Society, London, Special Publications*, 367(1), 185-199. <https://doi.org/10.1144/SP367.13>
- 983 Boston, K. R., Rubatto, D., Hermann, J., Engi, M., & Amelin, Y. (2017). *Geochronology*
984 of accessory allanite and monazite in the Barrovian metamorphic sequence of the Central Alps,
985 Switzerland. *Lithos*, 286–287, 502–518. <https://doi.org/10.1016/J.LITHOS.2017.06.025>
- 986 Bühler, M., Zurbriggen, R., Berger, A., Herwegh, M., & Rubatto, D. (2022). Late
987 Carboniferous Schlingen in the Gotthard nappe (Central Alps) and their relation to the Variscan
988 evolution. *International Journal of Earth Sciences*, 1–26. [https://doi.org/10.1007/S00531-022-](https://doi.org/10.1007/S00531-022-02247-5)
989 [02247-5](https://doi.org/10.1007/S00531-022-02247-5)
- 990 Bürgmann, R., & Dresen, G. (2008). Rheology of the lower crust and upper mantle:
991 Evidence from rock mechanics, geodesy, and field observations. *Annu. Rev. Earth Planet. Sci.*,
992 36, 531-567. <https://doi.org/10.1146/annurev.earth.36.031207.124326>
- 993 Bussien, D., Bussy, F., Masson, H., Magna, T., & Rodionov, N. (2008). Variscan
994 lamprophyres in the Lower Penninic domain (Central Alps): Age and tectonic significance.
995 *Bulletin de La Societe Geologique de France*, 179(4), 369–381.
996 <https://doi.org/10.2113/gssgfbull.179.4.369>
- 997 Campani, M., Mancktelow, N., Seward, D., Rolland, Y., Müller, W., & Guerra, I. (2010).
998 Geochronological evidence for continuous exhumation through the ductile-brittle transition
999 along a crustal-scale low-angle normal fault: Simplon Fault Zone, central Alps. *Tectonics*, 29(3).
1000 <https://doi.org/10.1029/2009TC002582>
- 1001 Candioti, L. G., Duretz, T., Moulas, E., & Schmalholz, S. M. (2021). Buoyancy versus
1002 shear forces in building orogenic wedges. *Solid Earth*, 12(8), 1749–1775.
1003 <https://doi.org/10.5194/se-12-1749-2021>
- 1004 Ceccato, A., & Pennacchioni, G. (2018). Structural evolution of the Rieserferner pluton
1005 in the framework of the Oligo-Miocene tectonics of the Eastern Alps. *Journal of Structural*
1006 *Geology*, 116, 64-80. <https://doi.org/10.1016/j.jsg.2018.08.004>
- 1007 Ceccato, A., Menegon, L., Warren, C. J., & Halton, A. M. (2020). Structural and
1008 metamorphic inheritance controls strain partitioning during orogenic shortening (Kalak Nappe
1009 Complex, Norwegian Caledonides). *Journal of Structural Geology*, 136, 104057.
1010 <https://doi.org/10.1016/j.jsg.2020.104057>
- 1011 Ceccato, A., Goncalves, P., & Menegon, L. (2022). On the petrology and microstructures
1012 of small-scale ductile shear zones in granitoid rocks: An overview. *Journal of Structural*
1013 *Geology*, 161(June), 104667. <https://doi.org/10.1016/j.jsg.2022.104667>
- 1014 Ceccato, A., Behr, W. M., Zappone, A. S., Tavazzani, L., Giuliani, A., (2023). Datasets
1015 for "Structural evolution, exhumation rates, and rheology of the European crust during Alpine
1016 collision: constraints from the Rotondo granite – Gotthard nappe". *ETH Zurich Research*
1017 *Collection*. DOI 10.3929/ethz-b-000644819
- 1018 Cesare, B., Nestola, F., Johnson, T., Mugnaioli, E., Della Ventura, G., Peruzzo, L.,
1019 Bartoli, O., Viti, C. & Erickson, T. (2019). Garnet, the archetypal cubic mineral, grows
1020 tetragonal. *Scientific Reports*, 9(1), 14672. <https://doi.org/10.1038/s41598-019-51214-9>

- 1021 Célini, N., Mouthereau, F., Lahfid, A., Gout, C., & Callot, J. P. (2023). Rift thermal
1022 inheritance in the SW Alps (France): insights from RSCM thermometry and 1D thermal
1023 numerical modelling. *Solid Earth*, 14(1), 1–16. <https://doi.org/10.5194/SE-14-1-2023>
- 1024 Cenki-Tok, B., Darling, J. R., Rolland, Y., Dhuime, B., & Storey, C. D. (2014). Direct
1025 dating of mid-crustal shear zones with synkinematic allanite: new in situ U-Th-Pb
1026 geochronological approaches applied to the Mont Blanc massif. *Terra Nova*, 26(1), 29–37.
1027 <https://doi.org/10.1111/TER.12066>
- 1028 Challandes, N., Marquer, D., & Villa, I. M. (2008). P-T-t modelling, fluid circulation,
1029 and ³⁹Ar-⁴⁰Ar and Rb-Sr mica ages in the Aar Massif shear zones (Swiss Alps). *Swiss Journal*
1030 *of Geosciences*, 101(2), 269–288. <https://doi.org/10.1007/s00015-008-1260-6>
- 1031 Collettini, C., Tessei, T., Scuderi, M. M., Carpenter, B. M., & Viti, C. (2019). Beyond
1032 Byerlee friction, weak faults and implications for slip behavior. *Earth and Planetary Science*
1033 *Letters*, 519, 245-263. <https://doi.org/10.1016/j.epsl.2019.05.011>
- 1034 Connolly, J. A. D. (2005). Computation of phase equilibria by linear programming: A
1035 tool for geodynamic modeling and its application to subduction zone decarbonation. *Earth and*
1036 *Planetary Science Letters*, 236(1–2), 524–541. <https://doi.org/10.1016/J.EPSL.2005.04.033>
- 1037 Cook, K. L., & Royden, L. H. (2008). The role of crustal strength variations in shaping
1038 orogenic plateaus, with application to Tibet. *Journal of Geophysical Research: Solid Earth*,
1039 113(B8). <https://doi.org/10.1029/2007JB005457>
- 1040 Cox, S. F. (2010). The application of failure mode diagrams for exploring the roles of
1041 fluid pressure and stress states in controlling styles of fracture-controlled permeability
1042 enhancement in faults and shear zones. *Geofluids*, 10(1–2), 217–233.
1043 <https://doi.org/10.1111/j.1468-8123.2010.00281.x>
- 1044 Dal Piaz, G. V., Bistacchi, A., & Massironi, M. (2003). Geological outline of the Alps.
1045 *Episodes*, 26(3), 175–180. <https://doi.org/https://doi.org/10.18814/epiugs/2003/v26i3/004>
- 1046 Dall’Asta, N., Hoareau, G., Manatschal, G., Centrella, S., Denèle, Y., Ribes, C., & Kalifi,
1047 A. (2022). Structural and petrological characteristics of a Jurassic detachment fault from the
1048 Mont-Blanc massif (Col du Bonhomme area, France). *Journal of Structural Geology*,
1049 159(March). <https://doi.org/10.1016/j.jsg.2022.104593>
- 1050 Deng, X.-D., Li, J.-W., Luo, T., and Wang, H.-Q., 2017, Dating magmatic and
1051 hydrothermal processes using andradite-rich garnet U–Pb geochronometry. *Contributions to*
1052 *Mineralogy and Petrology*, v. 172, p. 71, doi:10.1007/s00410-017-1389-2.
- 1053 Egli, D., Müller, W., & Mancktelow, N. (2016). Laser-cut Rb–Sr microsampling dating
1054 of deformational events in the Mont Blanc-Aiguilles Rouges region (European Alps). *Terra*
1055 *nova*, 28(1), 35-42. <https://doi.org/10.1111/ter.12184>
- 1056 Egli, D., Mancktelow, N., & Spikings, R. (2017). Constraints from ⁴⁰Ar/³⁹Ar
1057 geochronology on the timing of Alpine shear zones in the Mont Blanc-Aiguilles Rouges region
1058 of the European Alps. *Tectonics*, 36(4), 730-748. <https://doi.org/10.1002/2016TC004450>
- 1059 Etheridge, M. A. (1983). Differential stress magnitudes during regional deformation and
1060 metamorphism: Upper bound imposed by tensile fracturing. *Geology*, 11(4), 231–234.
1061 [https://doi.org/10.1130/0091-7613\(1984\)12](https://doi.org/10.1130/0091-7613(1984)12)

- 1062 Fitzpayne, A., Giuliani, A., Hergt, J., Woodhead, J. D., & Maas, R. (2020). Isotopic
1063 analyses of clinopyroxenes demonstrate the effects of kimberlite melt metasomatism upon the
1064 lithospheric mantle. *Lithos*, 370, 105595. <https://doi.org/10.1016/j.lithos.2020.105595>
- 1065 Galli, A., Mancktelow, N., Reusser, E., & Caddick, M. (2007). Structural geology and
1066 petrography of the Naret region (northern Valle Maggia, N.Ticino, Switzerland). *Swiss Journal*
1067 *of Geosciences*, 100(1), 53–70. <https://doi.org/10.1007/s00015-007-1211-7>
- 1068 Gapais, D., Bale, P., Choukroune, P., Cobbold, P. R., Mahjoub, Y., & Marquer, D.
1069 (1987). Bulk kinematics from shear zone patterns: some field examples. *Journal of Structural*
1070 *Geology*, 9(5–6), 635–646. [https://doi.org/10.1016/0191-8141\(87\)90148-9](https://doi.org/10.1016/0191-8141(87)90148-9)
- 1071 Girault, J. B., Bellahsen, N., Boutoux, A., Rosenberg, C. L., Nanni, U., Verlaguet, A., &
1072 Beyssac, O. (2020). The 3-D Thermal Structure of the Helvetic Nappes of the European Alps:
1073 Implications for Collisional Processes. *Tectonics*, 39(3), e2018TC005334.
1074 <https://doi.org/10.1029/2018TC005334>
- 1075 Giuliani, A., Guillong, M., Maas, R., & Howarth, G. H. (2023). In-situ Rb-Sr dating of
1076 mica without employing the MicaMG standard. In Goldschmidt 2023 Conference.
1077 GOLDSCHMIDT. <https://doi.org/10.7185/gold2023.20131>
- 1078 Glotzbach, C., Reinecker, J., Danišík, M., Rahn, M., Frisch, W., & Spiegel, C. (2010).
1079 Thermal history of the central Gotthard and Aar massifs, European Alps: Evidence for steady
1080 state, long-term exhumation. *Journal of Geophysical Research: Earth Surface*, 115(F3).
1081 <https://doi.org/10.1029/2009JF001304>
- 1082 Goncalves, P., Oliot, E., Marquer, D., & Connolly, J. A. D. (2012). Role of chemical
1083 processes on shear zone formation: An example from the grimsel metagranodiorite (Aar massif,
1084 Central Alps). *Journal of Metamorphic Geology*, 30(7), 703–722. <https://doi.org/10.1111/j.1525-1314.2012.00991.x>
- 1086 Goncalves, P., Poilvet, J. C., Oliot, E., Trap, P., & Marquer, D. (2016). How does shear
1087 zone nucleate? An example from the Suretta nappe (Swiss Eastern Alps). *Journal of Structural*
1088 *Geology*, 86, 166–180. <https://doi.org/10.1016/j.jsg.2016.02.015>
- 1089 Green, E., Holland, T., & Powell, R. (2007). An order-disorder model for omphacitic
1090 pyroxenes in the system jadeite-diopside-hedenbergite-acmite, with applications to eclogitic
1091 rocks. *American Mineralogist*, 92(7), 1181–1189. <https://doi.org/10.2138/AM.2007.2401>
- 1092 Groome, W. G., Koons, P. O., & Johnson, S. E. (2008). Metamorphism, transient mid-
1093 crustal rheology, strain localization and the exhumation of high-grade metamorphic rocks.
1094 *Tectonics*, 27(1). <https://doi.org/10.1029/2006TC001992>
- 1095 Guermani, A., & Pennacchioni, G. (1998). Brittle precursors of plastic deformation in a
1096 granite: An example from the Mont Blanc massif (Helvetic, western Alps). *Journal of Structural*
1097 *Geology*, 20(2–3), 135–148. [https://doi.org/10.1016/S0191-8141\(97\)00080-1](https://doi.org/10.1016/S0191-8141(97)00080-1)
- 1098 Guillong, M., Hametner, K., Reusser, E., Wilson, S. A., & Günther, D. (2005).
1099 Preliminary characterisation of new glass reference materials (GSA-1G, GSC-1G, GSD-1G and
1100 GSE-1G) by laser ablation-inductively coupled plasma-mass spectrometry using 193 nm, 213 nm
1101 and 266 nm wavelengths. *Geostandards and Geoanalytical Research*, 29(3), 315–331.
1102 <https://doi.org/10.1111/j.1751-908X.2005.tb00903.x>

- 1103 Guillong, M., von Quadt, A., Sakata, S., Peytcheva, I., & Bachmann, O. (2014). LA-ICP-
1104 MS Pb–U dating of young zircons from the Kos–Nisyros volcanic centre, SE Aegean arc. *J.*
1105 *Anal. At. Spectrom.*, 29(6), 963–970. <https://doi.org/10.1039/C4JA00009A>
- 1106 Hafner, S. (1958). Petrographie des südwestlichen Gotthardmassives (zwischen St.
1107 Gotthardpass und Nufenenpass). *Schweizerische Mineralogische und Petrographische*
1108 *Mitteilungen* (Vol. 38). <https://doi.org/10.3929/ethz-a-000097546>
- 1109 Handy, M. R., M. Schmid, S., Bousquet, R., Kissling, E., & Bernoulli, D. (2010).
1110 Reconciling plate-tectonic reconstructions of Alpine Tethys with the geological-geophysical
1111 record of spreading and subduction in the Alps. *Earth-Science Reviews*, 102(3–4), 121–158.
1112 <https://doi.org/10.1016/j.earscirev.2010.06.002>
- 1113 Hentschel, F., Janots, E., Trepmann, C. A., Magnin, V., & Lanari, P. (2020). Corona
1114 formation around monazite and xenotime during greenschist-facies metamorphism and
1115 deformation. *European Journal of Mineralogy*, 32(5), 521-544. [https://doi.org/10.5194/ejm-32-](https://doi.org/10.5194/ejm-32-521-2020)
1116 [521-2020](https://doi.org/10.5194/ejm-32-521-2020)
- 1117 Herwegh, M., Berger, A., Baumberger, R., Wehrens, P., & Kissling, E. (2017). Large-
1118 Scale Crustal-Block-Extrusion During Late Alpine Collision. *Scientific Reports*, 7(1), 1–10.
1119 <https://doi.org/10.1038/s41598-017-00440-0>
- 1120 Herwegh, M., Berger, A., Glotzbach, C., Wangenheim, C., Mock, S., Wehrens, P., et al.
1121 (2020). Late stages of continent-continent collision: Timing, kinematic evolution, and
1122 exhumation of the Northern rim (Aar Massif) of the Alps. *Earth-Science Reviews*, 200, 102959.
1123 <https://doi.org/10.1016/J.EARSCIREV.2019.102959>
- 1124 Hogmalm K. J., Zack T., Karlsson A. K. O., Sjöqvist A. S. L. and Garbe-Schönberg D.
1125 (2017) In situ Rb–Sr and K–Ca dating by LA-ICP-MS/MS: an evaluation of N₂O and SF₆ as
1126 reaction gases. *Journal of Analytical Atomic Spectrometry* 32, 305-313.
1127 DOI:10.1039/C6JA00362A
- 1128 Holland, T. J. B., & Powell, R. (1998). An internally consistent thermodynamic data set
1129 for phases of petrological interest. *Journal of Metamorphic Geology*, 16(3), 309–343.
1130 <https://doi.org/10.1111/J.1525-1314.1998.00140.X>
- 1131 Holland, T. J. B., & Powell, R. (2011). An improved and extended internally consistent
1132 thermodynamic dataset for phases of petrological interest, involving a new equation of state for
1133 solids. *Journal of Metamorphic Geology*, 29(3), 333–383. [https://doi.org/10.1111/J.1525-](https://doi.org/10.1111/J.1525-1314.2010.00923.X)
1134 [1314.2010.00923.X](https://doi.org/10.1111/J.1525-1314.2010.00923.X)
- 1135 Horstwood, M.S.A., Košler, J., Gehrels, G., Jackson, S.E., McLean, N.M., Paton, C.,
1136 Pearson, N.J., Sircombe, K., Sylvester, P., Vermeesch, P., Bowring, J.F., Condon, D.J., Schoene,
1137 B., 2016. Community-Derived Standards for LA - ICP - MS U-(Th-)Pb Geochronology –
1138 Uncertainty Propagation, Age Interpretation and Data Reporting. *Geostand Geoanal Res* 40,
1139 311–332. <https://doi.org/10.1111/j.1751-908X.2016.00379.x>
- 1140 Jamtveit, B., Petley-Ragan, A., Incel, S., Dunkel, K. G., Aupart, C., Austrheim, H.,
1141 Corfu, F., Menegon, L. & Renard, F. (2019). The effects of earthquakes and fluids on the
1142 metamorphism of the lower continental crust. *Journal of Geophysical Research: Solid Earth*,
1143 124(8), 7725-7755. <https://doi.org/10.1029/2018JB016461>

- 1144 Janots, E., & Rubatto, D. (2014). U-Th-Pb dating of collision in the external Alpine
1145 domains (Urseren zone, Switzerland) using low temperature allanite and monazite. *Lithos*, 184–
1146 187, 155–166. <https://doi.org/10.1016/j.lithos.2013.10.036>
- 1147 Janots, E., Engi, M., Berger, A., Allaz, J., Schwarz, J. O., & Spandler, C. (2008).
1148 Prograde metamorphic sequence of REE minerals in pelitic rocks of the Central Alps:
1149 Implications for allanite-monzazite-xenotime phase relations from 250 to 610°C. *Journal of*
1150 *Metamorphic Geology*, 26(5), 509–526. <https://doi.org/10.1111/j.1525-1314.2008.00774.x>
- 1151 Janots, E., Engi, M., Rubatto, D., Berger, A., Gregory, C., & Rahn, M. (2009).
1152 Metamorphic rates in collisional orogeny from in situ allanite and monazite dating. *Geology*,
1153 37(1), 11–14. <https://doi.org/10.1130/G25192A.1>
- 1154 Jébrak, M. (1997). Hydrothermal breccias in vein-type ore deposits: A review of
1155 mechanisms, morphology and size distribution. *Ore Geology Reviews*, 12(3), 111–134.
1156 [https://doi.org/10.1016/S0169-1368\(97\)00009-7](https://doi.org/10.1016/S0169-1368(97)00009-7)
- 1157 Jenkin, G. R., Ellam, R. M., Rogers, G., & Stuart, F. M. (2001). An investigation of
1158 closure temperature of the biotite Rb-Sr system: The importance of cation exchange. *Geochimica*
1159 *et Cosmochimica Acta*, 65(7), 1141–1160. [https://doi.org/10.1016/S0016-7037\(00\)00560-3](https://doi.org/10.1016/S0016-7037(00)00560-3)
- 1160 Kralik, M., Clauer, N., Holnsteiner, R., Huemer, H., & Kappel, F. (1992). Recurrent fault
1161 activity in the Grimsel Test Site (GTS, Switzerland) : revealed by Rb-Sr, K-Ar and tritium
1162 isotope techniques. *Journal - Geological Society (London)*, 149(2), 293–301.
1163 <https://doi.org/10.1144/GSJGS.149.2.0293>
- 1164 Lacombe, O., & Mouthereau, F. (2002). Basement-involved shortening and deep
1165 detachment tectonics in forelands of orogens: Insights from recent collision belts (Taiwan,
1166 Western Alps, Pyrenees). *Tectonics*, 21(4), 12–1. <https://doi.org/10.1029/2001TC901018>
- 1167 Lemoine, M., Bas, T., Arnaud-Vanneau, A., Arnaud, H., Dumont, T., Gidon, M., et al.
1168 (1986). The continental margin of the Mesozoic Tethys in the Western Alps. *Marine and*
1169 *Petroleum Geology*, 3(3), 179–199. [https://doi.org/10.1016/0264-8172\(86\)90044-9](https://doi.org/10.1016/0264-8172(86)90044-9)
- 1170 Leydier, T., Goncalves, P., Lanari, P., & Oliot, E. (2019). On the petrology of brittle
1171 precursors of shear zones – An expression of concomitant brittle deformation and fluid–rock
1172 interactions in the ‘ductile’ continental crust? *Journal of Metamorphic Geology*, 37(8), 1129–
1173 1149. <https://doi.org/10.1111/jmg.12504>
- 1174 Lützenkirchen, V., & Loew, S. (2011). Late Alpine brittle faulting in the Rotondo granite
1175 (Switzerland): Deformation mechanisms and fault evolution. *Swiss Journal of Geosciences*,
1176 104(1), 31–54. <https://doi.org/10.1007/s00015-010-0050-0>
- 1177 Ma, X., Hertrich, M., Amann, F., Bröker, K., Doonechaly, N. G., Gischig, V., et al.
1178 (2022). Multi-disciplinary characterizations of the BedrettoLab-A new underground geoscience
1179 research facility. *Solid Earth*, 13(2), 301–322. <https://doi.org/10.5194/se-13-301-2022>
- 1180 Mancktelow, N., & Pennacchioni, G. (2010). Why calcite can be stronger than quartz.
1181 *Journal of Geophysical Research: Solid Earth*, 115(10), 1–16.
1182 <https://doi.org/10.1029/2009JB006526>
- 1183 Mancktelow, N., & Pennacchioni, G. (2020). Intermittent fracturing in the middle
1184 continental crust as evidence for transient switching of principal stress axes associated with the

- 1185 subduction zone earthquake cycle. *Geology*, 48(11), 1072–1076.
1186 <https://doi.org/10.1130/G47625.1>
- 1187 McDonough, W. F., & Sun, S. S. (1995). The composition of the Earth. *Chemical*
1188 *geology*, 120(3-4), 223-253. [https://doi.org/10.1016/0009-2541\(94\)00140-4](https://doi.org/10.1016/0009-2541(94)00140-4)
- 1189 Melosh, B. L., Rowe, C. D., Smit, L., Groenewald, C., Lambert, C. W., & Macey, P.
1190 (2014). Snap, Crackle, Pop: Dilational fault breccias record seismic slip below the brittle–plastic
1191 transition. *Earth and Planetary Science Letters*, 403, 432-445.
1192 <https://doi.org/10.1016/j.epsl.2014.07.002>
- 1193 Menegon, L., & Pennacchioni, G. (2010). Local shear zone pattern and bulk deformation
1194 in the Gran Paradiso metagranite (NW Italian Alps). *International Journal of Earth Sciences*,
1195 99(8), 1805–1825. <https://doi.org/10.1007/S00531-009-0485-6>
- 1196 Menegon, L., Nasipuri, P., Stünitz, H., Behrens, H., & Ravna, E. (2011). Dry and strong
1197 quartz during deformation of the lower crust in the presence of melt. *Journal of Geophysical*
1198 *Research: Solid Earth*, 116(B10). <https://doi.org/10.1029/2011JB008371>
- 1199 Mohn, G., Manatschal, G., Beltrando, M., & Hauptert, I. (2014). The role of rift-inherited
1200 hyper-extension in Alpine-type orogens. *Terra Nova*, 26(5), 347-353.
1201 <https://doi.org/10.1111/ter.12104>
- 1202 Mouthereau, F., Watts, A. B., & Burov, E. (2013). Structure of orogenic belts controlled
1203 by lithosphere age. *Nature geoscience*, 6(9), 785-789. <https://doi.org/10.1038/ngeo1902>
- 1204 Musso Piantelli, F., Mair, D., Berger, A., Schlunegger, F., Wiederkehr, M., Kurmann, E.,
1205 et al. (2022). 4D reconstruction of the Doldenhorn nappe-basement system in the Aar massif:
1206 Insights into late-stage continent-continent collision in the Swiss Alps. *Tectonophysics*, 843,
1207 229586. <https://doi.org/10.1016/J.TECTO.2022.229586>
- 1208 Newton, R. C., Charlu, T. V., & Kleppa, O. J. (1980). Thermochemistry of the high
1209 structural state plagioclases. *Geochimica et Cosmochimica Acta*. [https://doi.org/10.1016/0016-](https://doi.org/10.1016/0016-7037(80)90283-5)
1210 [7037\(80\)90283-5](https://doi.org/10.1016/0016-7037(80)90283-5)
- 1211 Nibourel, L., Berger, A., Egli, D., Heuberger, S., & Herwegh, M. (2021). Structural and
1212 thermal evolution of the eastern Aar Massif: insights from structural field work and Raman
1213 thermometry. *Swiss Journal of Geosciences*, 114(1). [https://doi.org/10.1186/s00015-020-00381-](https://doi.org/10.1186/s00015-020-00381-3)
1214 [3](https://doi.org/10.1186/s00015-020-00381-3)
- 1215 Oliot, E., Goncalves, P., & Marquer, D. (2010). Role of plagioclase and reaction
1216 softening in a metagranite shear zone at mid-crustal conditions (Gotthard Massif, Swiss Central
1217 Alps). *Journal of Metamorphic Geology*, 28(8), 849–871. [https://doi.org/10.1111/j.1525-](https://doi.org/10.1111/j.1525-1314.2010.00897.x)
1218 [1314.2010.00897.x](https://doi.org/10.1111/j.1525-1314.2010.00897.x)
- 1219 Oliot, E., Goncalves, P., Schulmann, K., Marquer, D., & Lexa, O. (2014). Mid-crustal
1220 shear zone formation in granitic rocks: Constraints from quantitative textural and
1221 crystallographic preferred orientations analyses. *Tectonophysics*, 612–613, 63–80.
1222 <https://doi.org/10.1016/j.tecto.2013.11.032>
- 1223 Paton, C., Hellstrom, J., Paul, B., Woodhead, J. and Hergt, J. (2011) Iolite: Freeware for
1224 the visualisation and processing of mass spectrometric data. *Journal of Analytical Atomic*
1225 *Spectrometry*. doi:10.1039/c1ja10172b.

- 1226 Pennacchioni, G., Di Toro, G., Brack, P., Menegon, L., & Villa, I. M. (2006). Brittle–
1227 ductile–brittle deformation during cooling of tonalite (Adamello, Southern Italian Alps).
1228 *Tectonophysics*, 427(1-4), 171-197. <https://doi.org/10.1016/j.tecto.2006.05.019>
- 1229 Pennacchioni, G., Ceccato, A., Fioretti, A. M., Mazzoli, C., Zorzi, F., & Ferretti, P.
1230 (2016). Episyenites in meta-granitoids of the Tauern Window (Eastern Alps): unpredictable?
1231 *Journal of Geodynamics*, 101, 73–87. <https://doi.org/10.1016/j.jog.2016.04.001>
- 1232 Pfiffner, O. A. (2016). Basement-involved thin-skinned and thick-skinned tectonics in the
1233 Alps. *Geological Magazine*, 153(5-6), 1085-1109. doi:10.1017/S0016756815001090
- 1234 Piccolo, A., Faccenda, M., Carosi, R., Montomoli, C., & Visonà, D. (2018). Crustal
1235 strength control on structures and metamorphism in collisional orogens. *Tectonophysics*, 746,
1236 470-492. <https://doi.org/10.1016/j.tecto.2017.09.018>
- 1237 Pleuger, J., Mancktelow, N., Zwingmann, H., & Manser, M. (2012). K–Ar dating of
1238 synkinematic clay gouges from Neoalpine faults of the Central, Western and Eastern Alps.
1239 *Tectonophysics*, 550–553, 1–16. <https://doi.org/10.1016/J.TECTO.2012.05.001>
- 1240 Pozzi, G., Scuderi, M. M., Tinti, E., Nazzari, M., & Collettini, C. (2022). The role of fault
1241 rock fabric in the dynamics of laboratory faults. *Journal of Geophysical Research: Solid Earth*,
1242 127(6), e2021JB023779. <https://doi.org/10.1029/2021JB023779>
- 1243 Redaa A., Farkaš J., Gilbert S., Collins A. S., Wade B., Löhr S., Zack T. & Garbe-
1244 Schönberg D. (2021) Assessment of elemental fractionation and matrix effects during in situ Rb–
1245 Sr dating of phlogopite by LA-ICP-MS/MS: implications for the accuracy and precision of
1246 mineral ages. *Journal of Analytical Atomic Spectrometry* 36, 322-344. DOI:
1247 <https://doi.org/10.1039/D0JA00299B>
- 1248 Redaa A., Farkaš J., Gilbert S., Collins A. S., Löhr S., Vasegh D., Forster M., Blades M.,
1249 Zack T., Giuliani A., Maas R., Baldermann A., Dietzel M. & Garbe-Schönberg D. (2023)
1250 Testing Nano-Powder and Fused-Glass Mineral Reference Materials for In Situ Rb-Sr Dating of
1251 Glauconite, Phlogopite, Biotite and Feldspar via LA-ICP-MS/MS. *Geostandards and*
1252 *Geoanalytical Research* 47, 23-48. <https://doi.org/10.1111/ggr.12467>
- 1253 Ribeiro, B. V., Kirkland, C. L., Kelsey, D. E., Reddy, S. M., Hartnady, M. I., Faleiros, F.
1254 M., ... & Clark, C. (2023). Time-strain evolution of shear zones from petrographically
1255 constrained Rb–Sr muscovite analysis. *Earth and Planetary Science Letters*, 602, 117969.
1256 <https://doi.org/10.1016/j.epsl.2022.117969>
- 1257 Rast, M., Galli, A., Ruh, J. B., Guillong, M., & Madonna, C. (2022). Geology along the
1258 Bedretto tunnel: kinematic and geochronological constraints on the evolution of the Gotthard
1259 Massif (Central Alps). *Swiss Journal of Geosciences*, 115(1). <https://doi.org/10.1186/s00015-022-00409-w>
- 1261 Ricchi, E., Bergemann, C., Gnos, E., Berger, A., Rubatto, D., & Whitehouse, M. J.
1262 (2019). Constraining deformation phases in the Aar Massif and the Gotthard Nappe
1263 (Switzerland) using Th-Pb crystallization ages of fissure monazite-(Ce). *Lithos*, 342–343, 223–
1264 238. <https://doi.org/10.1016/J.LITHOS.2019.04.014>
- 1265 Rolland, Y., & Rossi, M. (2016). Two-stage fluid flow and element transfers in shear
1266 zones during collision burial-exhumation cycle: Insights from the Mont Blanc Crystalline Massif
1267 (Western Alps). *Journal of Geodynamics*, 101, 88-108. <https://doi.org/10.1016/j.jog.2016.03.016>

- 1268 Rolland, Y., Rossi, M., Cox, S. F., Corsini, M., Mancktelow, N., Pennacchioni, G., et al.
1269 (2008). $^{40}\text{Ar}/^{39}\text{Ar}$ dating of synkinematic white mica: Insights from fluid-rock reaction in low-
1270 grade shear zones (Mont Blanc Massif) and constraints on timing of deformation in the NW
1271 external Alps. *Geological Society Special Publication*, 299, 293–315.
1272 <https://doi.org/10.1144/SP299.18>
- 1273 Rolland, Y., Cox, S. F., & Corsini, M. (2009). Constraining deformation stages in brittle-
1274 ductile shear zones from combined field mapping and $^{40}\text{Ar}/^{39}\text{Ar}$ dating: The structural
1275 evolution of the Grimsel Pass area (Aar Massif, Swiss Alps). *Journal of Structural Geology*,
1276 31(11), 1377–1394. <https://doi.org/10.1016/j.jsg.2009.08.003>
- 1277 Rosenberg, C. L., & Kissling, E. (2013). Three-dimensional insight into Central-Alpine
1278 collision: Lower-plate or upper-plate indentation? *Geology*, 41(12), 1219–1222.
1279 <https://doi.org/10.1130/G34584.1>
- 1280 Rosenberg, C. L., Bellahsen, N., Rabaute, A., & Girault, J. B. (2021). Distribution, style,
1281 amount of collisional shortening, and their link to Barrovian metamorphism in the European
1282 Alps. *Earth-Science Reviews*, 222, 103774. <https://doi.org/10.1016/j.earscirev.2021.103774>
- 1283 Rubatto, D., Hermann, J., Berger, A., & Engi, M. (2009). Protracted fluid-induced
1284 melting during Barrovian metamorphism in the Central Alps. *Contributions to Mineralogy and
1285 Petrology*, 158, 703–722. <https://doi.org/10.1007/s00410-009-0406-5>
- 1286 Sanchez, G., Rolland, Y., Schneider, J., Corsini, M., Oliot, E., Goncalves, P., Verati, C.,
1287 Lardeaux, J.M. & Marquer, D. (2011). Dating low-temperature deformation by $^{40}\text{Ar}/^{39}\text{Ar}$ on
1288 white mica, insights from the Argentera-Mercantour Massif (SW Alps). *Lithos*, 125(1–2), 521–
1289 536. <https://doi.org/10.1016/J.LITHOS.2011.03.009>
- 1290 Sarkar, S., Giuliani, A., Dalton, H., Phillips, D., Ghosh, S., Misev, S., & Maas, R. (2023).
1291 Derivation of Lamproites and Kimberlites from a Common Evolving Source in the Convective
1292 Mantle: the Case for Southern African ‘Transitional Kimberlites’. *Journal of Petrology*, 64(7),
1293 egad043. <https://doi.org/10.1093/petrology/egad043>
- 1294 Schmid, S. M., Fügenschuh, B., Kissling, E., & Schuster, R. (2004). Tectonic map and
1295 overall architecture of the Alpine orogen. *Eclogae Geologicae Helvetiae*, 97(1), 93–117.
1296 <https://doi.org/10.1007/S00015-004-1113-X>
- 1297 Seman, S., Stockli, D.F., and McLean, N.M., 2017, U-Pb geochronology of grossular-
1298 andradite garnet: *Chemical Geology*, v. 460, p. 106–116, doi:10.1016/j.chemgeo.2017.04.020.
- 1299 Sibson, R. H. (1985). Stopping of earthquake ruptures at dilational fault jogs. *Nature*,
1300 316(6025), 248–251. <https://doi.org/10.1038/316248a0>
- 1301 Sibson, R. H. (1987). Earthquake rupturing as a mineralizing agent in hydrothermal
1302 systems. *Geology*, 15(8), 701–704. [https://doi.org/10.1130/0091-
1303 7613\(1987\)15%3C701:ERAAMA%3E2.0.CO;2](https://doi.org/10.1130/0091-7613(1987)15%3C701:ERAAMA%3E2.0.CO;2)
- 1304 Sibson, R. H. (2003). Brittle-failure controls on maximum sustainable overpressure in
1305 different tectonic regimes. *American Association of Petroleum Geologists Bulletin*, 87(6), 901–
1306 908. <https://doi.org/10.1306/01290300181>

- 1307 Sibson, R. H., Robert, F., & Poulsen, K. H. (1988). High-angle reverse faults, fluid-
1308 pressure cycling, and mesothermal gold-quartz deposits. *Geology*, 16(June), 551–555.
1309 [https://doi.org/doi.org/10.1130/0091-7613\(1988\)016%3C0551:HARFFP%3E2.3.CO;2](https://doi.org/doi.org/10.1130/0091-7613(1988)016%3C0551:HARFFP%3E2.3.CO;2)
- 1310 Simonetti, M., Carosi, R., Montomoli, C., Cottle, J. M., & Law, R. D. (2020).
1311 Transpressive Deformation in the Southern European Variscan Belt: New Insights From the
1312 Aiguilles Rouges Massif (Western Alps). *Tectonics*, 39(6), e2020TC006153.
1313 <https://doi.org/10.1029/2020TC006153>
- 1314 Spear, F. S. (2010). Monazite–allanite phase relations in metapelites. *Chemical Geology*,
1315 279(1-2), 55-62. <https://doi.org/10.1016/j.chemgeo.2010.10.004>
- 1316 Steck, A. (1976). Albit-Oligoklas-Mineralgesellschaften der Peristeritlücke aus
1317 alpinmetamorphen Granitgneisen des Gotthardmassivs. *Schweizerische Mineralogische Und*
1318 *Petrographische Mitteilungen*, 56, 269–292. <https://doi.org/10.5169/seals-43687>
- 1319 Steck, A., & Burri, G. (1971). Chemismus und Paragenesen von Granaten aus
1320 Granitgneisen der Grünschiefer- und Amphiholitfazies der Zentralalpen. *Schweizerische*
1321 *Mineralogische Und Petrographische Mitteilungen*, 51(2–3), 534–538.
- 1322 Vanardois, J., Trap, P., Roger, F., Melleton, J., Marquer, D., Paquette, J. L., Goncalves,
1323 P., Cagnard, F., & Le Bayon, B. (2022). Deformation, crustal melting and magmatism in the
1324 crustal-scale East-Variscan Shear Zone (Aiguilles-Rouges and Mont-Blanc massifs, Western
1325 Alps). *Journal of Structural Geology*, 163, 104724. <https://doi.org/10.1016/J.JSG.2022.104724>
- 1326 Vermeesch, P. (2018). IsoplotR: A free and open toolbox for geochronology. *Geoscience*
1327 *Frontiers*, 9(5), 1479-1493. <https://doi.org/10.1016/j.gsf.2018.04.001>
- 1328 Vogt, K., Willingshofer, E., Matenco, L., Sokoutis, D., Gerya, T., & Cloetingh, S. (2018).
1329 The role of lateral strength contrasts in orogenesis: A 2D numerical study. *Tectonophysics*, 746,
1330 549–561. <https://doi.org/10.1016/J.TECTO.2017.08.010>
- 1331 Volpe, G., Pozzi, G., & Colletini, C. (2022). YBPR or SCC'? Suggestion for the
1332 nomenclature of experimental brittle fault fabric in phyllosilicate-granular mixtures. *Journal of*
1333 *Structural Geology*, 165, 104743. <https://doi.org/10.1016/j.jsg.2022.104743>
- 1334 Volpe, G., Pozzi, G., Colletini, C., Spagnuolo, E., Achtziger-Zupančič, P., Zappone, A.,
1335 Aldega, L., Meier, M.A., Giardini, D., & Cocco, M. (2023). Laboratory simulation of fault
1336 reactivation by fluid injection and implications for induced seismicity at the BedrettoLab, Swiss
1337 Alps. *Tectonophysics*, 862, 229987. <https://doi.org/10.1016/j.tecto.2023.229987>
- 1338 Waldbaum, D. R., & Thompson Jr., J. B. (1968). Mixing properties of sanidine
1339 crystalline solutions; [Part] 2, Calculations based on volume data. *American Mineralogist*.
- 1340 Wehrens, P., Berger, A., Peters, M., Spillmann, T., & Herwegh, M. (2016). Deformation
1341 at the frictional-viscous transition: Evidence for cycles of fluid-assisted embrittlement and
1342 ductile deformation in the granitoid crust. *Tectonophysics*, 693, 66–84.
1343 <https://doi.org/10.1016/j.tecto.2016.10.022>
- 1344 Weisenberger, T., & Bucher, K. (2010). Zeolites in fissures of granites and gneisses of
1345 the Central Alps. *Journal of Metamorphic Geology*, 28(8), 825–847.
1346 <https://doi.org/10.1111/J.1525-1314.2010.00895.X>

- 1347 White, R. W., Powell, R., Holland, T. J. B., Johnson, T. E., & Green, E. C. R. (2014).
1348 New mineral activity–composition relations for thermodynamic calculations in metapelitic
1349 systems. *Journal of Metamorphic Geology*, 32(3), 261–286. <https://doi.org/10.1111/JMG.12071>
- 1350 Whitney, D. L., & Evans, B. W. (2010). Abbreviations for names of rock-forming
1351 minerals. *American Mineralogist*, 95(1), 185–187. <https://doi.org/10.2138/am.2010.3371>
- 1352 Wiederkehr, M., Bousquet, R., Ziemann, M. A., Berger, A., & Schmid, S. M. (2011). 3-D
1353 assessment of peak-metamorphic conditions by Raman spectroscopy of carbonaceous material:
1354 An example from the margin of the Lepontine dome (Swiss Central Alps). *International Journal*
1355 *of Earth Sciences*, 100(5), 1029–1063. <https://doi.org/10.1007/S00531-010-0622-2>
- 1356 Willingshofer, E., Sokoutis, D., & Burg, J. P. (2005). Lithospheric-scale analogue
1357 modelling of collision zones with a pre-existing weak zone. *Geological Society, London, Special*
1358 *Publications*, 243(1), 277-294. <https://doi.org/10.1144/GSL.SP.2005.243.01.18>
- 1359 Wolf, S. G., Huisman, R. S., Braun, J., & Yuan, X. (2022). Topography of mountain
1360 belts controlled by rheology and surface processes. *Nature*, 606(7914), 516-521.
1361 <https://doi.org/10.1038/s41586-022-04700-6>
- 1362 Zertani, S., Menegon, L., Pennacchioni, G., Buisman, I., Corfu, F., & Jamtveit, B. (2023).
1363 Protracted localization of metamorphism and deformation in a heterogeneous lower-crustal shear
1364 zone. *Journal of Structural Geology*, 104960. <https://doi.org/10.1016/j.jsg.2023.104960>